CEBAF PROPOSAL COVER SHEET

This Proposal must be mailed to:

CEBAF
Scientific Director's Office
12000 Jefferson Avenue
Newport News, VA 23606

and received on or before 1 October 1991.

A. TITLE:

Measurement of the Flavor Singlet Charge Form Factor of the Proton, G_E^0

B. CONTACT PERSON:

Douglas H. Beck

ADDRESS, PHONE, AND ELECTRONIC MAIL ADDRESS:

Nuclear Physics Laboratory
University of Illinois at Urbana-Champaign
23 Stadium Drive
Champaign, IL 61820
217-244-7994 (work phone) 217-333-1215 (FAX)

C. IS THIS PROPOSAL BASED ON A PREVIOUSLY SUBMITTED PROPOSAL OR LETTER OF INTENT?

[ ] YES [X] NO

IF YES, TITLE OF PREVIOUSLY SUBMITTED PROPOSAL OR LETTER OF INTENT:

****

(CEBAF USE ONLY)

Receipt Date 1 OCT 91

Log Number Assigned PR 91-017

By [redacted]

A Proposal to CEBAF:

Measurement of the Flavor Singlet Charge Form Factor of the Proton, G_E^0

R. Alarcon, J. Comfort
Arizona State University

B. Beise, B. Filippone, R. McKeown
Caltech

G. Franklin, B. Quinn, R. Schumacher, V. Zeps
Carnegie Mellon University

W. Barry, R. Carlini, D. Mack, J. Napolitano,
C. Sinclair, W. Vulcan, S. Wood
CEBAF

D. Beck (Spokesman), M. Brussel, L. Cardman, R. Eisenstein,
R. Laszewski, A. Nathan, D. Nilsson
University of Illinois

M. Musolf
MIT

B. Holstein
University of Massachusetts

Abstract

In this experiment the flavor singlet proton form factor G_E^0 will be determined from an elastic parity-violation measurement in the range $0.1 \leq Q^2 \leq 0.3$ GeV^2. This form factor, which has never been measured, can be extracted in a model independent manner from this experiment. The flavor singlet charge form factor is sensitive to s quark components of the proton wave function and to possible isospin violation in the $p\,n$ system. The expected asymmetry is about -5×10^{-6}. With an expected precision of 5% ($\Delta A = 2.5 \times 10^{-7}$) for both statistical and systematic uncertainty, and using information from the complementary SAMPLE experiment at Bates, the proposed experiment can determine G_E^0 to about 3%. The experiment will be done by detecting the recoil protons in an azimuthally symmetric, iron-free toroidal spectrometer with a solid angle acceptance of 0.5 sr. The beam time request is 1500 h with 400 h for production data and 1100 h for preliminary tests.

Contents

List of Figures

List of Tables

1 Overview

The structure of the nucleon is not well understood from the fundamental point of view of QCD, i.e. in terms of the quark and gluon degrees of freedom that appear in the QCD Lagrangian. This proposal describes an experiment to measure a ground state proton matrix element which is sensitive to s quarks and hence to the $q\bar{q}$ ocean in the proton. The matrix element of interest is the elastic flavor singlet charge form factor, G_E^0 , which can be extracted from an electron-proton parity- violation measurement. If a relationship between proton and neutron structure is assumed (for example that the proton and neutron differ only by the interchange of u and d quarks), the s quark contribution to the charge form factor of the nucleon can be determined. This measurement complements the SAMPLE measurement at Bates by measuring the parity-violating asymmetry at the same momentum transfer, but at forward rather than backward angles. Both the charge and magnetic flavor singlet form factors have intrinsic interest as fundamental quantities, especially in view of the limited information about the nucleon wave function.

In this experiment, the parity-violating electron scattering asymmetry will be measured in the region $0.1 \leq Q^2 \leq 0.3$ GeV^2 ($Q^2 \cong 0.1$ in the SAMPLE experiment). The initial goal for the experiment is to measure an average form factor in this range of Q^2 ; ultimately it would be possible to determine the form factor at two or more values of Q^2 within this range. The asymmetry is about -5×10^{-6} at this momentum transfer; we are planning to measure the asymmetry with 5% statistical and systematic precision. Assuming a beam polarization of 49% the time required to reach this precision for the initial measurement would be about 400 hours. There is good reason to expect that by the time of the experiment higher beam polarizations will be available which would reduce this base time by up to a factor of two. We note that the systematic uncertainties quoted for the recent parity measurements at LAMPF, SIN, Mainz and Bates of a few $\times 10^{-8}$ suggest that systematic uncertainties of $\sim 10^{-7}$ should be attainable in this experiment.

To achieve the desired precision in a reasonable amount of time, this experiment must be run at high luminosity with a large-acceptance detector. In order to avoid measurements of electrons at very forward angles (with high luminosities) we propose to measure elastically scattered protons ($320 \leq p_{p'} \leq 570$ MeV with $75.8° \geq \theta_{p'} \geq 67.3°$, respectively); the electron beam energy will be 2.5 GeV. The spectrometer will consist of a toroidal array of eight normal conducting coils with a field integral of approximately 1.1 T·m. The spectrometer is designed to focus particles of the same momentum and scattering angle from the length of the extended target to a single point. The bend angle of 35° at the highest momentum is sufficient to allow complete shielding of the detectors. We expect to be able to count individual particles as opposed to integrate the signal in the detector; both options will yield acceptable results within the framework of this proposal. We are currently bench testing detectors and electronics similar to those planned for the experiment to ensure that counting is feasible. Particle counting provides the possibility of using time-of-flight to supplement the resolution of the spectrometer. In this case a pulsed beam (31.25 MHz) would be used. The discussion in the document assumes the latter option;

generally either integration or simple particle counting would result in simplified apparatus. The detector package for either mode would consist of approximately 80 scintillator elements; each element would cover approximately 10% of the momentum range in each of the eight segments.

The pattern for data taking will be chosen to reduce random background noise. The standard measurement interval will likely be 1/30 s (or a minimum in the local noise spectrum); i.e. the beam helicity will be reversed at a frequency of 30 Hz. The helicity pattern $+--+$ and its complement will be randomly chosen to reduce further background noise. With this scheme contributions from all frequencies at multiples of 30/2 Hz will be averaged to zero. In addition long term drifts will be effectively eliminated by averaging the two positive and the two negative helicity measurements in each sequence of four before forming the asymmetry.

The liquid hydrogen target will have a length of about 20 cm. It will be based on the design of the SAMPLE target and earlier SLAC targets. With a 40μA average current the total power deposited by the beam is about 200 W. The beam will be rastered over a target area of about 0.2 cm^2. Precise monitoring and control of the beam will be required for this experiment. For each measurement interval the beam characteristics - position, angle, energy, charge and possibly profile must be measured. Based on the present design of the experiment, for each measurement interval position measurements with precision on the order of 25 μm will be required. During the experiment continuous monitoring of false asymmetries due to changing beam characteristics will require substantial interaction with various accelerator controls, including, for example, some control of steering in the beam switchyard.

The collaboration brings much experience in both electron scattering and parity-violation experiments, in the instrumentation necessary for the experiment, and in knowledge of the CEBAF accelerator properties. Arizona State is undertaking the GEANT and TOSCA simulations. The Caltech group will be responsible for the target. The Carnegie Mellon collaborators will provide the data acquisition electronics and computers. CEBAF takes responsibility for accelerator and beamline instrumentation. The spectrometer will be designed and constructed by the University of Illinois group. Illinois will also provide the polarized electron source for the accelerator. We are discussing the construction of the detectors and polarimeter with another potential collaborator at this time; if they are unable to join our effort, Illinois will construct the detectors and CEBAF will construct the beam polarimeter. Theoretical support will be provided by MIT and UMass, with particular emphasis on the radiative corrections.

2 Physics

2.1 Introduction

The proposed experiment will measure the parity-violating asymmetry in elastic electron-proton scattering at momentum transfers between $0.1 \leq Q^2 \leq 0.3$ GeV^2. The elastic flavor singlet charge form factor, G_E^0, can be determined from this measurement (under the assumption that the Standard Model of electroweak interactions is valid) by combining the measured asymmetry with the known (ordinary) electromagnetic form factors of the proton, G_E^γ and G_M^γ, as well as the backward angle asymmetry to be measured in the Bates SAMPLE experiment. We note that the extraction of G_E^0 from the experiment is independent of the form factors of the neutron. This experiment, being most sensitive to G_E^0 is the complement to SAMPLE where the result will be dominated by G_M^0. In the absence of s quark contributions *and* using a model to relate proton and neutron structure, the flavor singlet charge form factor of the proton can be predicted from the electromagnetic charge form factors. A deviation from the 'expected' value will likely be interpreted in terms of a contribution from s quarks.

In principle, the asymmetry is sensitive to deviations from the Standard Model as well as to hadronic structure. However, the effect from possible new physics beyond the Standard Model is expected to be about an order of magnitude smaller than what might be expected from s quarks at these momentum transfers (although both estimates are obviously crude). If the 'expected' result for G_E^0 is obtained with a high degree of precision, it might then be possible to design a set of experiments optimized to determine all the hadronic structure physics necessary to look for departures from the Standard Model.

2.2 Flavor-dependent nucleon currents

The structure of the nucleon and, indeed, of all hadrons is poorly understood from the point of view of QCD. There is strong experimental evidence that the quarks and gluons of the QCD Lagrangian are manifest in deep-inelastic scattering and high energy e^+e^- annihilation among other processes. This is the regime in which the interactions of quarks are weak; it is "QED-like" in the sense that perturbation theory is a suitable tool. However, at low energies, QCD exhibits a property different from those encountered in QED, that of confinement. Here perturbation theory is not suitable and much effort has gone into discretization (lattice) and other techniques to try to understand QCD in this strong coupling regime. The purpose of this experiment is to make a low energy measurement of a quantity precisely defined in the context of QCD.

At low energies (corresponding to distance scales ~ 1 fm) little is known about the detailed structure of hadrons within the framework of QCD. As effective degrees of freedom, constituent quarks have proven to be very successful in categorizing and understanding the

spectra of baryons and mesons. Neither the general properties of constituent quarks nor their relationship to the quarks of QCD are well understood. For example, how large is a constituent quark? What are its charge and magnetic moment densities? Does it have any "excited" states? [We90] How does it respond to its environment (or, for example, are the constituent quarks in the nucleon and the pion the same)? One of the other successfully demonstrated consequences of QCD at low energies is the near chiral limit in which pions (at least) play the role of Goldstone bosons. [Do89] This "chiral perturbation theory" leads to the recovery of the old current algebra phenomenology of the strong interactions. The relationship of this language to that of constituent quarks is not clear, although some connection can be made through the "chiral quark" effective Lagrangian of Manohar and Georgi. [Ma84a] In this experiment an approach will be made from a different direction to try to gain some insight into the consequences of QCD at low energies. The $q\bar{q}$ ocean is subsumed in effective degrees of freedom in all of the pictures described above. Because this measurement is potentially sensitive to s quark contributions, it could provide direct information on the $\bar{q}q$ ocean at low energies.

The electroweak probe provides a precise means of studying the currents of quarks inside the nucleon. Because they are assumed to be Dirac particles in QCD, their currents are written simply as

$$\mathcal{J}_\mu^{ew} = \mathcal{Q}\bar{q}\gamma_\mu q$$

where $\mathcal{Q}$ is the charge appropriate to γ (ordinary electromagnetic charge) or Z^0 (neutral weak "charge", see below) coupling. The total electroweak current of the nucleon can then be written as a sum of the contributions from each of the quark flavors. [Ca78,Ka88,Mc89, Bc89,Na91] For example, the charge form factor can be divided up in this way

$$G_E^{p,\gamma} = \sum_j \mathcal{Q}_j G_E^{j,p}$$

where j runs over all quark flavors and $\mathcal{Q}_j$ is the electric charge. (We note that this is an exact statement.) In what follows the contributions of the quarks and antiquarks of a given flavor are combined. For example, $G_E^{u,p}$ will represent the net contribution of u and $\bar{u}$ quarks to the charge form factor. The expression for the charge form factor is then

$$G_E^{p,\gamma} = \frac{2}{3}G_E^{u,p} - \frac{1}{3}G_E^{d,p} + \ldots$$

The utility of measuring the corresponding weak neutral current of the nucleon (in this case via parity-violating electron scattering, see Section 2.3) is that it can also be within the terms of the $G_E^{j,p}$

$$G_E^{p,Z} = \sum_j \left(\frac{1}{2}T_j^3 - \mathcal{Q}_j \sin^2\theta_W\right) G_E^{j,p}$$

where $\left(1/2\, T_j^3 - \mathcal{Q}_j \sin^2\theta_W\right)$ is the weak charge. This in turn suggests that the contributions of the quark flavors may be separated experimentally.

There is some experimental evidence that suggests the s quark contribution to various proton matrix elements is significant (notably the Ellis-Jaffe sum rule measurement [As89] and the πN sigma term [Do89]). That s quarks are present in the nucleon is not an issue – deep inelastic measurements [Ab82] show that they carry about 3% of the nucleon's momentum. The plausibility of significant s quark contributions to low momentum transfer matrix elements is reinforced by the fact that these same deep inelastic measurements show that the momentum distribution $s(x)$ diverges as $x \to 0$.

The related quantity in this experiment is the s quark contribution to the proton charge form factor, $G_E^{s,p}$. In order to determine $G_E^{s,p}$, *three* measurements are required (in addition to the assumption that c and heavier quarks do not contribute significantly). In addition to the form factors $G_E^{p,\gamma}$ and $G_E^{p,Z}$ it is possible to make use of $G_E^{n,\gamma}$ *if* a model of the relation between proton and neutron structure is assumed. The simplest (and most commonly accepted) relationship is that interchanging u and d quarks will transform a neutron into a proton and vice versa, i.e., in this language

$$\begin{aligned} G_E^{u,p} &= G_E^{d,n} \\ G_E^{d,p} &= G_E^{u,n} \\ G_E^{s,p} &= G_E^{s,n} \end{aligned}$$

From the point of view of this experiment, it is most appropriate to discuss the various form factors in a model-independent framework. Since the electromagnetic and weak neutral currents of the nucleon are related, it is most natural to ask what new information is contained in $G_E^{p,Z}$. For this purpose it turns out to be useful to rewrite the individual flavor contributions in terms of an SU(3) flavor basis. The electromagnetic form factor is then

$$G_E^{p,\gamma} = G_E^{3,p} + \frac{1}{\sqrt{3}} G_E^{8,p}$$

where

$$G_E^{3,p} = \frac{1}{2}\left(G_E^{u,p} - G_E^{d,p}\right)$$

is the ordinary isovector form factor, and

$$G_E^{8,p} = \frac{1}{2\sqrt{3}}\left(G_E^{u,p} + G_E^{d,p} - 2G_E^{s,p}\right)$$

is the octet contribution. In this basis the weak neutral form factor is

$$\begin{aligned} G_E^{p,Z} &= \left(\frac{1}{2} - \sin^2\theta_\omega\right) G_E^{3,p} + \left(\frac{1}{2\sqrt{3}} - \frac{1}{\sqrt{3}}\sin^2\theta_W\right) G_E^{8,p} - \frac{1}{4} G_E^{0,p} \\ &= \left(\frac{1}{2} - \sin^2\theta_W\right) G_E^{p,\gamma} - \frac{1}{4} G_E^{0,p} \end{aligned}$$

where

$$G_E^{0,p} = \frac{1}{3}\left(G_E^{u,p} + G_E^{d,p} + G_E^{s,p}\right)$$

is the flavor singlet proton current. Therefore, the new information in the measurement is this flavor singlet current. It, along with the octet current, is sensitive to s-quark contributions.

There are two important features about the flavor singlet form factors that should be reiterated:

i. they are not "visible" to the electromagnetic probe; they appear only in the weak neutral current; and

ii. they can be extracted from proton asymmetry measurements using only proton form factors, i.e. no neutron form factors are required.

It is possible that s quarks could show up in either G_E (the present experiment) or in G_M (the SAMPLE experiment) if they are significant. In order to contribute to the charge form factor there must be a 'polarization' of the s and $\bar{s}$ distributions, i.e. they must have different spatial distributions. The presence of s and $\bar{s}$ with different angular momenta – opposite m_l, for example – would result in a contribution to G_M. A variety of combinations is therefore plausible in which s quarks would contribute more to one form factor than the other. It should be noted that at present no microscopic model is capable of realistically linking the contributions to the charge and magnetic form factors.

It should also be noted that in the absence of s quarks and assuming that protons and neutrons are related by the interchange of u and d quarks, definite predictions for the G^0 and hence for the proton asymmetry can be made using only measured proton and neutron form factors. Thus, with these assumptions, the asymmetry for this experiment can be calculated without using the results of the SAMPLE experiment (giving the Höhler result in Figure 2). A deviation from this value would indicate that one or both of the above assumptions was incorrect; one would not, however, know whether the effect was connected with the charge or current distributions.

This experiment will contribute to the understanding of the spatial distribution of s quarks in the nucleon. At this stage there are no reliable microscopic models of the nucleon which could predict any such distributions. However, understanding the structure of the nucleon at low energies in terms of the valence and ocean quarks of QCD (whether or not they can be economically described in terms of some effective degrees of freedom) is of fundamental importance. The flavor dependence of the distributions already provides interesting information which relates to this issue. In general terms it is easy to see that the flavor structure of the nucleon in coordinate space is not trivial. For simplicity consider nucleons with only u and d quarks (where again here q is used to represent the net contribution of q and $\bar{q}$ quarks). The mean square radius of the neutron is measured (very precisely) to be negative. Therefore, the d quarks in the neutron must have a larger mean square radius than the u quarks (assuming that valence quarks dominate contributions to the charge radius). To be more precise, since the mean square radius is proportional to the slope of G_E at Q^2=0, the 'quark interchange' nucleon model above ($p \rightarrow n$ and vice versa by interchanging u and d quarks) can be used to extract $\langle r_E^2 \rangle^{u,p}$ and $\langle r_E^2 \rangle^{d,p}$ (corresponding

to $G_E^{u,p}$ and $G_E^{d,p}$ or $G_E^{d,n}$ and $G_E^{u,n}$, respectively) [Be91]

$$\begin{aligned}\left\langle r_E^2\right\rangle^{u,p} &= \left\langle r_E^2\right\rangle^{d,n} = 0.640 \text{ fm}^2 \\ \left\langle r_E^2\right\rangle^{d,p} &= \left\langle r_E^2\right\rangle^{u,p} = 0.465 \text{ fm}^2\end{aligned}$$

This indeed shows the d quark radius to be larger in the neutron. The same analysis can be carried out for the magnetic form factor considering, for example, just the magnetic moment. In this case, the contributions of the u and d quarks (per unit charge) differ by slightly less than a factor of 1.8 (the symmetric non-relativistic SU(6) quark model gives a factor of 2)

$$\begin{aligned}\mu^{u,p} &= \mu^{d,n} = 1.84 \text{ n.m.} \\ \mu^{d,p} &= \mu^{u,n} = -1.03 \text{ n.m.}\end{aligned}$$

The differences between these results and the naive expectations are significant. In interpretation of these differences questions naturally arise about whether the quantities are dominated by the valence quarks (those carrying the nucleon's quantum numbers) or whether, at low energies, they are dominated by ocean quarks. It has been argued that the overall coupling to the constituent quark effective degrees of freedom is largely unaffected by the $\bar{q}q$ and gluon cloud [We90]; this is, however, an open question. The s quarks are relatively light and exclusively part of the ocean; therefore measurements sensitive to their contributions provide an unambiguous window on the dynamics of the ocean at low energies.

There is at least one phenomenological model in which the s quark contributions to G_E and G_M are considered. Jaffe [Ja89] has extended the dispersion theory based approach of Höhler *et al.* [Ho76] to include a strange vector meson, the $\phi(1020)$. As shown in Figure 1 there is a large relative change in G_E^0 in this model. There is also a significant effect on the parity-violation asymmetry as shown in Figure 2. As will be indicated later, a measurement of the asymmetry (which has a nominal value of -5×10^{-6}) with 5% statistical and 5% systematic uncertainties ($\Delta A = 2.5 \times 10^{-7}$) is the goal of this experiment.

2.3 Parity-violating elastic electron scattering

Electron scattering by current distributions is described by the coherent sum of γ and Z^0 amplitudes

$$\mathcal{M} = \mathcal{M}^\gamma + \mathcal{M}^Z$$

although we tend to ignore $\mathcal{M}^Z$ since it is very small, roughly 10^{-5} as large as $\mathcal{M}^\gamma$. However, $\mathcal{M}^Z$, unlike $\mathcal{M}^\gamma$, has both vector and axial-vector pieces. Therefore, the cross term in the cross section violates parity.

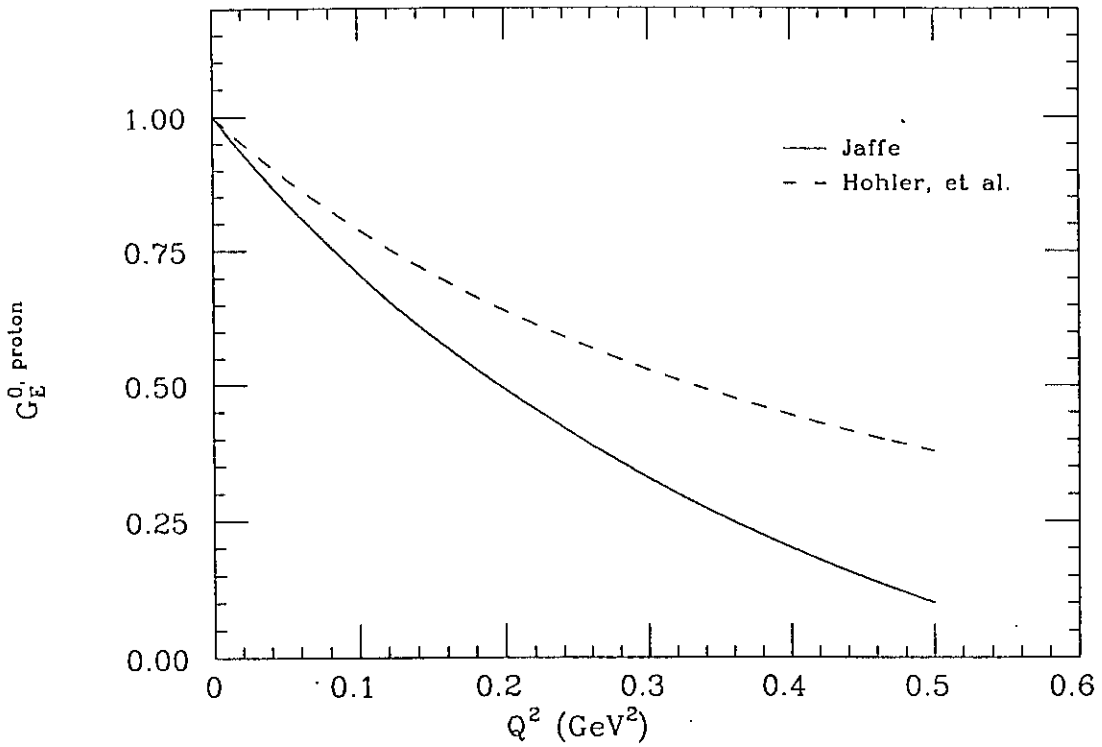

Figure 1: Comparison of G_E^0 as a function of momentum transfer for the form factor fits of Höhler *et al.* [Ho76] and Jaffe [Ja89]. The Höhler *et al.* fit assumes that there are no strange quarks in the nucleon.

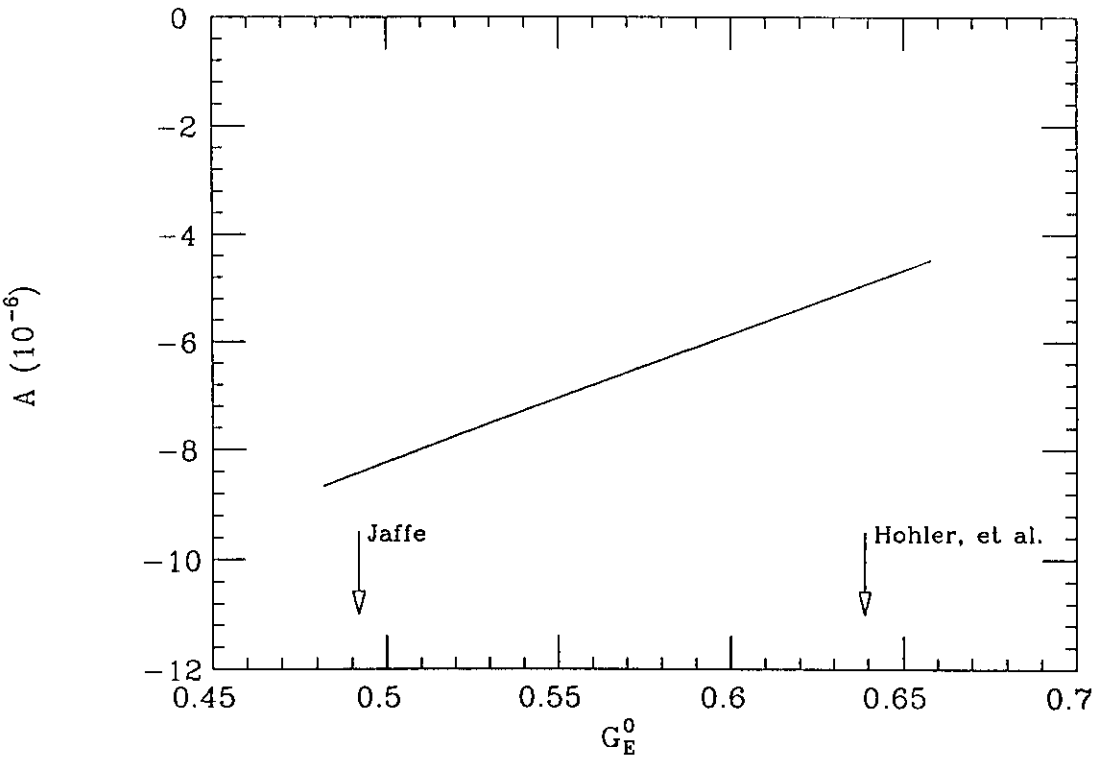

Figure 2: Elastic *ep* asymmetry at $Q^2 = 0.2$ for the range of G_E^0 values bracketed by the Höhler *et al.* and Jaffe form factors shown in Figure 1.

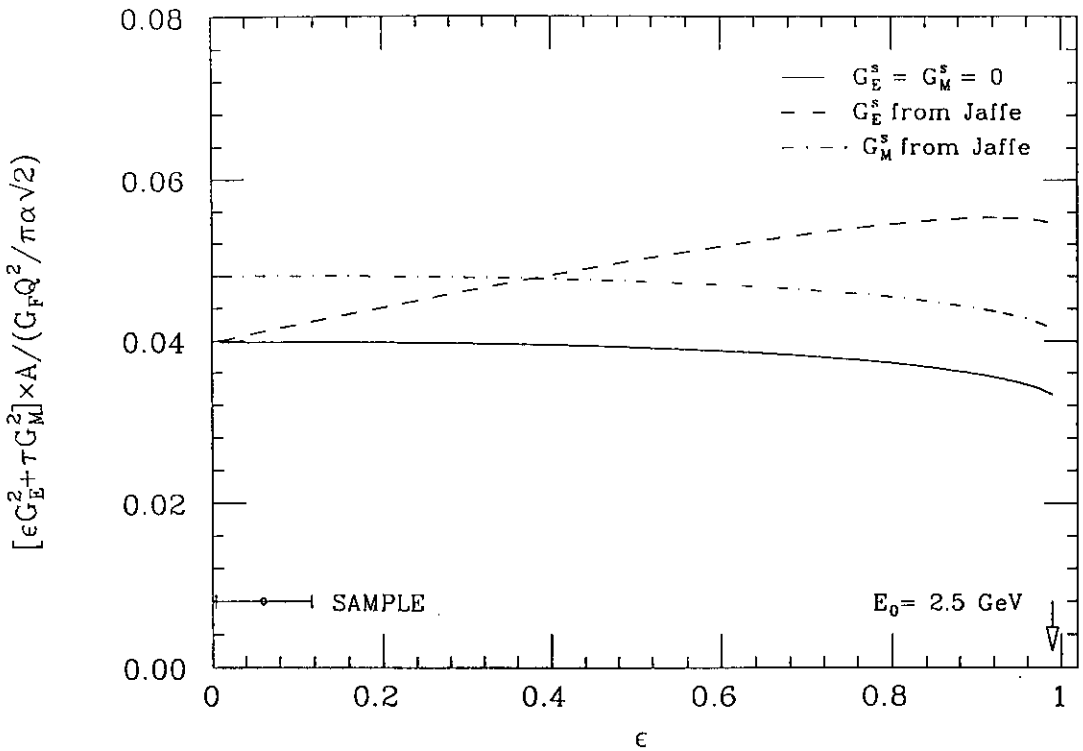

Figure 3: "Rosenbluth" plot of the parity violating asymmetry.

The cross term can be determined experimentally by comparing two parity- sensitive cross sections whose parity-conserving parts are identical. In this case the two cross sections are those of longitudinally polarized electrons with positive and negative helicities. Because the parity- violating terms in the cross sections are proportional to the electron helicity, the asymmetry is directly related to the cross term, i.e.

$$A = \frac{\sigma_+ - \sigma_-}{\sigma_+ + \sigma_-} \propto \mathcal{M}^\gamma \mathcal{M}^Z / |\mathcal{M}^\gamma|^2.$$

In terms of the form factors defined earlier, the asymmetry for elastic $\vec{e}p$ scattering is [Ca78, Mc89,Be89,Na91]

$$\begin{aligned} A &= -\frac{G_F Q^2}{\pi\alpha\sqrt{2}} \left[\varepsilon\, G_E^\gamma G_E^Z + \tau\, G_M^\gamma G_M^Z - \frac{1}{2}(1-4\sin^2\theta_W)(1-\varepsilon^2)^{1/2}\sqrt{\tau(1+\tau)}G_M^\gamma G_A^Z\right] \\ &\quad \times \left[\varepsilon\,(G_E^\gamma)^2 + \tau\,(G_M^\gamma)^2\right]^{-1} \end{aligned}$$

where $\tau \equiv Q^2/4M^2$ and $\varepsilon \equiv [1+2(1+\tau)\tan^2(\theta/2)]^{-1}$ can be varied between zero and unity for a fixed Q^2 by varying the beam energy and electron scattering angle. The "axial-vector" term proportional to G_A^Z arises from the axial-vector current in the proton which may couple directly to the Z^0. It is largely suppressed relative to the vector "electric" and "magnetic" terms because of the factor $(1-4\sin^2\theta_W) \approx 0.08$.

It is possible to control the relative contributions of G_E^0 and G_M^0 to the asymmetry, for a fixed Q^2, by varying ε. We demonstrate this in Figure 3 where we plot, for $Q^2 = 0.1$ GeV^2, the asymmetry as a function of ε. Note that we have "normalized" the asymmetry by dividing out the scale factor $-G_F Q^2/\pi\alpha\sqrt{2} = 3.6\times 10^{-5}$ at $Q^2 = 0.1$ GeV^2 and by

removing the "electromagnetic denominator" $\varepsilon\,(G_E^\gamma)^2 + \tau\,(G_M^\gamma)^2$. This is similar to the familiar "Rosenbluth" plot used to separate electric and magnetic form factors in the electromagnetic differential cross section. We plot the results with G_E^0 and G_M^0 given by assuming np isospin but no strangeness contribution, and by assuming each separately has a strangeness contribution given by the Jaffe model [Ja89]. One sees that small values of ε remove sensitivity to G_E^Z so that an experiment would primarily measure G_M^Z. This is the case with the SAMPLE experiment. At values of ε near unity, the asymmetry is relatively sensitive to G_E^0 (the G_E^0 term is approximately three times as large as the magnetic term at $Q^2 = 0.2$). Our experiment would run at a beam energy of 2.5 GeV or $\varepsilon = 0.99$.

2.4 Expected precision

The flavor singlet form factor G_E^0 will be extracted from the present measurement of the forward angle asymmetry by combining it with the result of the SAMPLE experiment. Assuming 7% uncertainties in the asymmetries for both experiments (the goals are 5% statistical and 5% systematic uncertainties in both cases) gives $\Delta G_E^0/G_E^0 \cong 3\%$. The only other inputs required to determine G_E^0 are the ordinary charge and magnetic form factors as well as the axial form factor. Only rudimentary knowledge of the axial form factor is required as it contributes only about 5% of the asymmetry for the CEBAF kinematics.

In order to determine an s quark form factor from G_E^0, it should be noted that at present (assuming that the proton and neutron are an isospin doublet) the approximately 100% uncertainty in G_E^n will dominate the uncertainty for any reasonable value of G_E^s. However, we expect that the G_E^n uncertainty will drop to perhaps the 20% level or lower in the near future and that the contributions to the G_E^s uncertainty would then be split very roughly between those from G_E^0 and G_E^n.

2.5 Radiative corrections

A proper interpretation of precision measurements of the hadronic neutral current requires that one take into consideration corrections to "tree- level" formulae introduced by higher-order electroweak processes. While the scale of these corrections is generically of $O(G_\mu\alpha/4\pi)$ at one-loop order, their importance relative to the tree-level amplitudes can be enhanced by the presence of large logarithms in one-loop amplitudes and by accidental numerical suppression of tree-level terms. [Mu90] In addition to carrying a dependence on the undetermined Higgs and t quark masses, electroweak corrections can also depend on theoretically uncertain hadronic physics. While (M_H, m_t) uncertainties introduce no fundamental limitation on the interpretation of precise electron scattering parity-violation experiments, hadronic uncertainties can represent a more serious issue in certain kinematic situations. One must be clear, then about where the latter uncertainties arise and to what extent they limit the information which might be extracted from precision measurements.

The ep elastic asymmetry presented in Section 2.3 depends on five proton form factors G_E^γ, G_E^Z, G_M^γ, G_M^Z and G_A^Z. Radiative corrections can be calculated for each form factor with varying degrees of accuracy. The uncertainty in G_E^0 due to uncertainties in radiative corrections turns out to be small. First, writing G_E^0 in terms of those form factors for which the corrections are typically calculated

$$G_E^0 = G_E^{\gamma,p} + G_E^{\gamma,n} + G_E^{s,p},$$

it is seen that the radiative correction for G_E^0 is dominated by that for $G_E^{\gamma,p}$ at low momentum transfers, i.e.

$$G_E^{0,meas} \cong G_E^{0,tree}(1 + R_V^p)$$

where R_V^p is the correction for the ordinary charge form factor. This factor is calculated to be -0.33 ± 0.01; [Mu90] the scale of the uncertainty is estimated from the work of Marciano and Sirlin. [Ma84b] The corresponding corrections for $G_E^{\gamma,n}$ and $G_E^{s,p}$ are calculated to be 0.015 and -0.015, respectively, with small uncertainties.

In addition to the direct radiative correction for G_E^0, the other potential source of difficulty is the relatively much less certain radiative correction for G_A^Z. The correction is estimated to be $R_A^p = -0.24 \pm 0.22$. [Mu90] However, as the axial term contributes only about 5% in the present kinematics, even this level of uncertainty is small compared with the overall uncertainty desired for G_E^0.

The ordinary radiative effects which enter into normal electron scattering experiments do not enter the asymmetry to first order. They do, however, affect the rates in that each cross section will be reduced by, in our case, about 15%. Therefore, the nominal running time for the experiment has been increased by this factor.

3 Experiment

3.1 Introduction

In this experiment the parity-violating asymmetry in elastic electron- proton scattering will be measured in the Q^2 range of 0.1 to 0.3 GeV^2. Because the asymmetries in these experiments are small, a large counting rate is required. In the present case the measured asymmetry will be a few $\times 10^{-6}$ and in order to achieve a statistical precision of 5% of this asymmetry approximately 10^{13} counts will be needed. The large counting rate is generally obtained by using a combination of high luminosities and detectors with large acceptances. In the present experiment a 20 cm long LH_2 target will be used with a 40 μA beam current ($\mathcal{L} = 2.1 \times 10^{38}$ cm^{-2} s^{-1}) and a detector with a solid angle acceptance of 0.50 sr.

For this ep elastic scattering experiment, it is useful to take advantage of recoil proton detection. As these protons have relatively low momentum in the region of interest ($<$ 600 MeV), a relatively simple spectrometer of very large acceptance can be designed.

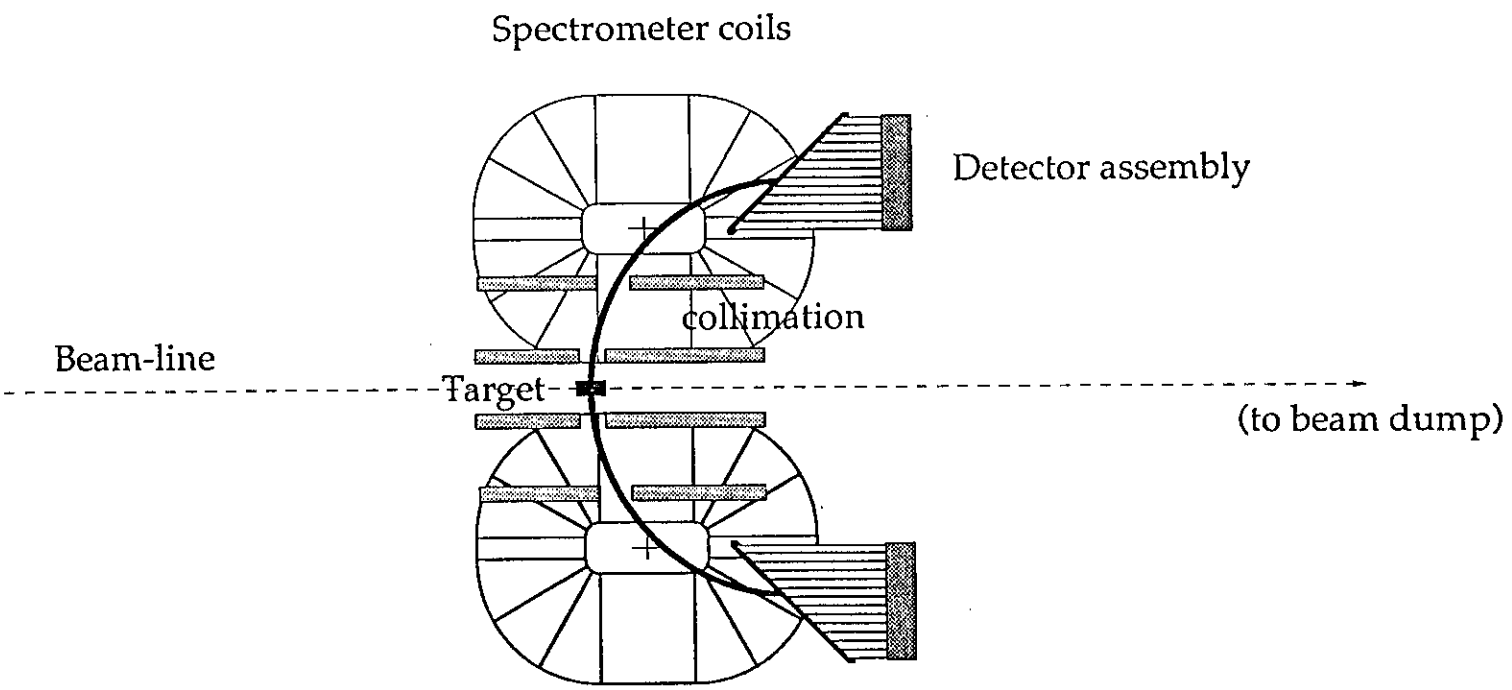

Figure 4: Schematic layout of the experiment.

Proton detection has the additional advantage that the detectors are at relatively large angles (with electrons at small scattering angles corresponding to a large Mott cross section) and away from the shower of particles from the (thick) target. These non-relativistic protons also have a large signal in simple detectors such as plastic scintillators. The spectrometer described in Section 4.1 has no magnetized iron, therefore, false asymmetries due to secondary scattering should not be a problem. Finally, this spectrometer is small enough to be positioned upstream of the pivot in Hall C so that it will neither be disturbed by nor interfere with other experiments.

The basic layout of the experiment is shown in Figure 4. Polarized electrons scatter from the 20 cm LH_2 target cell; recoiling protons in the angular range 67.3 - 76.8° are focussed according to their momentum by the spectrometer (the scattered electrons are not detected). This figure may be viewed as 1/8 of the experiment – it shows the particle trajectories for one of the eight segments of the azimuthally symmetric (with respect to the beam axis) spectrometer. The protons are detected by an array of plastic scintillators which are nominally 1 cm thick. The detectors will be shielded from the target by an internal baffle(s), and from general hall background with concrete shielding blocks.

In addition to the need for large rate, the experiment must be designed to reduce systematic errors to an acceptable level – the goal also being 5% of the measured asymmetry.

Table 1: Range of kinematics for elastic electron-proton scattering. The incident beam energy is 2.5 GeV.

Q^2 (GeV^2)	θ'_p ((deg))	p' (MeV)	T'_p (MeV)
0.1 - 0.3	76.8 - 67.3	321 - 571	53 - 160

Table 2: Experimental apparatus parameters.

Average current	40 μA
Target length	20 cm
Target thickness	1.4 g/cm^2
Luminosity	2.1×10^{38} cm^{-2}s^{-1}
Spectrometer acceptance	0.50 sr ([$\sin\theta\Delta\theta = 0.16$, $\Delta\phi = 0.39$] $\times$ 8)

This requires precise monitoring of beam characteristics such as position, angle, shape, energy and intensity as well as spectrometer acceptance, counting rates and backgrounds. A dedicated experimental setup clearly provides the most efficient and reliable means of making such a measurement. A symmetric detector with uniform azimuthal coverage is also the simplest to control in terms of systematic errors. In addition, this detector is designed to measure backgrounds continuously during the experiment.

3.2 Kinematics and rates

The kinematics for the experiment are presented in Table 1. Using an incident beam energy of 2.5 GeV, elastically scattered protons will be measured between the angles of 67.3 and 76.8° corresponding to the momentum transfers of 0.3 and 0.1 GeV^2, respectively. The spectrometer will accept particles in this range of scattering angle and in eight azimuthal segments covering half the full range, yielding a solid angle acceptance of 0.495 sr. A 20 cm long LH_2 target will be used, and the proposed beam current is limited to the 40 μA to be used in the SAMPLE experiment assuming that with beam rastering, this power deposition density can be handled. The luminosity is then $\mathcal{L} = 2.1 \times 10^{38}$ cm^{-2} s^{-1}. A summary of the experiment parameters is presented in Table 2.

With this combination of apparatus and an average elastic (Born) cross section of 0.7 μb/sr, the counting rate will be about 44 MHz in the whole spectrometer. With

Table 3: Summary of rates.

Average cross section	0.67 μb/sr
Total rate in detector	4.4×10^7 s^{-1}
Average physics asymmetry	-5.0×10^{-6}
Electron beam polarization	49%
δA statistical (5%)	1.3×10^{-7}
Counting time	400 h

segmentation into 80 detectors (eight segments $\times$ ten detectors per segment) the count rate in each detector will be limited to about 1 MHz. If the beam is bunched to provide pulses at 32 ns intervals the maximum counting rate per pulse in each detector segment is about 0.03. Assuming a beam polarization of 49%, the goal of 5% statistical precision can be met with a measurement time of 400 hr. A summary of the rates is presented in Table 3.

3.3 Physics backgrounds

The spectrometer described in Section 4 will accept protons over a broad correlated range of momenta and scattering angles; positions on the focal plane are, however, independent of the z (target) position of the scattering event. The raw inelastic proton background is less than 5% of the total elastic rate in any detector element. This yield can be reduced by using a time-of-flight cut; for example for a bin of 2 ns width centered on the elastic protons, the inelastic contribution can be reduced by a factor of about four. Time-of-flight will also allow us to directly measure the asymmetry of the background. In any case the physics background contributions to the asymmetry are expected to be small. We therefore expect to be able to determine the contribution of the background to the overall asymmetry with an accuracy of, at worst, a few percent.

Results of a Monte Carlo simulation of the elastic and background events at the focal plane of the spectrometer are shown in Figure 5. The present simulation includes realistic event generation, multiple scattering from the target and the approximate first order optical characteristics of the spectrometer. The inelastic proton spectra are taken from the code of Lightbody and O'Connell [Li88]. This code considers only protons from the decay of the Δ. However, for these near elastic kinematics, we find that higher lying resonances are excited by events with Q^2 near the elastic momentum transfer but with ϵ significantly smaller than one thus reducing their contribution. We estimate an increase of about 50% in the *inelastic* proton yield over the result using Lightbody and O'Connell shown in Figure 5. We note the general feature of the spectrometer that the inelastic protons with low momenta are focussed off the detector array. Pions with momenta in the acceptance of the spectrometer (between 320 and 570 MeV) are nearly $\beta = 1$ and therefore will arrive at the detectors

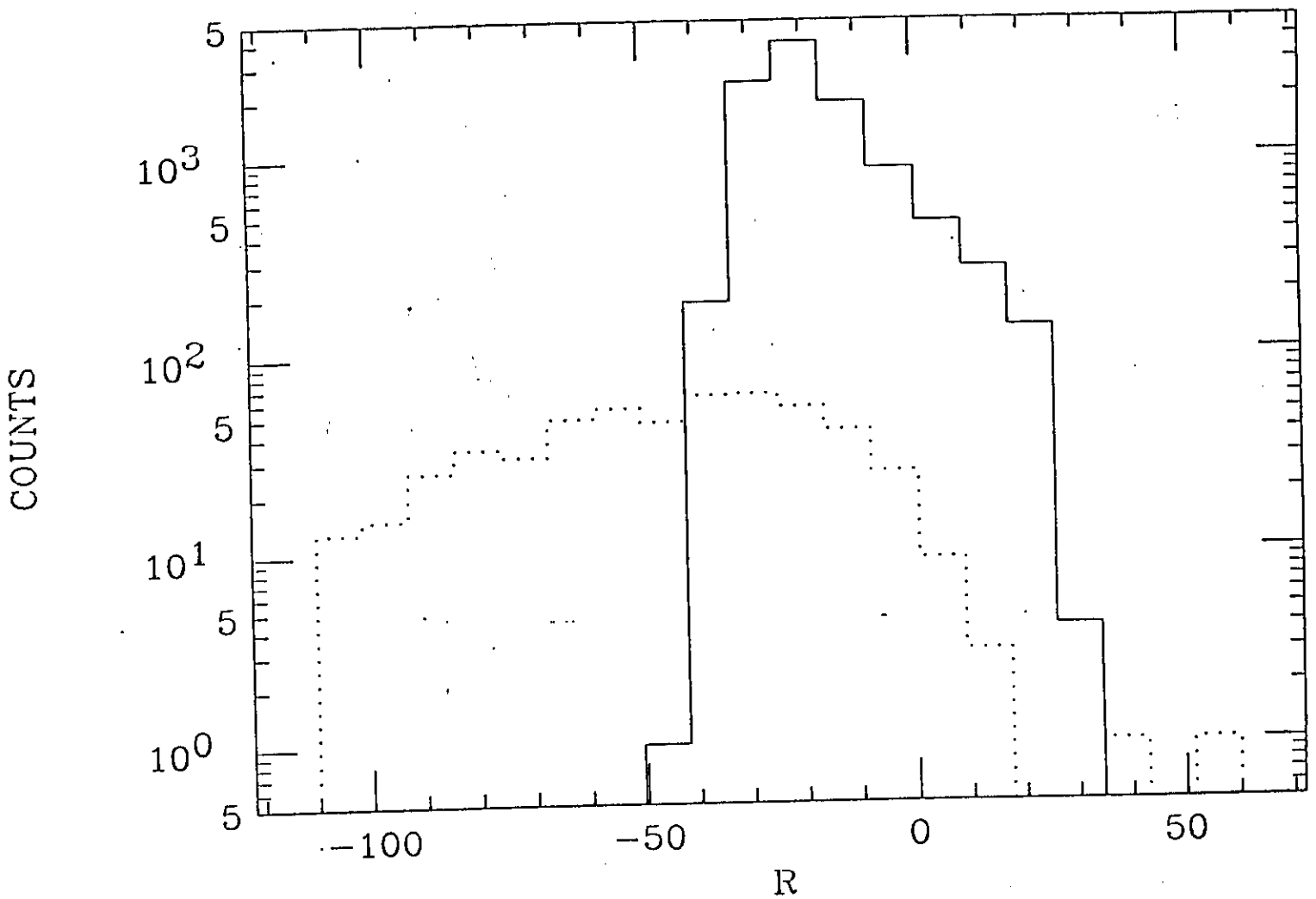

Figure 5: Monte Carlo simulation of spectrometer. Plot of counts vs. focal plane position R (defined in Section 4.1) for elastic protons (solid) and inelastic protons (dots).

about 7 ns after the beam pulse. They can therefore be eliminated from the yield in a straightforward manner by gating either the (counting or integrating) electronics off until after the $\beta = 1$ particles have passed the detectors (even a 10 ns long gate will suffice). The pion background is relatively flat in this momentum and angle range (again based on the Lightbody and O'Connell code). The cross sections are comparable to those of the inelastic protons.

There may also be some residual background associated with prompt particles from the target which are not stopped by the internal baffles and detector shielding. This background can also be eliminated with a broad gate as it would arrive at the detectors some 10 - 15 ns earlier than the elastic protons.

3.4 Uncertainties and corrections

3.4.1 Introduction

Because parity-violating asymmetries are small, analysis of the data in this experiment is more involved than in other electron scattering measurements. However, the framework is relatively straightforward. The starting point for assessing the uncertainties in the asymmetry is the normalized yield, i.e. the number of counts in the detector per unit beam charge. The asymmetry is determined from yields for the two beam helicities (each measured for a time T_h):

$$A^{meas} = \frac{Y_+ - Y_-}{Y_+ + Y_-}$$

where

$$\begin{aligned} Y_h &= \frac{(d\sigma/d\Omega)\mathcal{L}\Delta\Omega T_h}{Q_h} \\ &= \frac{C_h}{Q_h} \end{aligned}$$

and $d\sigma/d\Omega$ is the differential ep cross section, $\mathcal{L}$ is the luminosity, $\Delta\Omega$ is the solid angle acceptance, and C_h and Q_h are the total number of counts in the spectrometer and the beam charge passing through the target in time T_h, respectively. In each signal used to determine these quantities there may be, in addition to the true signal, contributions from random (not correlated with beam helicity) background noise, helicity correlated background noise and helicity correlated changes in beam, target and/or detector properties. The helicity correlated piece is separated into the set which can, in principle, be corrected, and the remainder ("correlated noise"). These contributions comprise the uncertainties and corrections for the experiment and are examined in turn below. Assessment of these contributions leads to tolerances on various parameter measurements (for example, beam position) as well as to a methodology for data taking.

The experiment will involve both the counting of individual scattered protons as well as the integration of various signals from beam monitors. Those systematic effects which

can be corrected enter the two types of measurements in similar ways; the effects of noise enter in different ways. These considerations are detailed below.

The remainder of this section is organized as follows. First, the uncertainties associated with beam charge and polarization are addressed, as they enter directly. The general effects of uncorrelated and correlated noise as well as those of helicity-correlated changes in beam parameters are treated next. Last, the effect of non-linearities is discussed. These considerations lead in general to specification of monitor tolerances and to strategies for data taking.

3.4.2 Beam charge measurement

The uncertainty in the measurement of the charge should contribute only a small amount to the overall uncertainty in the asymmetry, i.e. it should be significantly smaller than the uncertainty in the spectrometer signal. This uncertainty will be dominated by uncorrelated background noise (i.e. not particle counting statistics) to be discussed in general in Section 3.4.4. For all uncorrelated noise contributions to the overall uncertainty, the goal in this proposal is taken to be 5% of the uncertainty due to counting statistics. Therefore, if the measurement time is taken to be $T_h = 1/30$ s (as it will be throughout for illustration, see Section 3.4.3) the relative uncertainty required in the charge measurement is 5% of the relative uncertainty in the number of counts in time T_h, i.e.

$$\begin{aligned} \frac{\Delta Q}{Q} &= 0.05 \frac{1}{\sqrt{44\,\mathrm{MHz}\,T_h}} \\ &= 4 \times 10^{-5}. \end{aligned}$$

Note that consideration of the helicity correlated beam intensity changes yields the same tolerance as will be discussed below.

3.4.3 Beam polarization measurement

The measured asymmetry defined above is related to the physics asymmetry by

$$A^{meas} = P_e\, A^{phys}.$$

Therefore the uncertainty in the average beam polarization adds to the other systematic uncertainties in the experiment. Differences in the polarization for the two helicity states will not be important (see Section 3.4.6). We expect to be able to measure the average polarization to 2% (see Section 4.4.2).

3.4.4 Uncorrelated background noise

In this section the general effects of noise not correlated with beam helicity are considered and a measurement strategy is developed to reduce them to as low a level as possible. The

effects in the counting and integration modes are similar; the result in either case is that if the background is small relative to the signal in each measurement (of duration T_h), it will remain so in the final result if some simple precautions are taken. In the following the measured signal is denoted by S, the true (real) signal by R and the uncorrelated background by B.

In a measurement of duration T_h (with a single beam helicity), the overall uncertainty will be

$$\Delta^2 S \ = \Delta^2 R + \Delta^2 B$$

where $\Delta^2 R = C_h$ in the case of the signal from the spectrometer. If the true signal is to be measured very precisely using N such measurement intervals, then as long as two conditions are fulfilled the resulting uncertainty will be dominated by that of R. First, $\Delta^2 B$ must be smaller than $\Delta^2 R$, and, second, the N time intervals must be chosen in a random fashion relative to the background noise (in a sense that will become clear below) to prevent unintended helicity correlations. If these conditions are met, even if there is a significant background signal at, for example, a frequency of 60 Hz, $\Delta^2 S/S^2$ can in principle be made arbitrarily small (reduced by the factor N for many measurements).

In practice, to reduce the uncorrelated background as much as possible the following strategy will be used. First, measurements will be made for the period T_h corresponding to a frequency $f_h = 1/T_h$ (the beam helicity will be changed with a period of $T_h + \delta t$ where the time δt is used to read out the electronics after each measurement). This frequency will likely be 30 Hz depending on the local power spectrum of uncorrelated noise. For this discussion it is assumed that $f_h = 30$ Hz. Second, suppose that the pattern of four beam helicities $+ - - +$ is used for consecutive measurement intervals and suppose this pattern or its complement is chosen randomly to make up the N measurements. The uncorrelated noise components with frequencies $f >> f_h$ will largely average to zero leaving some small residual which will be reduced by N as in the preceding paragraph. Background components with frequencies at harmonics of 30 Hz will be averaged to zero with high precision in each measurement interval t_h. For background components with frequencies $f << f_h$ (for example, long term drifts), averaging measurements from intervals one and four, and two and three (i.e. the averaged measurements for each helicity are effectively made at the same time) before forming the asymmetry will result in cancellation of the effect of these low frequency components to the extent that they are changing linearly over the time period $4T_h$. This pattern has the added benefit of cancelling precisely background components at frequencies of $(2n+1)f_h/2$, $n = 0, 1, 2, \ldots$. For frequencies closer to f_h (where little power is expected), the contributions will simply be reduced by making N measurements as above. Note that if the $+ - - +$ and $- + + -$ patterns were not chosen randomly, noise at a frequency of $f_h/4$ would accumulate, generating an unintended helicity correlation.

The effect of uncorrelated noise in an integrated signal is straightforward – it simply adds to the true signal. In the counting mode, noise may enter, for example, the double pulse resolution time (i.e. this resolution may fluctuate). The true number of counts in a

measurement interval C_h is

$$\begin{aligned} C_h &= M_h + lM_h \\ &= M_h(1 + r\tau_d) \end{aligned}$$

where M_h is the measured number of counts and the loss fraction l is product of the rate r and the double pulse resolution time τ_d. The uncertainty in C_h is then

$$\Delta^2 C_h = \Delta^2 M_h (1 + r\tau_d)^2 + M_h^2 r^2 \tau_d^2 \frac{\Delta^2 \tau_d}{\tau_d^2}$$

i.e., it has a piece from ordinary counting statistics and a piece due to uncorrelated noise in the double pulse resolution time τ_d (the rate, unlike the double pulse resolution, is normally measured in the course of the experiment). For this experiment if the noise due to double pulse resolution fluctuations is to be less than 5% of the overall uncertainty, with loss fractions of 1%, the relative fluctuations (over the period $4T_h$) in the double pulse resolution (averaged over all detector elements) must be less than 4×10^{-3}. (The noise in question here is the residual noise, i.e. that noise not eliminated by the data- taking methodology described above.)

There will be a similar noise contribution in time-of-flight measurements. For example, consider the effect of a short gate of duration $T_g \cong 2$ ns set for each detector during the time the elastic protons arrive (see Section 4.2). If the machine is pulsed every 32 ns, in the standard measurement time of 1/30 s there will be $N_g = 1.04 \times 10^6$ such gates. The uncertainty in the measured number of counts including that from the fluctuating gate width will therefore be

$$\begin{aligned} \frac{\Delta^2 C_h}{C_h^2} &= \frac{\Delta^2 M_h}{M_h^2} + \frac{\Delta^2 T_l}{T_l^2} \\ &= \frac{\Delta^2 M_h}{M_h^2} + \frac{1}{N_g} \frac{\Delta^2 T_g}{T_g^2} \end{aligned}$$

where T_l ($\propto T_g$) is the live time. Therefore $\Delta T_g / T_g$ must be smaller than 4% to meet the "5%" standard.

3.4.5 Correlated background noise

There are many parameters throughout the entire experimental apparatus (including the accelerator) whose variations will be correlated with helicity at some level. The effects of those apparatus parameters which can be measured independently will be treated in the next Section; variations in all other parameters will be seen only indirectly in the spectrometer (or charge monitor) signal. These effects are referred to here as helicity-correlated background noise. They can be distinguished by providing for different means of reversing the beam helicity. For this experiment at least two different methods will be used. The "fast" helicity reversal will be effected by changing the sign on the drive signal of

a Pockels cell "± quarter-wave plate" in the laser drive to the source. In addition there is provision in the laser drive for the polarized source to insert a 1/2-wave plate in the optical path which will reverse the sign of the helicity at the target without any other changes (in particular, without changes in electrical signals) in the system. In practice this plate would be inserted for half the running time (changing from 'plate in' to 'plate out' several times during the experiment). The offset in the asymmetries so measured (which should only differ by a sign) is the overall effect of correlated noise on the asymmetry. Finally, the spin direction of the electrons in the beam can be changed to an arbitrary orientation using the electrostatic spin manipulator in the polarized source. Therefore, the polarization of the electrons upstream of the manipulator can be reversed in the normal way and the manipulator tuned to provide, for example, transverse polarization at the target in which case the parity-violating asymmetry vanishes.

3.4.6 Corrections for correlated parameter variations

In the expression above for the normalized yield all terms are effected by one or more of the beam, target and spectrometer properties except for the measurement interval. Many of these properties can be measured independent of the main signals to determine their dependence on beam helicity. Specifically, the beam energy, position, angle, shape, polarization and intensity will be measured in addition to the relative acceptances of the detector elements. The response of the yield to variations in these parameters (the *measured* derivatives rather than the various derivatives *calculated* below will be used for the analysis) as well as their helicity dependence will be measured continuously throughout the experiment. The tolerances for these measurements are again determined here by requiring that the false asymmetry corresponding to the tolerance is less than 5% of the overall systematic uncertainty in the asymmetry. If the time interval considered for measuring these parameters is again taken to be $T_h = 1/30$ s, the corresponding uncertainty in the asymmetry is about 8×10^{-4}; therefore, in 1/30 s the false asymmetry resulting from the resolution of the parameter measurements should be less than 4×10^{-5}.

In practice, each measured asymmetry A_m is composed of a number of such false asymmetries $A_{f,i}$ in addition to the true asymmetry A_t and the contribution from the correlated noise A_{cn} discussed in the previous section

$$\begin{aligned} A_m &= A_t + A_{cn} + \sum_i A_{f,i} \\ &\cong A_t + A_{cn} + \sum_i \frac{1}{Y}\frac{\partial Y}{\partial \alpha_i}\delta\alpha_i \end{aligned}$$

since for $Y_+ = Y_-$

Table 4: Tolerances on beam and spectrometer parameter measurement. Measurements are all assumed to be made in the time period $T_h = 1/30$ s. The quoted values are all relative (measurement interval to measurement interval). The linear tolerance for the beam energy assumes a dispersion of 2.5 cm/%. The tolerances on the beam position and angle measurements depend on the relative efficiency of opposite detector pairs being corrected at the 5×10^{-3} level. The linear tolerance for the beam angle assumes two measurements 10 m apart.

Incident energy	1×10^{-5} (25 μm)
Beam diameter at target	1 mm
Beam charge	4×10^{-5}
Beam position at target	800 μm
Beam angle at target	14 μr (100 μm)
Detector asymmetry	5×10^{-3}

$$
\begin{aligned}
A_{f,i} &= \left\{ Y_+ \left(1 + \frac{1}{Y}\frac{\partial Y}{\partial \alpha_i}\delta\alpha_i \right) - Y_- \left(1 - \frac{1}{Y}\frac{\partial Y}{\partial \alpha_i}\delta\alpha_i \right) \right\} \cdot \\
&\qquad \left\{ Y_+ \left(1 + \frac{1}{Y}\frac{\partial Y}{\partial \alpha_i}\delta\alpha_i \right) + Y_- \left(1 - \frac{1}{Y}\frac{\partial Y}{\partial \alpha_i}\delta\alpha_i \right) \right\}^{-1} \\
&\cong \frac{1}{Y}\frac{\partial Y}{\partial \alpha_i}\delta\alpha_i .
\end{aligned}
$$

This expression is written to first order in $\delta\alpha_i$ where the α_i are parameters such as the beam energy, etc. Each of the types of parameter variation are considered below. The required resolutions of the measurement devices for the various parameters are listed in Table 4.

The beam energy enters the yield through the cross section; the derivative of the cross section with respect to energy is

$$\left| \frac{E_k}{\sigma}\frac{\partial \sigma}{\partial E_k} \right| \cong 4$$

for the kinematics of this measurement. Therefor $\delta E_k / E_k$ must be measured to 1×10^{-5} in time T_h.

The beam "diameter" (r.m.s. size) also enters directly – through the effective solid angle. If the beam changes its diameter in a helicity- correlated manner, a false asymmetry will be generated as the solid angle is actually smaller for a larger beam (of the same

current). In the case of a uniform beam of diameter d:

$$\left|\frac{d}{\Delta\Omega}\frac{\partial\Delta\Omega}{\partial d}\right| = \frac{1}{4}\left(\frac{d}{r_0}\right)^2$$

where r_0 is the distance from the beam to the solid angle defining aperture. Assuming even a (defocussed) CEBAF beam diameter of $d = 1$ mm and $r_0 = 20$ cm for the proposed apparatus, $\delta d/d$ must be measured at only about the 100% level. Therefore the effect of the beam size is not significant.

The final parameter which enters the asymmetry directly is the beam intensity. If there is a systematic change in intensity from one helicity to the other, and the intensities are measured with some non-zero helicity-correlated precision, there will be a false asymmetry. However, the relative change in intensity in times on the order of the measurement time is not expected to be large; it was $\sim 1 \times 10^{-2}$ in the Bates ^{12}C experiment [Ku90]. There are actually two contributions from correlated intensity changes: a direct uncertainty in the asymmetry resulting from the uncertainty in the intensity; and a contribution due to the change in detector deadtime in the counting mode. The direct contribution is simply

$$\frac{I}{Y}\frac{\partial Y}{\partial I}\delta I = 1$$

hence $\delta I/I = \delta Q/Q = 4 \times 10^{-5}$ as above (in the absence of non-linearities in the charge measuring device – see Section 4.4.3). The indirect contribution through changes in deadtime is not as important here as in the direct contribution to the noise since in this case they come in multiplied by $\delta I/I$.

The remaining false asymmetries all require a combination of effects, for example, a helicity-correlated beam motion and an (uncorrelated) asymmetry in the spectrometer acceptance. To first order, changes in the beam position and angle are compensated by a perfectly symmetric detector. For the purposes of illustration consider a helicity-correlated beam motion or angle change in the plane of two opposite detectors ("L" and "R") with identical acceptances. In the case of beam translation the changes in solid angle are compensated, one side to the other, and in the case of changes in the beam angle, the increased cross section on one side compensates the reduced cross section on the other. However, the opposite segments of the detector will not be perfectly matched. The general form of such effects is

$$\begin{aligned} A &= \left\{\left[Y_{+R}(1+\frac{1}{Y}\frac{\partial Y}{\partial\alpha}\delta\alpha)(1+\epsilon) + Y_{+L}(1-\frac{1}{Y}\frac{\partial Y}{\partial\alpha}\delta\alpha)(1-\epsilon)\right] - \right. \\ &\qquad \left.\left[Y_{-R}(1-\frac{1}{Y}\frac{\partial Y}{\partial\alpha}\delta\alpha)(1+\epsilon) + Y_{-L}(1+\frac{1}{Y}\frac{\partial Y}{\partial\alpha}\delta\alpha)(1-\epsilon)\right]\right\}\cdot\{\text{“}sum\text{”}\}^{-1} \\ &\cong \frac{1}{Y}\frac{\partial Y}{\partial\alpha}\,\delta\alpha\cdot\epsilon \end{aligned}$$

for

$$Y_{+R} = Y_{+L} = Y_{-R} = Y_{-L}$$

where the beam position or angle is represented by α and the efficiency asymmetry for the two detectors is ϵ. For the case of changes in beam position

$$\left|\frac{1}{\Delta\Omega}\frac{\partial\Delta\Omega}{\partial r}\right| = \frac{2}{r_0}$$

where r_0 is again the distance to the solid angle defining aperture. For the case of changes in the angle of the beam with respect to the nominal

$$\left|\frac{1}{\sigma}\frac{\partial\sigma}{\partial\theta'_k}\right| = 570\ \frac{1}{\text{rad}}$$

for the kinematics of this experiment. If it is further assumed that the detection asymmetry can be reliably determined at the 5×10^{-3} level (corresponding to the statistics of one 1/30 s measuring period for each detector element), the required precisions for beam position and angle measurements (per 1/30 s measuring period) are

$$\begin{aligned}\delta r &= 800\ \mu\text{m}\\ \delta\theta'_k &= 14\ \mu\text{r}\end{aligned}$$

The tolerance for the angle measurement corresponds two beam position monitors each with precision of 100 μm at a separation of 10 m.

Changes in beam shape which preserve the first (beam centroid position) and second (the 'diameter' as discussed above) moments of the beam charge distribution also enter the expression for false asymmetries multiplied by a detector efficiency asymmetry. Such a change could consist of, for example, the third moment simply changing signs. However, such changes result in much smaller asymmetries than those associated with beam diameter changes since they come in like $(d/r_0)^2\epsilon$ and are certainly smaller than the diameter effects for beams of reasonable shape.

If the beam polarization for positive and negative helicities is different the effect on the physics asymmetry is small. Assuming that the average of the two is measured with a polarimeter it enters the *relative* uncertainty in the physics asymmetry (i.e. if the precision of the polarization measurement is n%, the limiting relative precision of the physics asymmetry will be n%). In this experiment the goal for measurement of the beam polarization is 2% (see Section 4.4.2). False asymmetries due to helicity- correlated changes in polarization come in only at the level

$$A_f \sim A^2_{expt}\frac{\delta P}{P}$$

and are thus unimportant.

3.4.7 Non-linearities

A false asymmetry can result from helicity-correlated changes in beam intensity coupled with a non-linear response in either the spectrometer or the beam charge monitor. As an

example, consider the non-linear response of the charge monitor. Suppose that the beam charge Q_0 changes by $\pm\delta Q$ as the helicity changes. If the non-linearity η is defined to be

$$\eta = \left\{ \frac{Q_{meas}}{Q_0} - \left(1 - \frac{\delta Q}{Q_0}\right) \right\} \cdot \left\{ \frac{\delta Q}{Q_0} \right\}^{-2}$$

then

$$A_f \cong \eta \left(\frac{\delta Q}{Q_0} \right)^2 .$$

In the absence of measurements of η, this false asymmetry must be less than 5% of the *overall* uncertainty in the experiment, i.e. about 1×10^{-8}. In the Bates ^{12}C experiment the helicity correlated changes in the beam intensity were reduced to be less than 1×10^{-5} averaged over the whole experiment [Ku90], therefore, the relative difference between the measured and true charges must be less than 1×10^{-8} for relative changes in current of 1×10^{-5} or

$$\eta \frac{\delta Q}{Q_0} \leq 10^{-3}.$$

This typical non-linearity tolerance for charge monitor and spectrometer response (measurement interval to measurement interval) should be relatively easy to meet given the small dynamic range of interest (about 1% from measurement interval to measurement interval).

4 Apparatus

4.1 Magnetic spectrometer

The object of the proposed measurement is the determination of G_E^0 from elastic electron-proton scattering at several values of Q^2 in the range $0.1 \leq Q^2 \leq 0.3$ (GeV/c)^2. Either the electron or the proton could be detected, but the two options make very different demands on a spectrometer. The electrons of interest are at small forward angles and have very high energies. This implies major attendant problems involving backgrounds, spectrometer geometry, and detector shielding [La91]. The proton kinematics, which are listed in Table 5, are much more attractive from the point of view of an experimental measurement. In addition to kinematics, a number of requirements for an optimal spectrometer arise from the small size of the elastic cross section and the presence of competing inelastic processes. These can be summarized:

Table 5: Proton kinematics for the proposed measurement.

$E_e = 2.5$ (GeV)

Q^2 (GeV/c)^2	p_p (MeV/c)	θ_p (deg.)
0.1	320.7	76.8
0.2	459.7	71.4
0.3	570.6	67.3

Extended targets:	Nominal 20 cm length
Very high counting rates:	Only one focal plane measurement/event (no trajectory reconstruction)
Line-of-sight shielding:	Required between target and focal plane
Azimuthal acceptance:	Maximum possible fraction of 2π
Resolution:	$\delta p/p \leq 10\%$
	$\delta\theta \leq 1°$(scattering angle)
Systematic Errors	Symmetric proton detection

4.1.1 Normal-conducting toroidal spectrometer

The desirable features of maximal azimuthal angular acceptance and symmetry make the open geometry of a toroidal spectrometer particularly attractive if a suitable optical configuration can be found [La91].

Optics considerations

Conventional focusing configurations. In first order, the magnetic fields of a simple toroid have a 1/R radial- dependence and a Gaussian longitudinal-dependence (as measured from the median plane normal to the symmetry axis). For a point target, excellent focal behavior (i.e. momentum dispersion along a focal plane with $(x \mid \theta) \sim 0$) can be achieved; but determination of the scattering angle requires the measurement of angles at the location of the focus with wire planes. This latter requirement is an undesirable feature at high event rates. Also, the focusing configuration has very bad extended target (t) characteristics. In a typical example, a matrix element $(x \mid t) \sim 4$ compares with a dispersion $(x \mid \delta) \sim 1$ cm/%. It can be seen that a 5 cm long target would translate into a momentum uncertainty of about 20%.

Non-conventional configurations. Very long targets best can be accommodated if it is possible to constrain the matrix element $(x \mid t) \sim 0$. In the case of a dipole magnet, it can be shown that this condition is always equivalent to $(x \mid x) \sim 0$ (i.e. zero magnification). With this requirement, in general the corresponding $(x \mid \delta)$ and $(x \mid \theta)$ matrix elements both will be non-zero. Every point on the focal plane, which is defined by the $(x \mid t) \sim 0$ condition, will correspond to a family of coordinate pairs (p_0, θ_0). If proton time-of-flight (TOF) is measured by the focal plane position detector, both p_0, and θ_0 can be uniquely determined. This optical configuration is very advantageous for high counting rates, long targets, and the reduction of backgrounds with particle TOF.

Coil design

Because of the toroid 1/R field drop-off and the large initial angles of the protons, a much more compact spectrometer and focal plane are possible if the protons are bent inward toward the symmetry axis rather than away from it. Optical properties similar to those that are possible for inward- bending geometries can also be obtained for out-bending ones, but it requires relatively more current to move the detector location away from target line-of-sight. Also, because the focal plane is located farther from the toroid axis for the out-bender design, more detector area will be required for any given azimuthal acceptance. More shielding will be needed and the device as a whole will be much larger and more expensive.

Suitable coil configurations were explored by tracing particle trajectories through magnetic fields that were calculated analytically for distributions of filamentary currents. Although these analytic fields can be calculated quite rapidly, they can be made to correspond closely to the fields computed for somewhat more realistic uniform current distributions with TOSCA routines. The agreement can be of order parts in 10^3, with an attendant savings of more than a factor of ten in cpu time.

Our present coil configuration is illustrated in Figures 6 and 7. A total of 0.8 MA turns in each of eight symmetrically-placed loops was modeled initially (as shown in Figure 8) by 57 filamentary circuits, which are distributed to approximate an effective uniform current density of 0.56 kA/cm^2 in a cross sectional area of 1425 cm^2. Half of the azimuthal angular range is occupied with conductors. The diameter of the central (axial) aperture is 35 cm.

Figure 9 shows a plot of the median plane magnetic fields, B_y, in one of the eight sectors of the spectrometer. The peak field is on the order of 1.1 tesla. The field drops to zero on the symmetry axis (z), and falls somewhat less rapidly than $1/R$ with increasing radius because of the extended coil.

Trajectories corresponding to $Q^2 = 0.1$, 0.2, and 0.3 (GeV/c)^2, originating at points in a 20 cm long axial target are shown in Figure 10. It can be seen that the distribution of Q^2 along the focal plane is quite independent of where in the target the respective proton originated. This indicates that the desired condition $(x \mid t) \sim 0$ has been achieved.

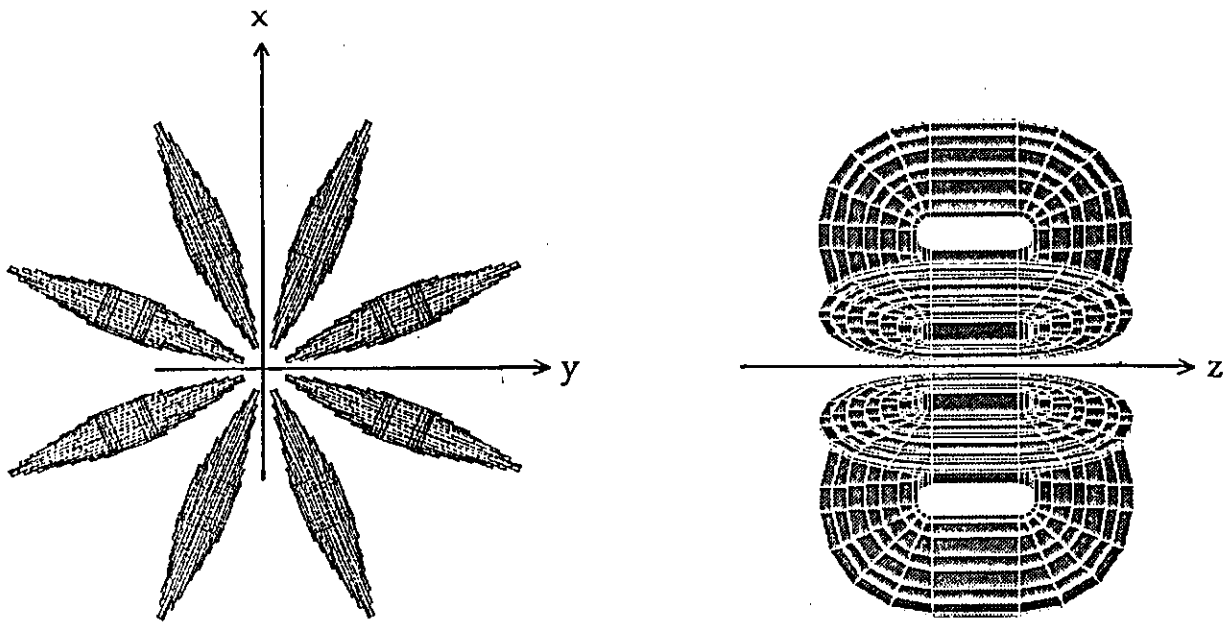

Figure 6: The coil configuration provides eight symmetric spectrometer sectors.

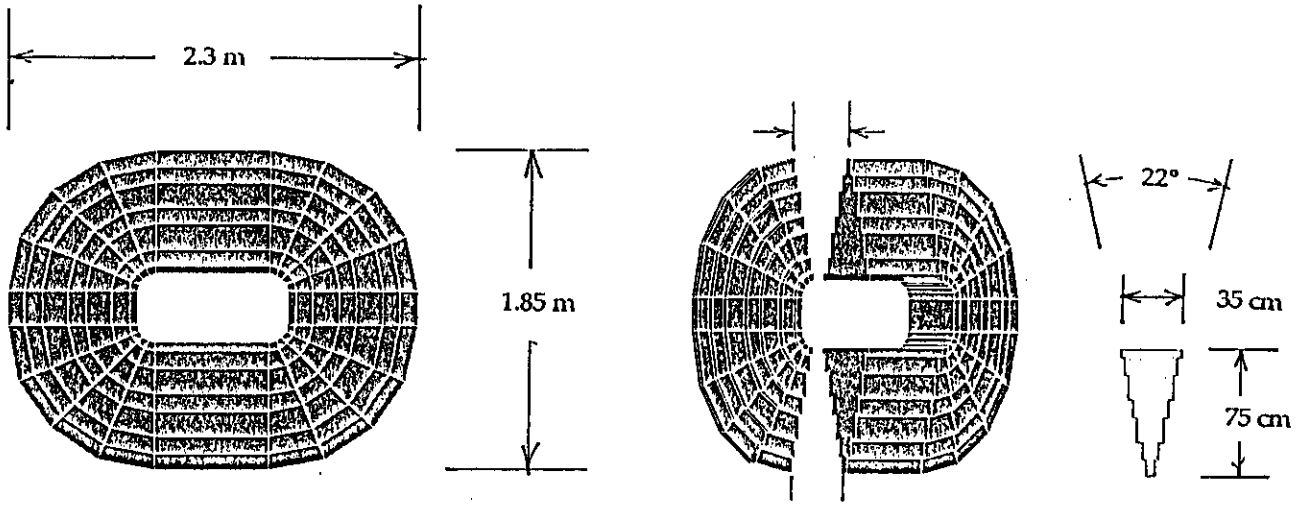

Figure 7: Details of the geometry of one coil.

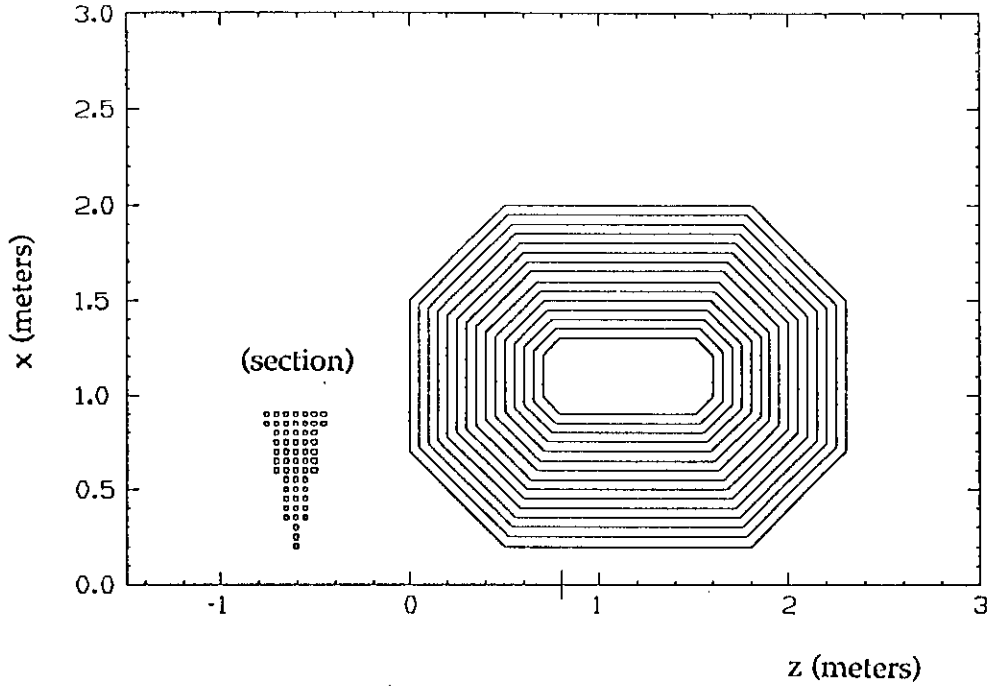

Figure 8: The 57 current filaments used for the initial field and trajectory calculations.

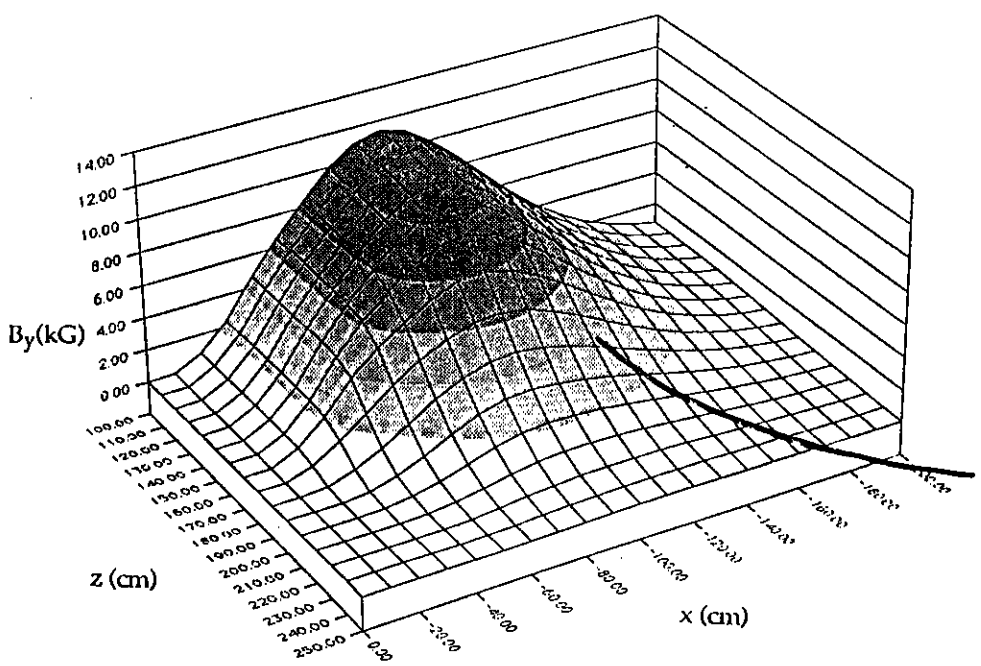

Figure 9: The median plane magnetic fields (B_y). The solid line indicates the location of the focal plane (see Figure 11).

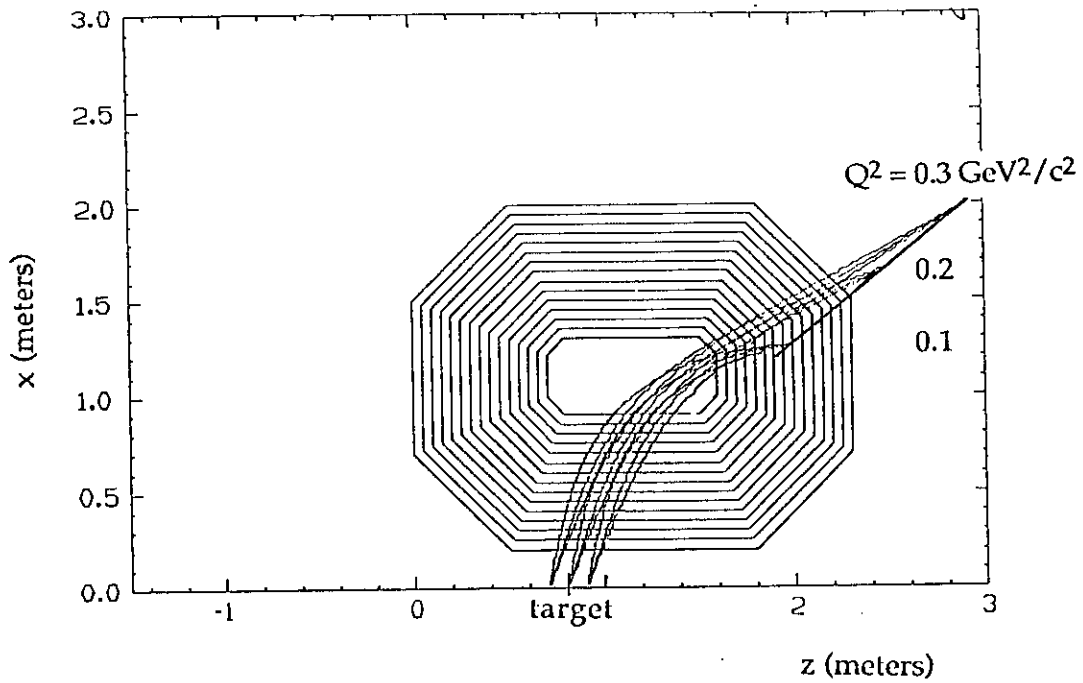

Figure 10: Proton trajectories from a 20 cm long target corresponding to $Q^2 = 0.1$, 0.2, and 0.3 $(\mathrm{GeV/c})^2$.

Trajectories are deflected by angles between 35° and 75°, and can be well shielded from target line-of-sight. The distribution of Q^2 along the focal plane is shown in more detail in Figure 11. The focal plane lies at an angle of 45° relative to the central symmetry axis, and shows only minor deviations from linearity moving toward low Q^2 . The Q^2 dispersion is quite reasonable even at a value of 0.4. This has positive implications for the instrumentation of the focal plane with simple plastic scintillators. We note that some of the detectors will lie between the spectrometer coils where, as can also be seen in Figure 9, the magnetic fields are as high as a few kG. As a result, light guides will be required between the focal plane scintillators and their respective phototubes. The phototubes can be positioned just to the rear of the spectrometer where the fields are very low. Local magnetic shielding of phototubes in the higher field region is a less desirable option because of the potential for asymmetric distortion of the spectrometer optics.

Performance

In order to examine the characteristics of this spectrometer in greater quantitative detail we have attempted to determine effective lowest order matrix elements which relate changes in experimentally observed quantities to changes in initial variables. Of interest are the target-to-focus path length, L, which is related to the time-of-flight, T; the radial distance, R, from the symmetry axis to the point of intersection with the focal plane; and the azimuthal angle, Φ, that the radial vector to the point of intersection makes with the

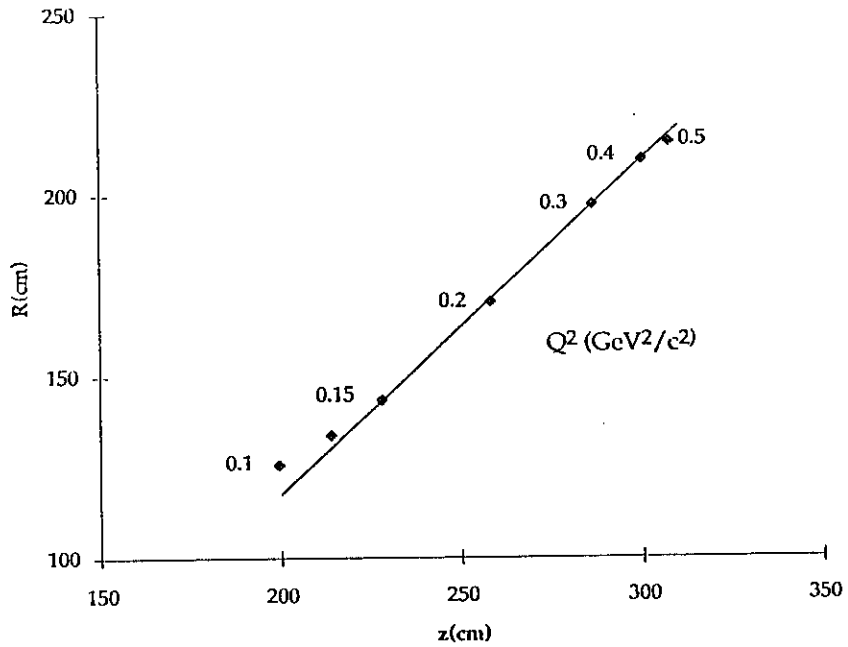

Figure 11: Focal plane detail showing the median plane position coordinates corresponding to $(x \mid t) = 0$ for particles with $0.1 < Q^2 < 0.5$.

median plane of a spectrometer sector (see Figure 12).

It is convenient to expand the matrix elements about a median-plane momentum-dependent central ray corresponding to elastic scattering at the center of the target:

$$\begin{aligned} x_f &= x_0(p_0) + \sum (x \mid y)\Delta y \\ x_0(p_0) &= M^x log(p_0) + B^x \\ (x \mid y) &= m^x_{p\phi} p_0 \phi_0 + m^x_p p_0 + m^x_\phi \phi_0 + b^x \end{aligned}$$

where $x_f = (R, L, \Phi)$, $x_0 = (\theta_0, R_0, L_0, \Phi_0)$, and $y = (\theta, \phi, t, I, ...)$. The coefficients are listed in Table 6, and were obtained from a fit to partial derivatives computed for trajectories corresponding to $Q^2 = 0.1$, 0.2, and 0.3 $(\mathrm{GeV/c})^2$, at $\phi_0 = 0$, and 100 mr. This parameterization was found to provide a very reasonable fit to the calculated data.

The entries of Table 6 were used to generate parametric expressions for R and T in terms of p_0, t_0 and θ_0. R and T are measured experimentally with a scintillator ladder at the focal plane. It is interesting to examine the kinematics listed in Section 3.2 above in the R-T plane shown in Figure 13. Each line corresponds to a constant proton momentum and to a range of scattering angles, θ_0, which increase as one moves to the right. The angles are indicated in the figure by points placed on the lines at one degree intervals. It can be seen that a position measurement at the focal plane selects a family of momenta and angles which can be uniquely separated by the TOF cut. The dotted band about each line indicates the timing uncertainty that arises from the 20 cm length of the target. It is clear that 5 cm wide plastic scintillators would allow $\delta\theta \sim 1°$ scattering angle resolution. Timing

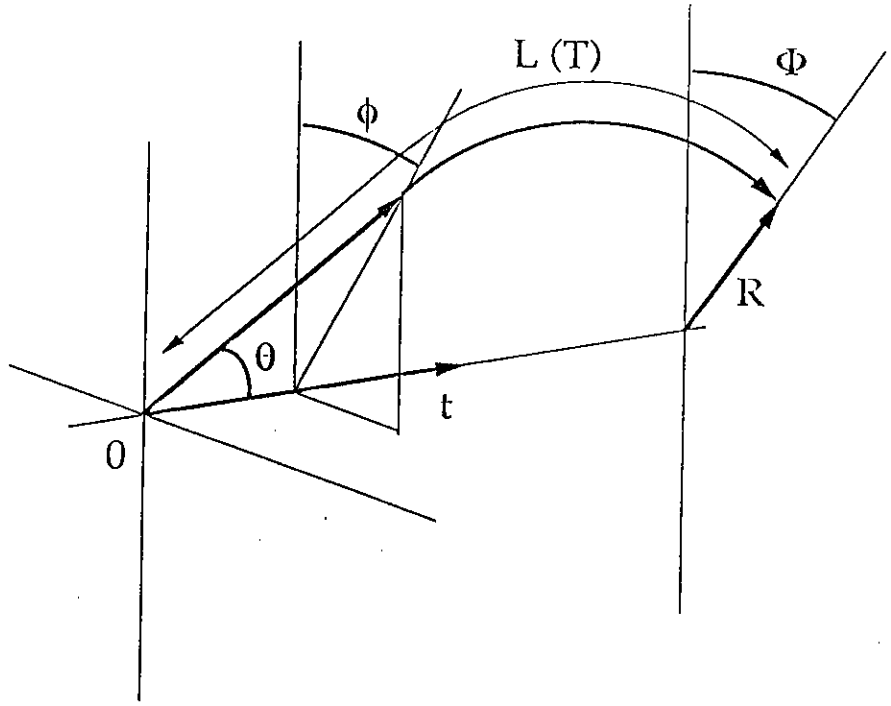

Figure 12: Definition of the coordinate system used in the construction of effective transport matrix elements for the toroid optics.

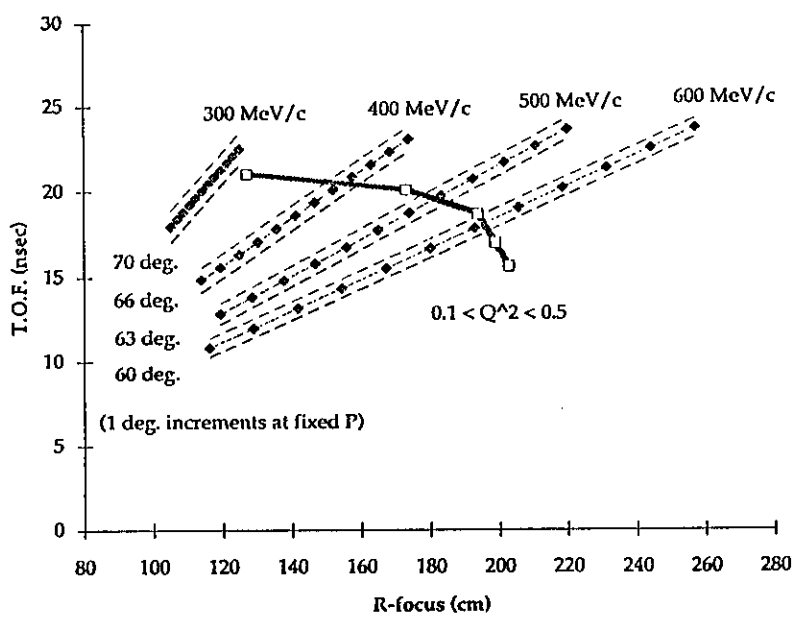

Figure 13: Parity spectrometer optics showing dependences of R and T on p_0 and θ_0. The dashed lines indicate the TOF uncertainty due to the 20 cm long target. The distribution of Q^2 in the $R-T$ space is indicated by the open rectangles.

Table 6: Effective matrix elements for the G_E^0 spectrometer (see text). The uniform dimensions used throughout are: cm; mr; MeV/c; kA.

x_0	M^x	B^x
θ_0	-653.4445475	2979.828704
R_0	274.7195734	-561.1088615
Φ_0	-0.000393192	0.002032471
L_0	356.962726	-690.6985916

$(x\|y)$	$m^x_{p\phi}$	m^x_p	m^x_ϕ	b^x
$(R\|p)$	-1.3349×10^{-6}	0.000865155	0.000156819	0.152625319
$(R\|\theta)$	-8.48292×10^{-7}	0.002104983	9.06809×10^{-5}	-0.52904381
$(R\|\phi)$	-3.42572×10^{-6}	-9.93123×10^{-10}	0.000498398	-1.2821×10^{-6}
$(R\|t)$	-2.39854×10^{-6}	-2.20839×10^{-5}	0.001090477	0.01206395
$(R\|I)$	-1.27663×10^{-6}	0.001136648	0.000307243	-0.195337328
$(L\|p)$	-1.8202×10^{-6}	0.00128534	0.000152364	0.196835327
$(L\|\theta)$	-5.50454×10^{-7}	0.002882462	-0.000109446	-0.650501999
$(L\|\phi)$	-5.44152×10^{-6}	-6.22729×10^{-9}	0.001066426	2.10021×10^{-7}
$(L\|t)$	-2.63371×10^{-6}	-0.000148331	0.001065715	-0.792468467
$(L\|I)$	-1.81857×10^{-6}	0.001652366	0.000420294	-0.290715478
$(\Phi\|p)$	1.14147×10^{-5}	2.82243×10^{-8}	-0.007131859	-1.75533×10^{-5}
$(\Phi\|\theta)$	3.55028×10^{-6}	9.71148×10^{-9}	-0.004002082	-1.02741×10^{-5}
$(\Phi\|\phi)$	-9.06529×10^{-7}	-0.000146882	0.000254907	1.46647937
$(\Phi\|t)$	5.12676×10^{-6}	1.10106×10^{-8}	0.006733662	2.06249×10^{-5}
$(\Phi\|I)$	3.50361×10^{-6}	8.7427×10^{-9}	-0.002549735	-6.2948×10^{-6}

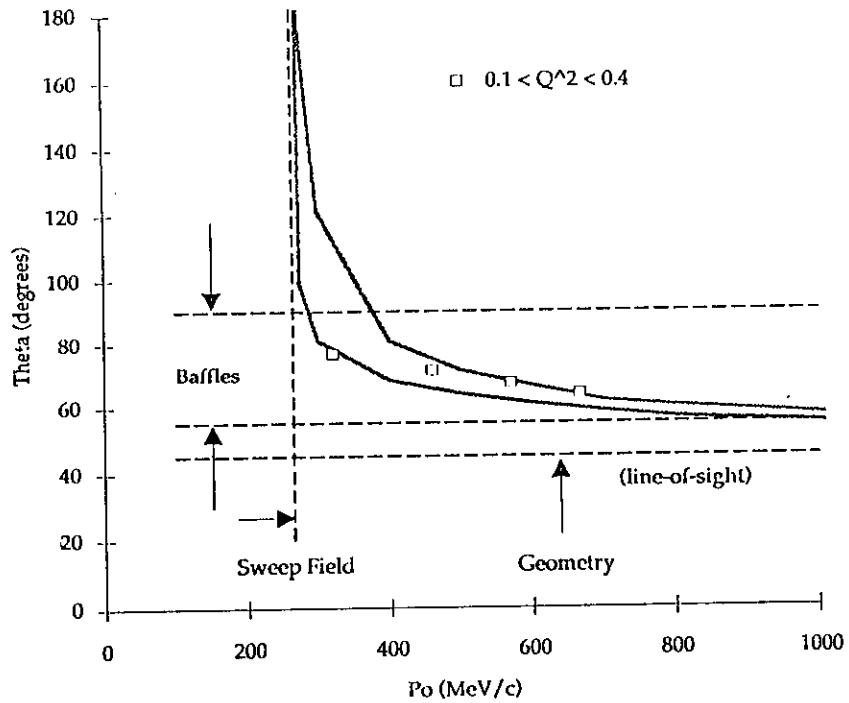

Figure 14: Focal plane momentum and scattering-angle acceptance of the spectrometer.

resolution much better than about 1 nsec is not justified for long targets. Timing at this level would correspond to momentum resolution between about 5% and 9% depending on the momentum. Figure 13 also specifies the location of particular values of Q^2 in the R-T plane in increments of 0.1 $(\mathrm{GeV/c})^2$. In the range $0.1<Q^2<0.3$ $(\mathrm{GeV/c})^2$, the Q^2 resolution is on the order of 0.01 to 0.02 $(\mathrm{GeV/c})^2$.

The ranges of momenta and scattering angles that can reach the focal plane detectors from the target are important from the point of view of potential background processes. At low momenta, independent of angle, it is not possible for particles to make it to the detectors because of the sweeping effect of the spectrometer fields. It is also true that at small enough angles, even very high momenta will be precluded because of the location of the detector plane at relatively large angles with respect to the target. If intercepting baffles are placed inside the spectrometer, additional large-momentum small-angle (including line-of-sight) trajectories can be eliminated, as can additional large-angle small-momentum ones. These observations are summarized in Figure 14. The thick grey lines bound the range of values of (p_0, θ_0) for which the full 20 cm length of the target falls within the spectrometer acceptance. Values corresponding to $Q^2 = 0.1$ to 0.4 are indicated, as are the bounds on the acceptance imposed by sweep fields, spectrometer geometry, and baffles.

It is of interest to examine the azimuthal distribution of trajectories at the focal plane. Figure 15 shows the location of ray intercepts in one sector corresponding to $0.1 < Q^2 < 0.3$ $(\mathrm{GeV/c})^2$ and $-200 < \phi_0 < +200$ mr (i.e. $\pm 11.25°$, for a total 8-sector azimuthal acceptance of π). If the radial dependence of the magnetic fields were uniform in ϕ, the Q^2 curves would appear to be arcs of circles. Fields near the conductors are somewhat higher than those on the median plane and bend nearby trajectories more strongly, giving rise to the

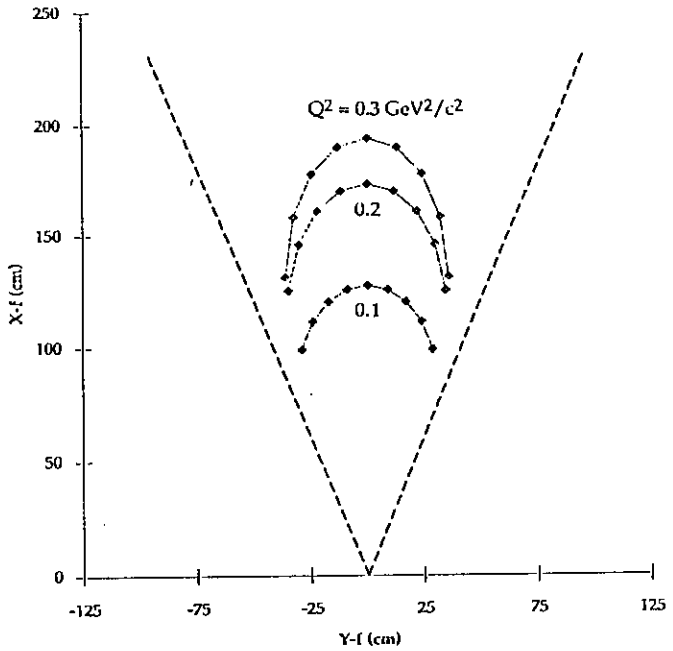

Figure 15: Azimuthal (end-on) view of the focal region of one sector showing curves corresponding to $Q^2 = 0.1$, 0.2, and 0.3. The points correspond to increments of 50 mr in ϕ_0, and the dashed lines indicate the center lines of the adjacent coil assemblies.

'elliptical' shape that is seen in the figure. This azimuthal field dependence has the effect of reducing the Q^2 dispersion at the edges of the acceptance. The details presented in Figure 16 show that the optics at the limits of the acceptance are also more sensitive to the length of the extended target. We note that in the present example the focal plane position was defined to give $(x \mid t) \sim 0$ on the sector median plane, and that it actually would be more appropriate to define its location to minimize $(x \mid t)$ across the ϕ acceptance of the spectrometer in order to maximize the overall resolution in Q^2 .

Tolerances

Current Stability Requirements The spectrometer is iron-free, and all changes in the current in the coils will result in proportional changes in the magnetic fields that define the optics. The effect of current instabilities on the performance of the device can be investigated by means of the $(x \mid I)$ matrix elements that are listed in Table 6. Figure 17 shows the shift in the location of Q^2 in the R-T plane that is brought about by altering the current by $\pm 1\%$. Current uncertainties at this level appear to effect the Q^2 resolution in about the same degree as the TOF uncertainties associated with a 20 cm target. As can be seen in Figure 18, with current regulation on the order of $\pm 0.1\%$, the associated degradation in resolution becomes negligible relative to other effects.

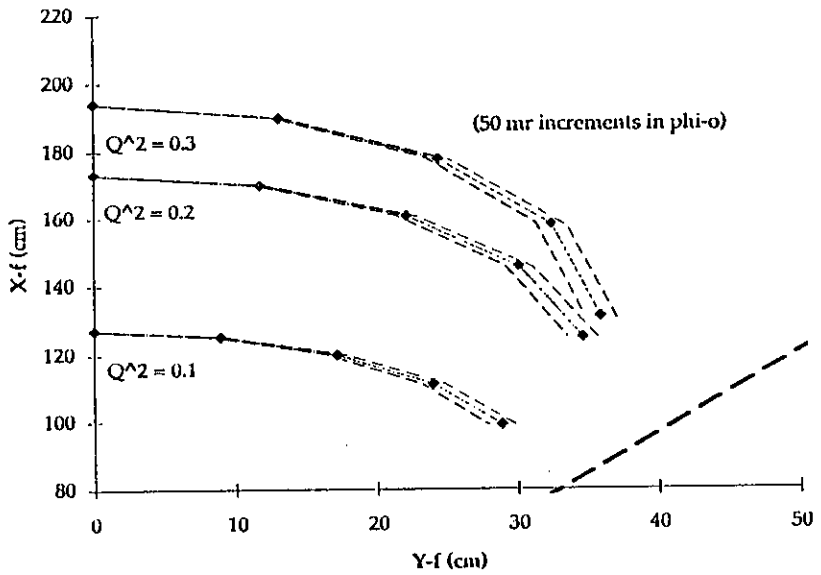

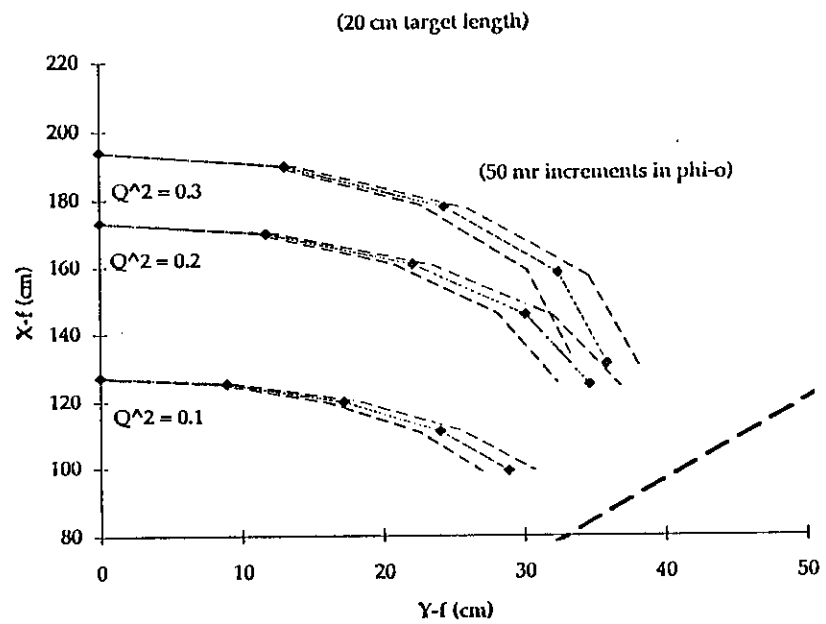

Figure 16: Azimuthal view of the focal region as in Figure 15. Detail showing the effect of 10- and 20-cm target lengths.

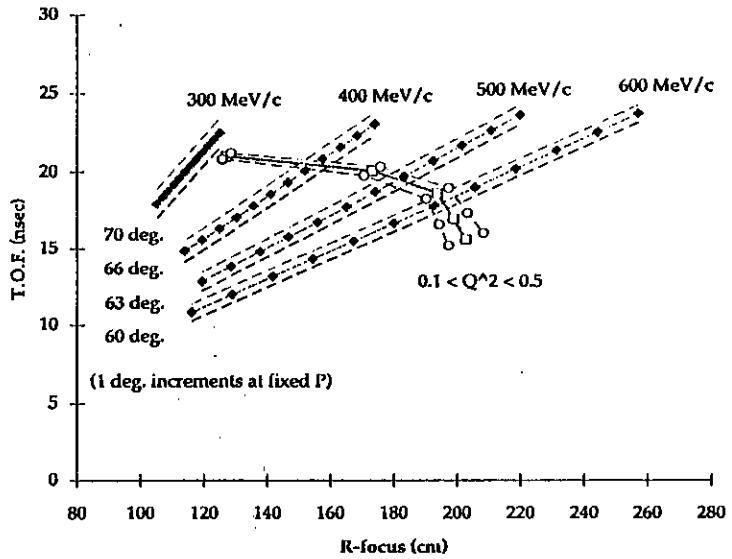

Figure 17: The change in the location of Q^2 in the R-T plane corresponding to current variations of $\pm 1\%$.

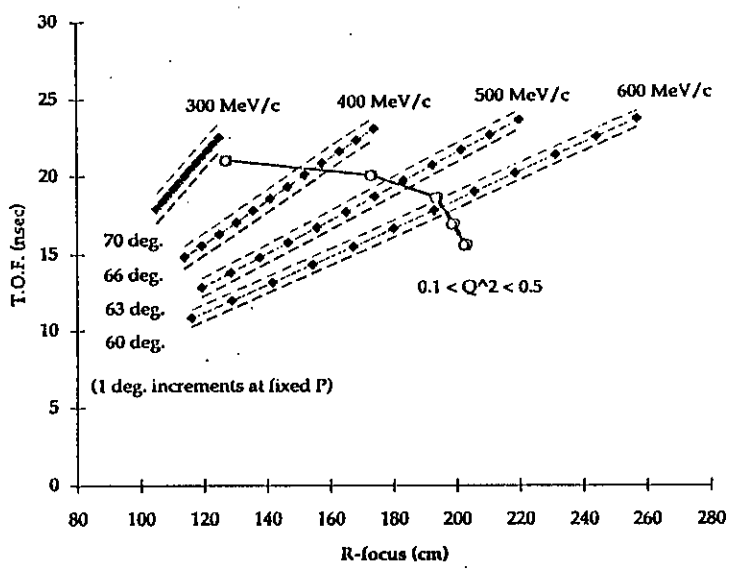

Figure 18: The change in the location of Q^2 in the R-T plane corresponding to current variations of $\pm 0.1\%$.

Table 7: Alignment tolerances (one coil displaced).

Displacement	$\int \lvert B \rvert dL$ (tesla · meter) ($\phi = 0°$)	$\int \lvert B \rvert dL$ (tesla · meter) ($\phi = 8.5°$)
Reference Trajectory $\Delta x, \Delta y, \Delta z = 0.0$ cm	1.268	1.392
Δx=0.5 cm	1.266 (0.2%)	1.388 (0.3%)
Δx=0.2 cm	1.268 (0.1%)	1.390 (0.14%)
Δy=0.5 cm	1.272 (0.2%)	1.400 (0.6%)
Δy=0.2 cm	1.270 (0.08%)	1.395 (0.2%)
Δz=0.5 cm	1.270 (0.08%)	1.395 (0.3%)
Δz=0.2 cm	1.269 (0.0%)	1.393 (0.07%)

Alignment/Deflection Tolerances A realistic evaluation of permissible deviations in the positions of the elements that make up the spectrometer and the detector array will be an important part of the design process. It is possible to obtain a rough indication of the sensitivity of the optics to misalignments or deflections in the coils of the toroid by examining corresponding differential changes in the magnetic fields along typical particle trajectories. From the discussion above, it might be expected that integral field deviations at the level of $\pm 0.1\%$ will not effect the Q^2 resolution significantly. The consequences of displacing one of the eight coils of the G_E^0 spectrometer are tabulated in Table 7. The central-trajectory integrals, on the median plane and on a plane rotated 8.5° toward the displaced coil, for shifts of 5 mm and 2 mm along each of the coordinate-axis directions are compared with the unshifted values. It can be seen that even in the most sensitive case, position uncertainties on the order of 1 mm should be tolerable. This does not appear to be a particularly stringent demand on either alignments or deflections for a device of this size.

4.1.2 Realization

Fields/Forces

As indicated earlier, real coils for the G_E^0 spectrometer will have the geometry illustrated in Figures 6 and 7. It is of some interest to examine how well magnetic field calculations for a uniform current density in this configuration can be matched by a filamentary current approximation. We note that the uniform current density is also an approximation to the real windings in that it does not take into account the insulation between conductors or the cooling channels within them. Figure 19 shows a minor modification of the filamentary loop of Figure 8 which produces fields that correspond well with the results of a uniform density field calculation using TOSCA routines. This correspondence is illustrated in Figure 20

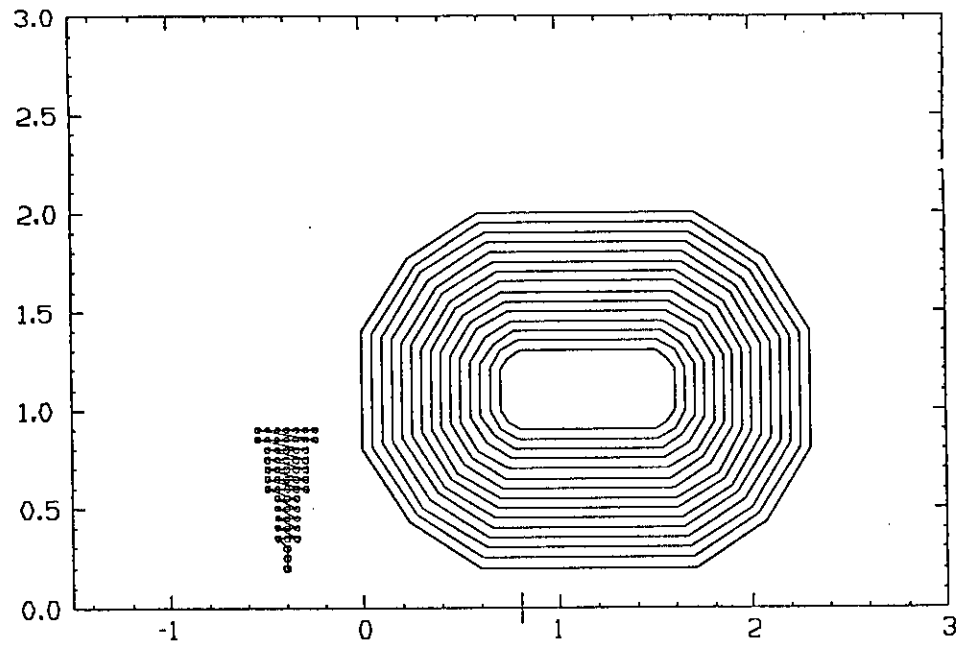

Figure 19: A coil modeled as indicated by 57 current filaments approximates the uniform current distribution configuration shown in Figures 6 and 7.

which shows the relative deviation between the two calculations on the median plane at z = 115 cm. Even close to the coil windings ($\phi = 11.25°$), and at the edge of the spectrometer (z = 215 cm), the agreement is reasonably good as can be seen from Figure 21. Because both the TOSCA calculation and the analytic one are at extremes in approximating the real winding geometry, it is likely that the real fields will fall between the two results.

TOSCA also has been used to calculate the magnetic forces on the coils. Because of the symmetry of the device, all of the forces are radial and lie in directions that tend to expand the individual coils. The resultant forces on the perimeter of one of the coils are shown in Figure 22. Transverse forces can arise if the coils are misaligned significantly; and these will be studied for their possible implications for the coil support system. For reasons of economy the G_E^0 spectrometer will be driven by a single power supply. This will effectively preclude the possibility of large asymmetric transverse forces being produced by the shut-down of one or more of the eight coils independent of the others.

Coils

A section of one of the coils is shown in Figure 23 to illustrate the placement of the windings within a nominal 22.5° wedge. In this case, the copper conductor was taken to be square, 2.3 cm on a side, with a 1.0 cm diameter hole for coolant flow. The individual windings are insulated with a 1.0 mm thick wrapping of epoxy impregnated glass tape, and the steps in

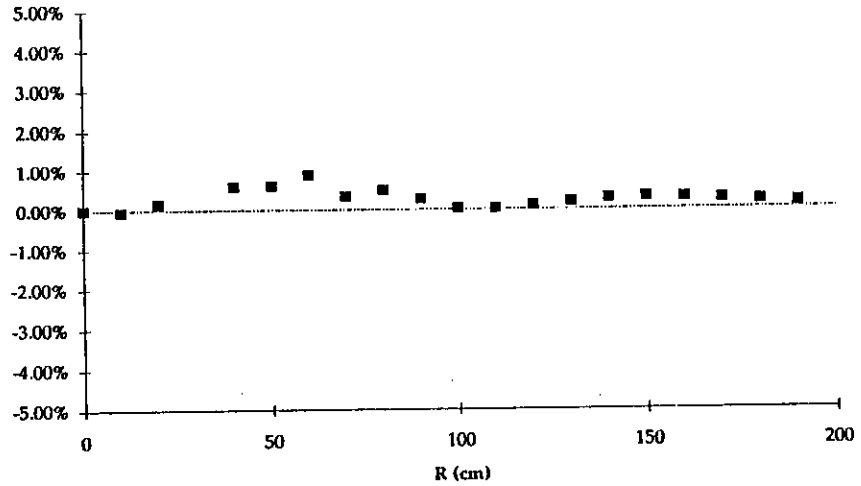

Figure 20: Deviations between TOSCA median-plane magnetic fields and fields calculated analytically for the current filaments of Figure 19, at z = 115 cm.

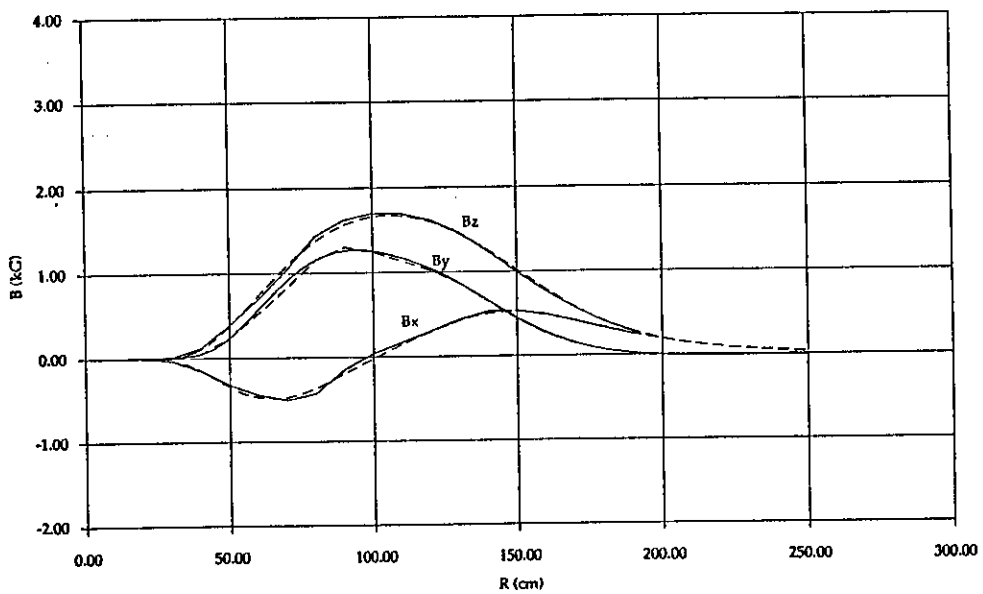

Figure 21: Deviations between TOSCA magnetic fields and fields calculated analytically for the current filaments of Figure 19, at z = 215 cm, and ϕ = 11.25.

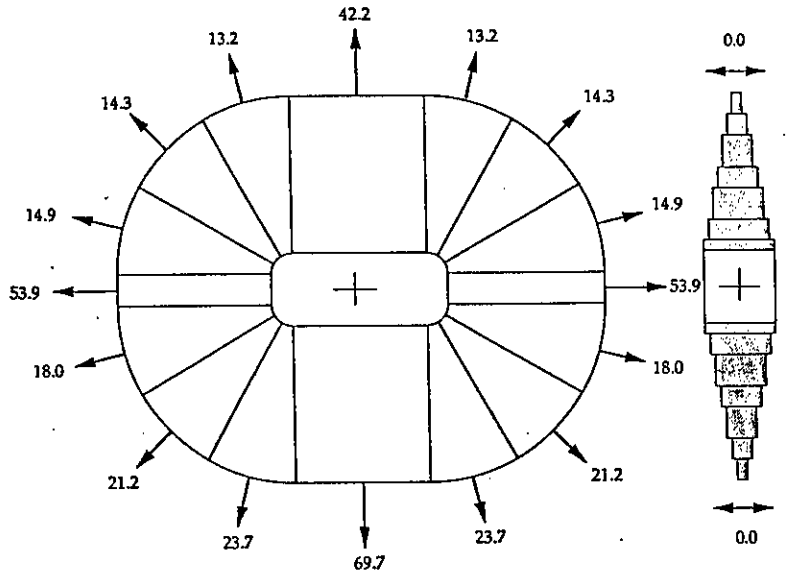

Figure 22: Resultant magnetic forces at the perimeter of one coil assembly (in metric tons/meter).

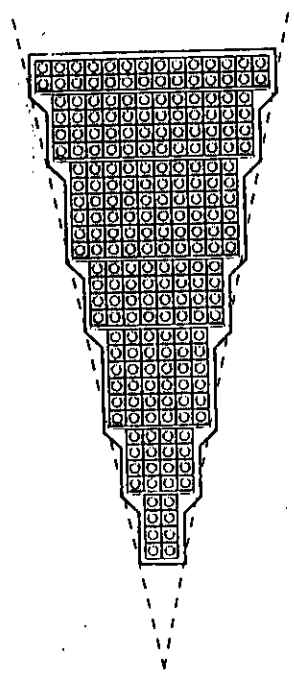

Figure 23: Section of one coil shows the placement of the windings within a nominal 22.5° wedge.

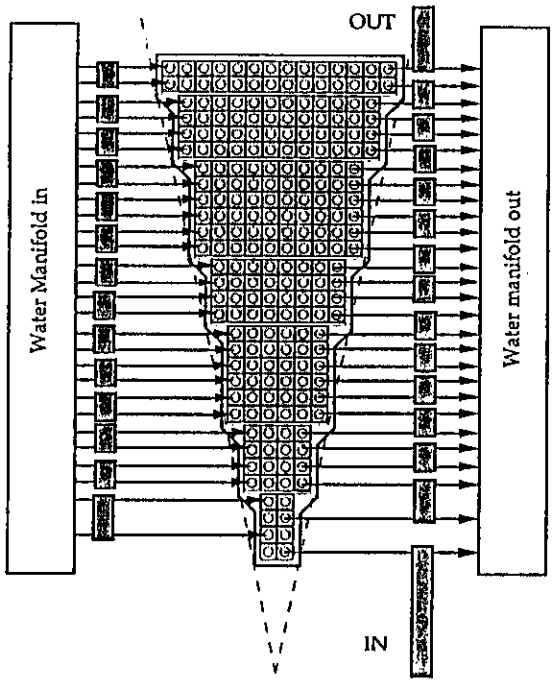

Figure 24: Connection schematic showing the 28 cooling circuits and the associated current straps.

the coil are reinforced with 4 mm thick G10 mounting pads. The entire coil is enclosed in vacuum cast epoxy/glass. The cross sectional area is 1425 cm^2, with an average current density of 0.56 kA/cm^2. The length of conductor in each coil is 901 m wound in 228 turns in 30 layers having a resistance of 0.04 Ω. A current of 3.5 kA at 140 V is required, with a maximum power demand of 490 kW for each coil. If one assumes a coolant pressure drop of 60 psi, and a temperature rise of 40 F, it will be necessary to divide each coil into 28 cooling circuits with individual flow rates of 3.35 gpm. Total water requirements for all eight coils will amount to 750 gpm. The water and power connection scheme is shown in Figure 24 Each layer of the coil is wound from an individual segment of conductor, with connections to the coolant input manifold on one side of the coil, and to the output manifold on the other. The current circuit is made by strapping adjacent conductors on alternate sides. Figure 25 shows the location of these connections on the spectrometer. They are removed from proximity to the particle trajectories, and are readily accessible for assembly and maintenance.

The total power that will be needed by the spectrometer is about 3.9 MW. A single 28 kA, 140V supply will be the most cost effective way to meet these requirements, and if its efficiency at full load is 85 %, the maximum power from the line will be on the order of 4.6 MW. At a nominal cost of \$85/MW-hr, full power operation will cost almost \$400/hr. It should not be difficult to obtain long term current regulation on the order of 5×10^{-4} in a supply of this size, but a requirement for the reduction of voltage ripple at the terminals below the level of 2 to 5 % could add significantly to the cost. However, the inductance of this spectrometer is sufficiently large (L$\sim$ 17 mH for each coil) so that terminal ripple of

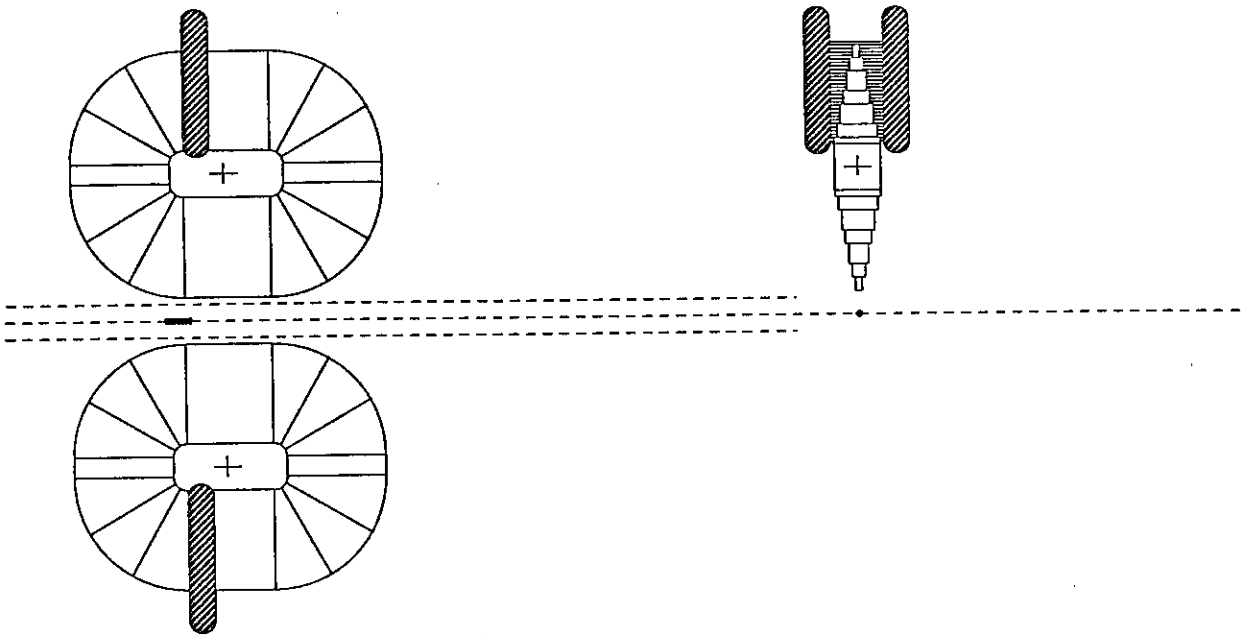

Figure 25: The connections to the water manifold and the current buss are made away from the region of the particle trajectories.

this order will not present a problem.

As an aside we mention that the dimensions of the conductor can have a significant effect on the power and the water cooling requirements, as well as the external connection scheme. For example, the dimensions of the conductor in the above example were chosen to minimize the power consumption under temperature rise and pressure drop constraints. If instead we were to use a standard cross section conductor, 2.5 cm on a side with a 1.4 cm diameter channel, the total power requirements would rise by 640 kW, and the temperature gradient by 15 F, while the water flow rate would drop by 33%. In this case, two layers could be wound from the conductor of each cooling circuit, and all connections would be made on one side of the coil. Attention to the optimization of the coil configuration will be an important part of the engineering design process.

Support scheme

Preliminary estimates of the stiffness of the coil assembly described in the previous section indicate that it may be capable of withstanding the magnetic and gravitational forces to which it will be subjected without the need for additional external reinforcements. An engineering analysis of the coil structure will need to be undertaken to study this question in detail; but if we assume that the present indications regarding stiffness are true, the support system can be relatively simple.

The main requirements are that, with the retention of the specified tolerances, the support structures allow the individual coils to be positioned symmetrically with respect to each other, and permit the device as a whole to be centered accurately on the beam line. It would also be useful to be able to move the spectrometer clear of the beamline during the course of other experiments in Hall C. In conjunction with a consulting mechanical engineer, L. M. Bartoszek of FNAL, we have developed a conceptual design for a support mechanism that appears to meet these requirements. Front, side, and top views of the support design are shown in Figures 26, 27, and 28. Each of the coils is held along its perimeter in an external frame. The symmetry axis of the spectrometer is established by means of a trestle, the cross-beam of which is a cylindrical stainless steel pipe having an internal diameter of 25 cm. The cryogenic target is located within the pipe, and scattered particles enter the spectrometer proper through slots milled in the pipe wall. Because the slots are not large (nominally 6×35 cm), it will be possible to incorporate vacuum windows at this point if it proves to be desirable. The inner edge of each coil-frame is attached to the central pipe with carefully machined longitudinal pivot- pins. This fixes the axial and azimuthal position of each coil, but permits a degree of azimuthal motion at larger radii. The outer edges of the coil-frames are constrained at the front and back of the spectrometer by nominally concentric external support rings. The coil-frames are attached to these rings with brackets that permit fine adjustments of the azimuthal orientation of the coils (i.e. with 'push-push' bolts). The trestle and the outer rings rest on a common rigid base that incorporates a three point leveling mechanism and adjustments that allow the symmetry axis of the spectrometer to be positioned accurately along the beam line. The entire device, which weighs something on the order of 60 tons, can be moved in and out of position along a line normal to the beamline on hillman rollers. The structure will be assembled from above by crane. The base, end- rings and trestle weigh about 17 tons together, and could be fabricated off-site, as could the eight coil/frame assemblies which weigh nearly 5 tons each. In the hall, the base can be put in place, and then each coil can be lowered at the nominally correct angle and pinned to the trestle. The angle adjustment brackets can then be mounted to the rings and the adjusting screws used to take up the weight before the crane is disconnected and used to place the next coil. Assembly could proceed quite rapidly.

The question of the support of detector packages and internal collimation has not been examined in detail. These components will be relatively light and it is expected that they easily can be designed to hang from the members of the main support system. On the other hand, it is possible that shielding the detectors from room backgrounds might require large amounts of material. Support of this heavy detector shielding is best done independently of the spectrometer support because of the alignment demands on the latter. The detector shielding, on independent carriages, can be designed to be moved into position around the spectrometer as required. We anticipate using approximately 1 m of high density concrete to shield the entire spectrometer.

A decision has not been made as to whether this spectrometer will be located upstream or down of the HMS pivot. Figure 29 shows the footprints of the HMS, SOS, and G_E^0 spectrometer in Hall C with the latter device positioned upstream. It is clear that

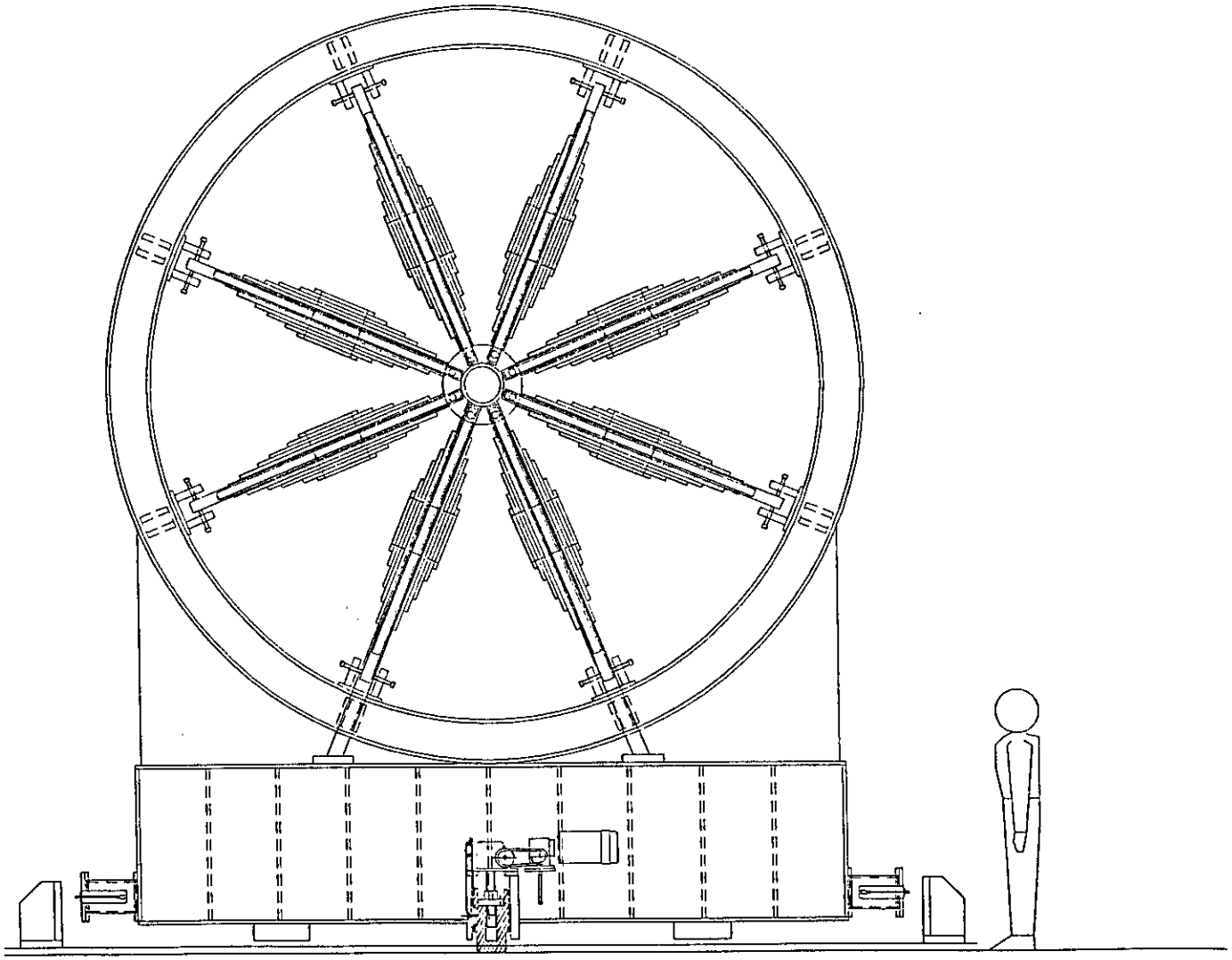

Figure 26: Front view of the G_E^0 spectrometer support system.

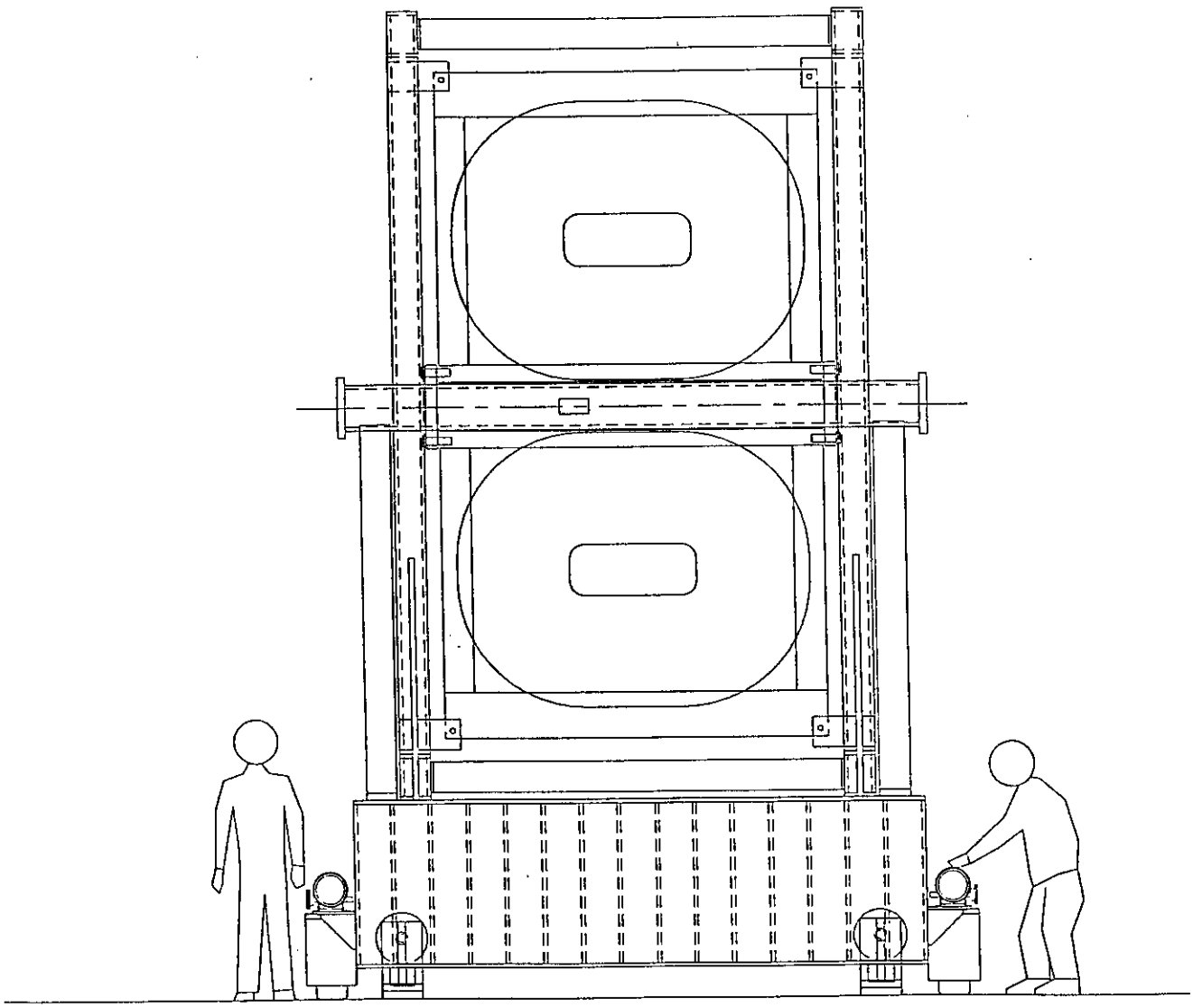

Figure 27: Side view of the G_E^0 spectrometer support system.

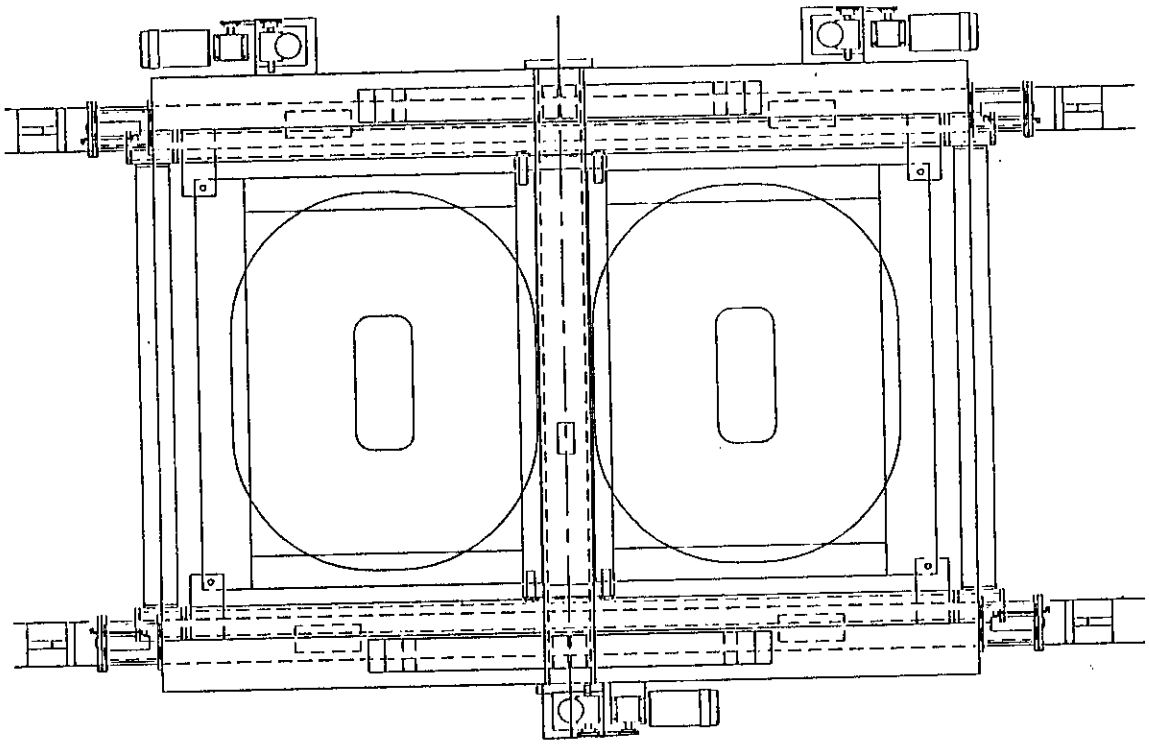

Figure 28: Top view of the G_E^0 spectrometer support system.

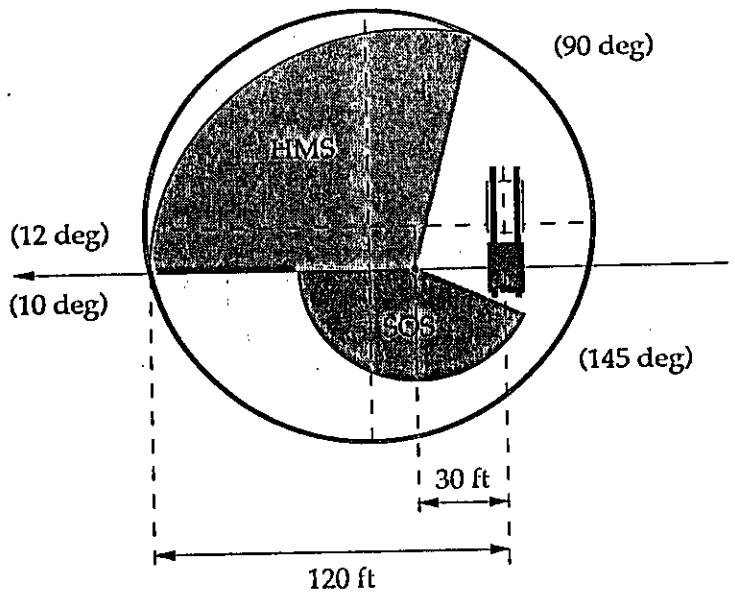

Figure 29: Hall C locations of HMS, SOS, and the G_E^0 spectrometer.

there is ample room to move and park the G_E^0 spectrometer out of the beam, but even if it proves to be convenient, at times, for it to remain in the beam (i.e. with the target removed and the beam transported through it), the SOS would still be able to get as far back as 145°. There is no interference with HMS. The question of shielding the beam transport to the dump needs to be examined further.

4.1.3 Cost estimates

Although it is useful to have an indication of the cost of major components of a new instrument in order to understand its scale, it must be emphasized that, at this early stage, the design is still undergoing development, and not even basic engineering studies have been completed for important parts of the project. Nevertheless, an attempt has been made to assemble a reasonable cost estimate based to as large extent as possible on scaling from previous experiences with similar components, and on preliminary consultations with knowledgeable engineers. The estimate is summarized in Table 9 in Section 5.

4.2 Detectors

4.2.1 Introduction

The detectors will be distributed symmetrically in the eight sectors of the spectrometer. Elastically scattered protons are dispersed in each focal plane according to their momenta (and hence to the their elastic momentum transfer) as shown in Figure 10. The detector for each sector will be divided into 10 elements to provide a nominal resolution in Q^2 of roughly 0.02 GeV^2 and to reduce the elastic rates to a maximum of 1 MHz in each segment. As shown in Figure 15 the lines of constant Q^2 are curved; accordingly each detector element will be crescent shaped.

Momentum and scattering angle, which are correlated for elastic scattering, can be differentiated with a time-of-flight measurement used to supplement the focal plane position (see Figure 13 in Section 4.1). Time-of-flight will therefore allow for identification of inelastic background and of prompt particles such as photons and electrons (and, in this case, pions). The following discussion assumes that individual particles will be counted in the experiment and that their time-of-flight will be measured. Tests performed so far indicate no unexpected limitations in the accuracy of such measurement as compared to an integrating technique (see Section 4.2.5).

As shown in Figure 10, a typical trajectory length for a scattered particle is about 2 meters. Thus particles with $v/c = 1$ (mostly electrons) require no more than 7 nsec to reach the focal plane. The "gamma flash" will be absorbed by shielding the detectors from line- of-sight view of the target. Elastic protons from our experiment, with Q^2 between 0.1 and 0.3 (GeV/c)^2 (corresponding to $v/c = 0.32$ and 0.50), require about 20 ns (see Figure 13).

4.2.2 Detector elements

The individual detector elements will consist of 1 cm thick Bicron BC408 scintillator machined to match the constant Q^2 contours of the focal plane. The scintillators will be viewed at each end by Hammamatsu R-329-02 photomultiplier tubes. Because the low Q^2 detector elements lie in the high field region, light guides will be required to allow positioning of the tubes in a region (downstream of the detector elements) with suitably low fields. The detector elements can easily be arranged such that individual protons do not intersect more than one counter.

4.2.3 Electronics

There are two possible approaches to treating the signals from these detectors: analog; and digital. Analog signal processing techniques have been used in most previous parity-

violation experiments out of necessity. They would be straightforward here as well. The signal from each phototube could be sent to a gated charge pump (to select the desired time-of-flight interval out of the analog signal) and the resulting output integrated during the $1/30^{th}$ of a second that will comprise one measurement interval. However, the high duty factor of the CEBAF accelerator raises the intriguing possibility that the desired accuracy could be achieved using counting techniques, with an attendant improvement in the details of the experimental information available at a modest (if any) increase in the total cost. In the discussion that follows we review the considerations relevant for digital signal processing, and in Section 4.2.5 we present preliminary results from an experimental investigation of the level of accuracy achievable in a counting measurement. If the experiment demonstrates the feasibility of digital signal processing, we will employ this technique for the proposed G_E^0 measurement. If, instead, the experiment shows that digital signal processing is problematic at the level of precision demanded by the G_E^0 experiment, we will switch to analog signal processing.

The 80 curved scintillator elements which make up the detector will be viewed by PMT's at each end. Because of the length and shape of these scintillator bars, pulse heights may be expected to have a large dynamic range. Good timing must be achieved without off-line walk corrections because the desired data rate (44 MHz) makes event-by-event data recording impractical. Constant-fraction discriminators will be used to eliminate walk while commercially available mean-timers will compensate for propagation time through the scintillators.

A specialized circuit board, outlined in Figure 30, will then be used to bin each of these 80 signals into 2 ns time bins for the time-of-flight region of interest. Wider time bins will be used in the background region. The output from these boards will go to a set of scalers. These scalers will essentially store a time-of-flight spectrum for each scintillator. The method of forming and storing these spectra is described below.

The time sorting of the events is achieved by sending each of the 80 mean- timed signals into the serial input of a 16 bit shift register. (This is formed by connecting in series two 8-bit, 700 MHz shift registers, such as SYNERGY Semiconductor's SY100E141). Each signal will be latched at the input to ensure that at most one hit is detected from any scintillator element after a beam pulse. This will simplify the dead-time corrections and render them insensitive to the discriminator widths.

The shift registers and latches will be cleared before the expected arrival time of fast particles (photons and electrons). The registers will then receive a train of 12 clock pulses (covering the duration of the time of interest). This will shift a copy of the input along the series of data bits. At the end of the clock train, the depth of the bits which have been set, if any, will indicate the arrival time of the signal. (Because of the latch the string of set bits will always extend back to the first bit.) The earlier a signal arrives, the more bits it will set before clocking stops. If no signal arrives no bits will be set.

High speed storage of this information can be effected by sending the signals from the shift register bits to individual scaler channels. If a particular bit is set during the

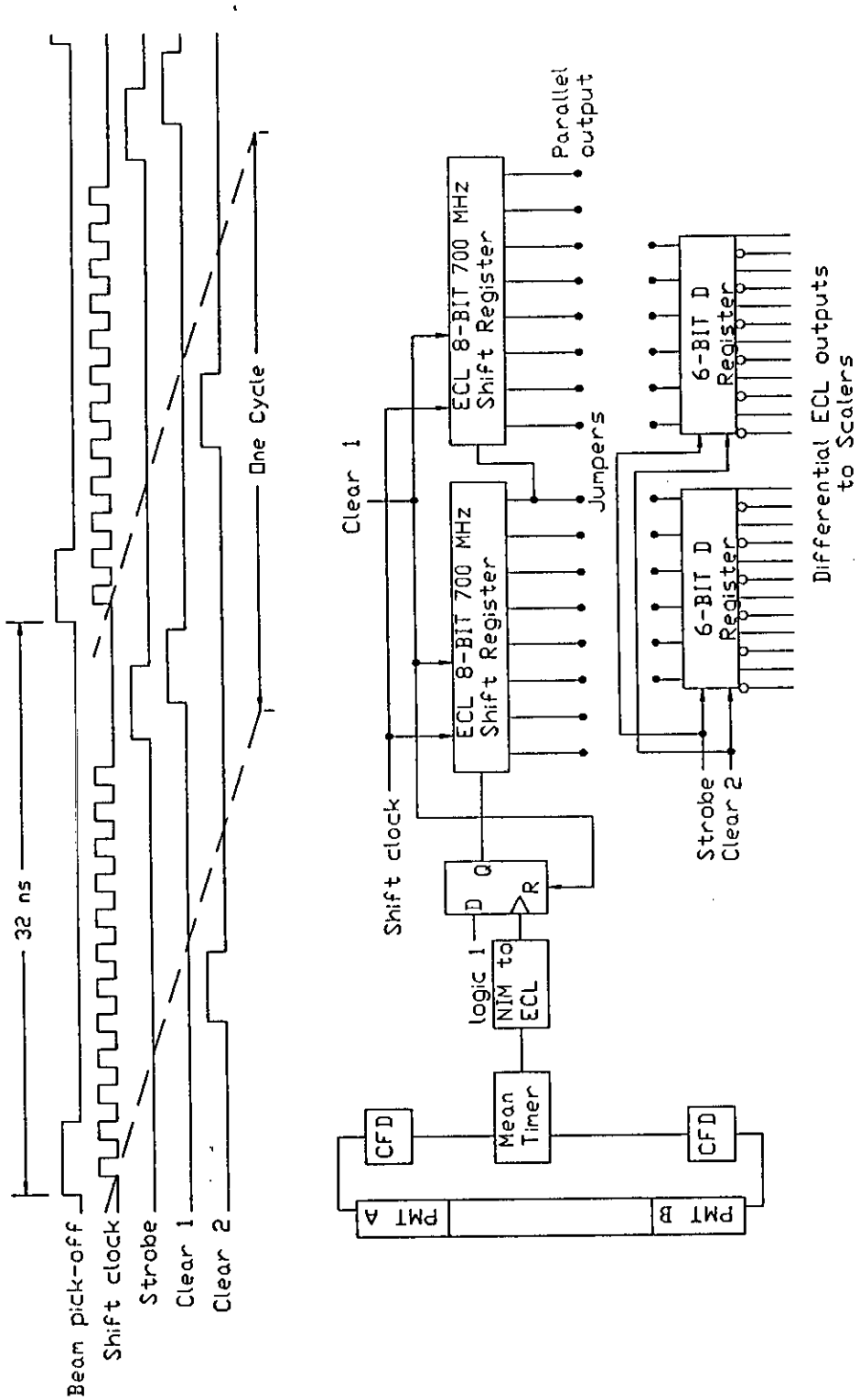

Figure 30: Timing diagram and schematic of the signal processing from detector to scaler. The logic pulses between the dashed lines in the timing diagram indicate signals associated with a given beam pulse. (See text for discussion).

clocking, the corresponding scaler channel will increment exactly once. A set of strobed latches (D flip-flops)will act as an interface between the shift registers and scalers. They will be strobed after the clocking of the shift registers has ended. While the shift registers are cleared for the next beam pulse, the latches will serve to stretch the signal to the scalers out to 10 ns and to drive the ECL lines. They will also eliminate the random time structure of the input to the scalers, keeping the instantaneous rate below 30 MHz.

The difference in counts registered in adjacent scaler channels equals the number of events which arrived within a specific time bin, early enough to increment the first scaler, but too late to increment the second one. If these scalers monitor adjacent bits of the shift register, then the width of the time bin will be one clock 'tick'. Background can be easily monitored in coarser time bins (with a corresponding savings in scaler channels per scintillator) by scaling only a subset of the available shift register bits. Internal jumpers between the shift registers and latches, for example, would allow one to vary the size of the time bins.

The clock signal will be derived from the CEBAF master oscillator signal. The 1500 MHz signal will be divided down to give a 500 MHz clock. Good timing resolution will require that the phase of the clock signal be adjusted to reflect any drift (or abrupt change with helicity reversal) in the arrival time of the beam pulses at the target relative to the oscillator. This will be accomplished by using a beam pickup to measure average phase difference over many beam pulses. This signal will provide feedback to a phase-shifter, which will change the clock phase to null the difference.

It is anticipated that the 2 ns time resolution will be sufficient, even in the time interval corresponding to protons of interest. Should future developments show that an improved resolution in time digitization is merited, a 1 ns binning can be achieved. This would be accomplished by sending each mean-timed signal to the input of two parallel series of shift registers which shift 180° out of phase. Differences in scalers on these interleaved latches would then give the number of hits within a time bin of half the clock period.

4.2.4 Data acquisition

Latching scalers, such as LeCroy 4434 CAMAC scalers, will be used for storage of these time-of-flight spectra. They require only a very short interruption of data-collection at the end of each 1/30 s macropulse. Front-panel signals can be used to load the present scaler readings into latches and clear the scalers. Data taking can then resume in less than 0.4 μs, while the readout of the latched values from the previous macropulse occurs over the CAMAC backplane. Since 1/30 s would be available for readout and writing to tape, the demands on the data- acquisition system are very modest. A possible scenario would be the use of VME-based CPU's with a simple VME branch-driver providing the link to CAMAC.

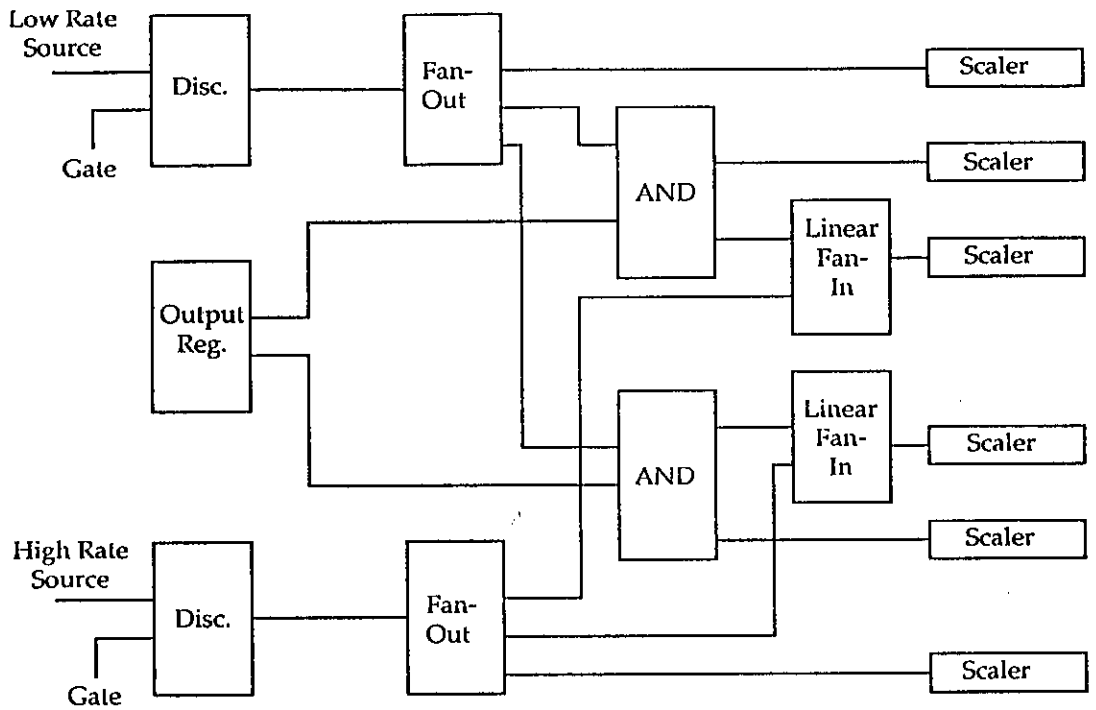

Figure 31: Electronic setup used for the counting tests.

4.2.5 A study of the feasibility of a high-precision counting experiment

To demonstrate the feasibility of performing a counting experiment to the desired degree of precision, we have started an experimental investigation of the possible problems that might be involved. In earlier parity experiments where counting techniques have been used, uncertainties of about 6×10^{-6} have been achieved without any particular problems associated with the measurement technique [Ze89]. Before reaching a final decision regarding counting, we expect to have demonstrated that a high precision counting experiment is feasible by measuring an asymmetry with a precision of about 1×10^{-7} with the electronics to be used in the experiment.

The experimental set up used in the initial tests is shown in Figure 31. Two radioactive sources viewed by plastic scintillators connected to photomultiplier tubes are used to provide random pulses. One of the sources is a high intensity source and is used as the main signal, while the other, much weaker source, produces a controlled asymmetry when added to the main signal. The phototubes are connected to gated discriminators. The main signal is fanned out to two scalers; the weaker signal is added (via a linear fan-in) to the input of one of the scalers during alternate gates.

By separately counting the number of pulses added to the main signal, the actual asymmetry can be determined. If the summed signal measurement is done properly, the calculated asymmetry from this measurement should agree with the actual asymmetry

within statistics. Preliminary results from initial test shows that this is indeed the case, at least at the precision achieved so far. The most recent results are:

$$A = (7.77 \pm 0.28) \times 10^{-5} \quad \text{(Measured)}$$
$$A = 7.85 \times 10^{-5} \quad \text{(Actual)}.$$

The errors shown are due to statistics only. These measurements have been made with the main signal rate of about 230 kHz and using 200 MHz scalers. Thus, at this level of precision there are no obvious difficulties encountered with counting individual particles.

To increase the precision to the level required, several improvements are being made. A different source with a larger activity will be used to generate the main counting signal at rates from 0.1 to 100 MHz. Several channels of scintillator/scalers will be used to investigate further variations in different channels. Ten scintillators counting at 5 MHz each will yield the required statistics in about 500 hours.

4.3 Target

The target will consist of a 20 cm cell of LH_2 with longitudinal circulation at speeds of a few m/s. It is envisioned to run with the same average power density as the SAMPLE target (a 40 μA average beam current on target assuming that the CEBAF beam can be rastered over an area of approximately 0.2 cm^2). The total power deposited in such a target is about 200 W. At the present time it appears that a straightforward modification of the SAMPLE target (including use of cold He gas from the CEBAF system rather than from a stand-alone refrigerator) will be possible.

A schematic view of the target loop as seen by the beam is shown in Figure 32. The hydrogen liquid is circulated by a vaneaxial pump with one cold and one warm bearing. The pump is driven by a motor nominally running at 3600 rpm but with a variable frequency power supply, which should minimize coupling of target vibrations to 60 Hz. The hydrogen is cooled by He gas in a counterflow heat exchanger which has been designed for very high throughput. The heat exchanger is a 15 cm stainless steel pipe with a 10 cm flexible Cu hose running through the center.

The target cell will be a seamless aluminum tube 5 cm in diameter with 0.15 mm wall thickness. Since the target windows will most likely be collimated from the detector, the endcaps can be soldered. The beam will enter the target through a cell of helium gas at the same pressure as the target cell (2 atm). The helium cell is not viewed by the detector; its purpose is to maintain the radius of curvature of the entrance window so that the target length as a function of beam position remains constant. Both the target cell and the He cell will be new items as they will be slightly different in geometry from the SAMPLE target.

The biggest modification to the SAMPLE target will be in the manifold which attaches to the target loop. The manifold must be quite long since the target loop will sit outside of the spectrometer's support frame. We presently envision a series of concentric tubes which

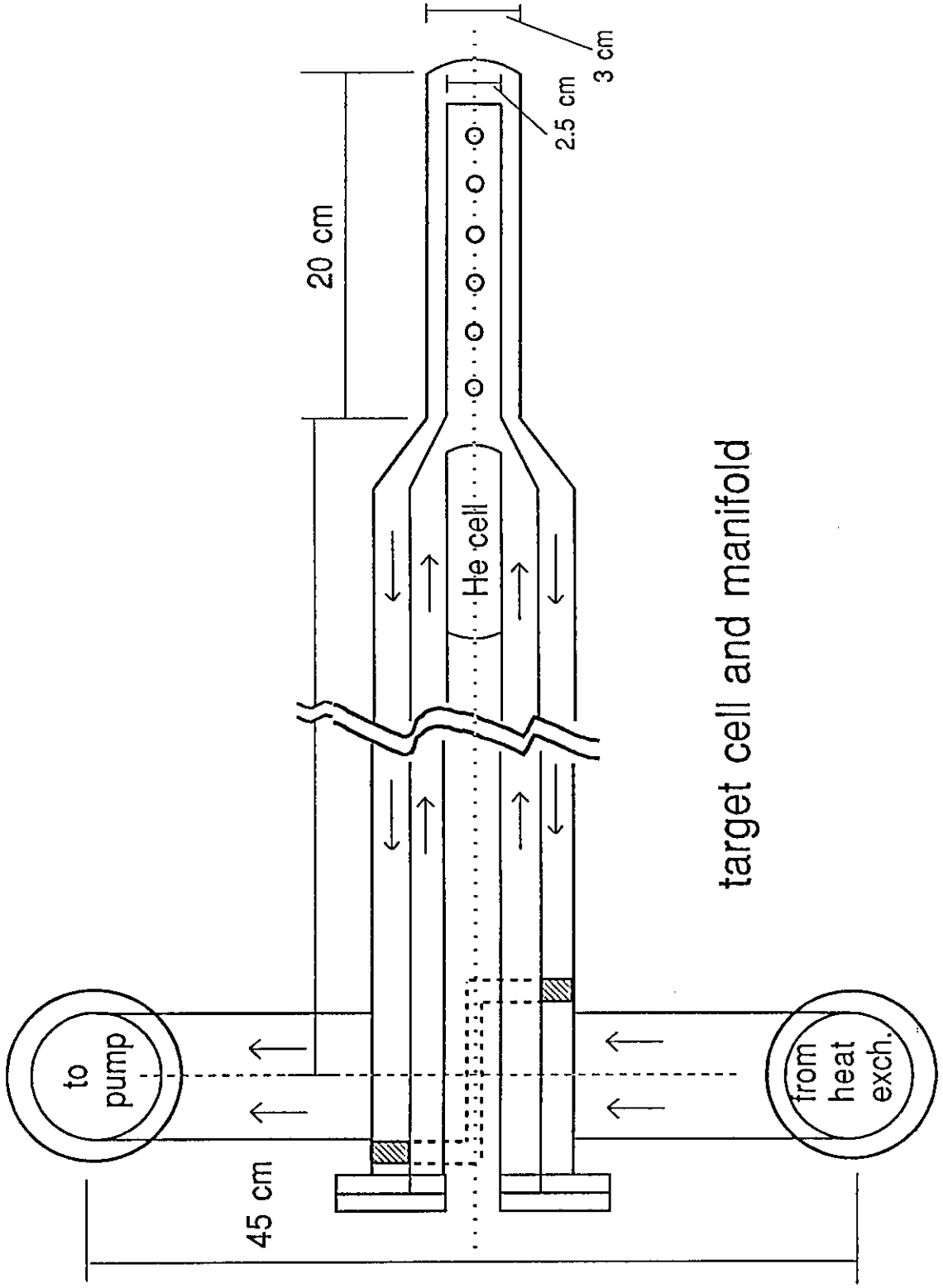

Figure 32: A schematic view of the target.

direct the flow of the LH_2 through the target cell to and from the target loop. With this design a high flow rate can be maintained in the target cell without loss of throughput in the target loop. A schematic view of the manifold as it attaches to the target cell and the remainder of the loop is shown in Figure 33.

The only other modifications to the SAMPLE target will be a new vacuum chamber and scattering chamber. These are both quite straightforward items. The scattering chamber will be a tube with thin windows on the sides for the scattered protons to leave the target. The tube assembly will fit inside the spectrometer's support tube. The vacuum chamber will have a sliding Teflon seal on the top to allow for target positioning while it is cold and under vacuum. This will be a similar design to the SAMPLE vacuum chamber. The entire vacuum chamber/scattering chamber assembly can be rigidly mounted to the spectrometer support stand to allow reproducible alignment when the spectrometer is moved in and out of the beam line.

4.4 The polarized source, accelerator issues, and beam charge, position, and polarization measurement

A polarized source, capable of producing a high intensity beam of electrons with the very high level of stability necessary for the measurement of small, parity-violating asymmetries is a critical component of the G_E^0 experiment. This source must be capable of reversing the helicity of the beam rapidly without changing its other characteristics. In addition, for the measurement proposed here, it must be capable of imposing a microstructure on the beam, filling only every 16th rf bucket, so that it is straightforward to measure the time of flight of the recoiling protons and use it to determine their momenta. The beam from this source must be transported through the accelerator without polarization dilution, and rastered across the target to avoid power density problems. Finally, the charge, position, direction, and polarization of the beam must be measured rapidly and precisely.

In the sections that follow we address these issues, beginning with the source itself and the associated spin manipulator. We also review recent progress in the polarization obtainable from photocathode sources, as these developments can be expected to have a major impact on the experiment proposed. Next we discuss beam transport issues associated with the microstructure required in the beam for the G_E^0 experiment, indicate the rastering scheme that will be employed, and review the issues associated with spin transport through CEBAF and the work in progress to address them. Finally we present our plans for beam polarimetry and for current and position monitoring.

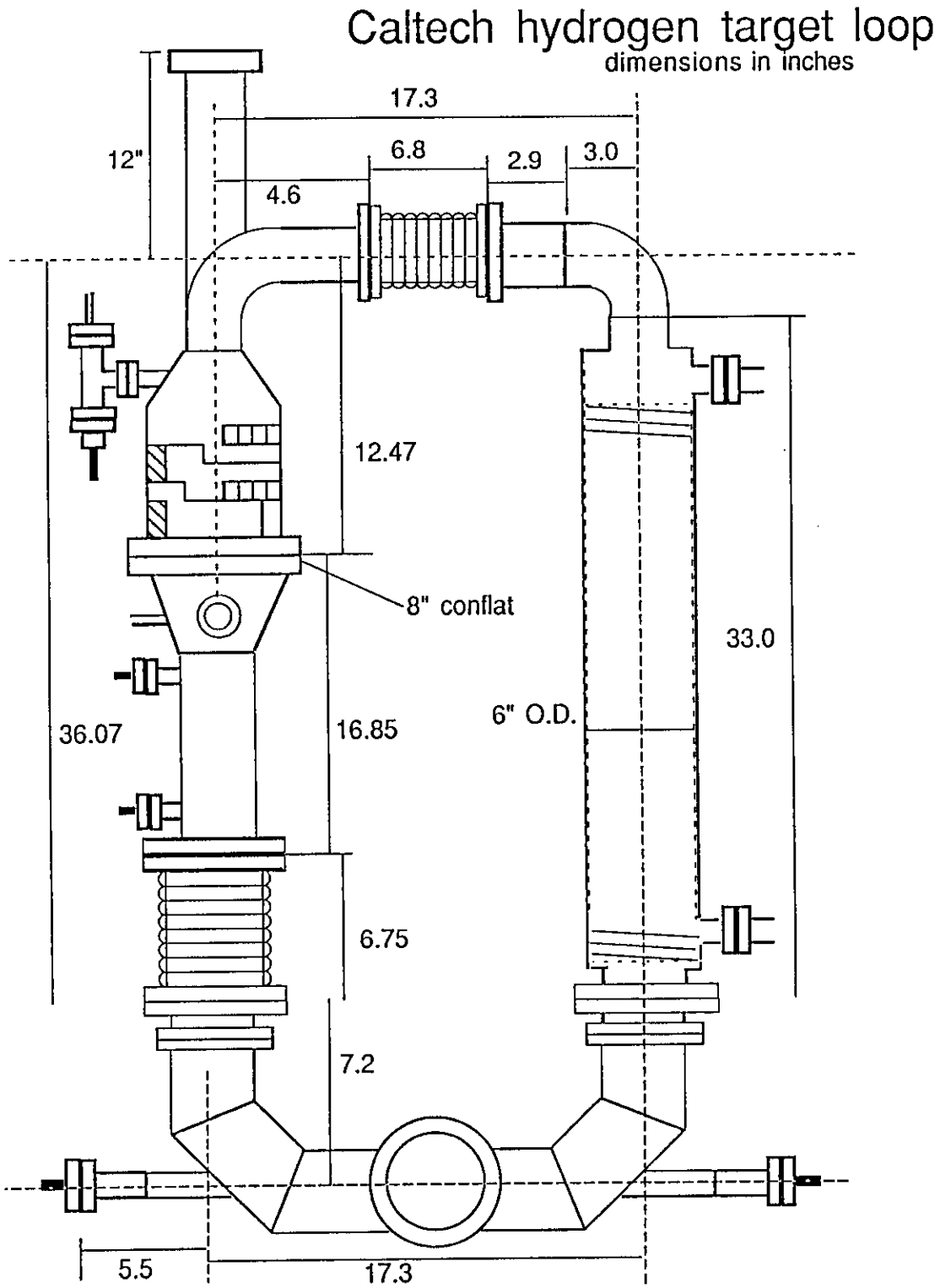

Figure 33: A schematic view of the target loop.

4.4.1 Polarized source

Overview

CEBAF's polarized electron source has been constructed and brought into operation at the University of Illinois [Ca89]; its basic features are shown in Figure 34. This source is a "third–generation" design developed through a close collaboration between C. K. Sinclair of CEBAF and the Illinois group; it incorporates features of the Peggy II [Si76] and SLC [Si81] sources from SLAC as well as new ideas that have evolved since the construction of those sources. The electrostatic design of the source was optimized for the beam requirements of CEBAF. Evident in the drawing are the main ion pump and the subsystems for heat–treating the photocathode to clean it prior to activation and for depositing a layer of cesium on the photocathode surface. Three additional ports on the vacuum chamber (not shown in detail in the section view in the figure) are used for a residual gas analyzer head, a mirror for admitting light during the activation cycle, and a leak valve for admitting NF_3 during the activation cycle.

The source has been mounted on the "table top" that provides support and serves as a base for a specially-constructed bakeout box. This box, which is an insulated cube roughly one meter on a side with its bottom removed, can be lowered into place over the source in a few minutes, permitting the high–temperature bakeouts that are necessary each time the photocathode crystal is changed to take place rapidly and efficiently. The first focusing solenoid, which is mounted roughly midway between the cathode and the tabletop, is a SLAC design that can withstand the full temperatures of the bakeout. The circularly polarized light that excites the photocathode during normal operation enters vertically along the beam axis; the laser beam is separated from the electron beam by a small 90° dipole that is located just below the tabletop.

Status

The initial assembly of the Illinois/CEBAF source was completed in April of 1989. Since that time it has been used mainly to investigate photocathode technology, with an emphasis on chalcopyrite photocathodes as described below, in an effort aimed at improving the maximum polarization available. More recently we have completed the construction of a spin manipulator and a Mott polarimeter. The manipulator can rotate the longitudinal spin orientation of the beam as it emerges from the photocathode into the transverse orientation needed for polarimetry. After passing through the spin rotator and polarimeter, the beam is sent through a double wire scanner system for measuring the beam emittance and finally to a small Faraday cup. These instruments provide the capability for characterizing the beams from the photocathode source completely, permitting a critical evaluation of its performance in different modes of operation.

The spin manipulator will also serve a crucial function when the source is installed

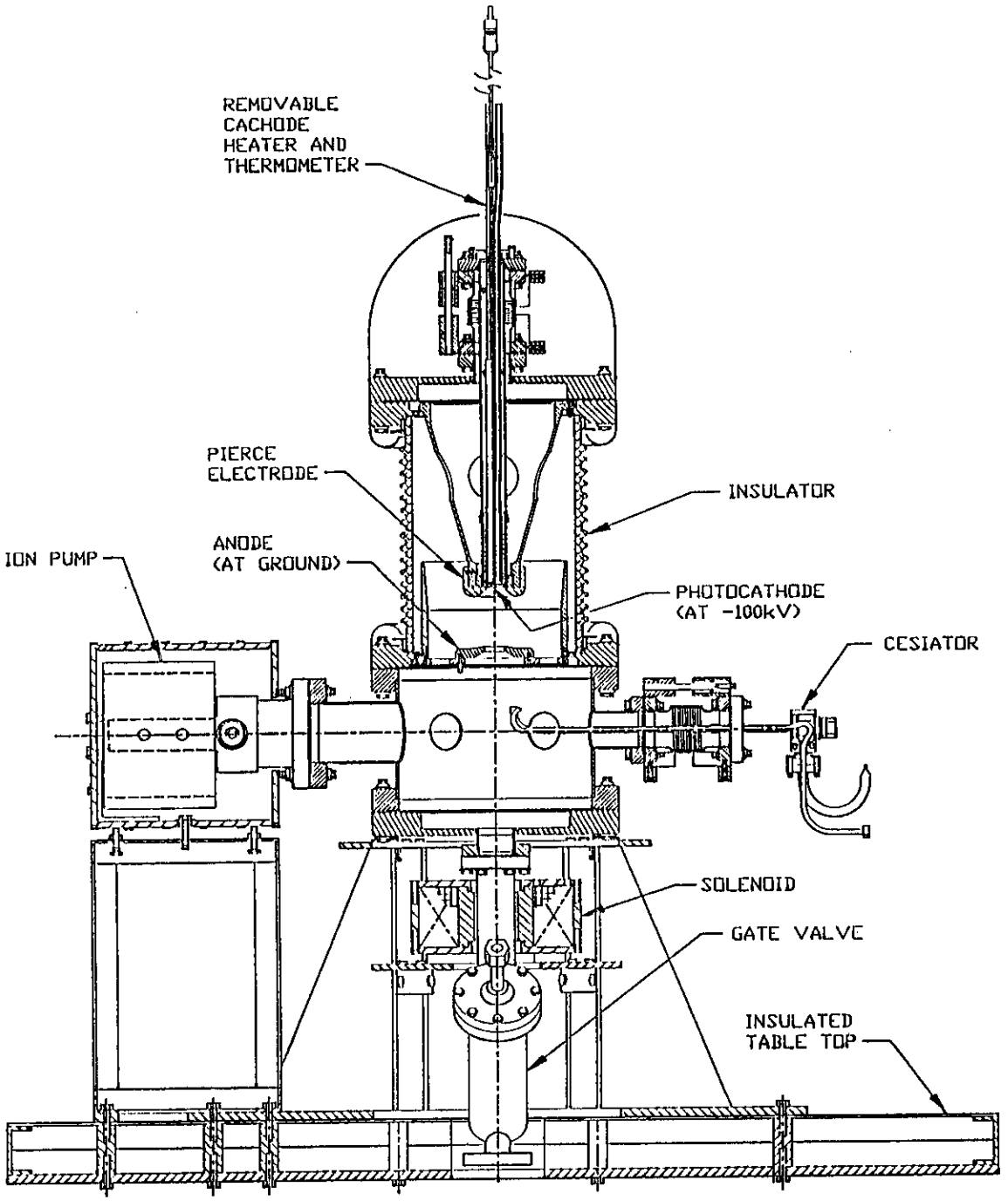

Figure 34: A section view of the Illinois/CEBAF polarized electron source.

at CEBAF, permitting the experimenter to orient the spin direction at the target location in a completely arbitrary manner. This device takes advantage of an important feature of the CEBAF recyclotron, namely that (in contrast to synchrotrons or linac–stretcher ring designs) each electron will follow a precisely-prescribed trajectory during acceleration and transport to the experimental area. For such an accelerator the integral of the magnetic field traversed is a machine constant for a given final energy in the limit of very small beam emittance. To achieve a desired spin orientation on the target it is simply necessary to inject the electrons with their spin oriented in such a way that they emerge as requested at the target after the (fixed and calculable) precession during acceleration and transport. This technique will save the considerable cost and effort involved in building a 4 GeV solenoidal rotator for an experimental area; a spin manipulator at 100 keV is trivial compared to a similar device at 4 GeV.

Figure 35 displays the concept of the spin manipulator and its mechanical realization. It is based on an idea first proposed by Reichert and collaborators at Mainz [Repc,Si89]. The manipulator consists of a pair of electrostatic bends with two pairs of solenoids between them and another two pairs of solenoids following them. The electrostatic bend angle is chosen to provide an exact 90° precession of the spin vector, translating the longitudinal spin direction from the source to perfectly transverse. The field integrals of the central solenoid pair between the electrostatic bends can be adjusted to precess the spin vector's azimuthal angle through angles between 0 and $\pm\pi$. After the beam passes through the second electrostatic bend its spin direction will lie in the vertical plane and can have an arbitrary polar angle, θ, ranging from 0 to $\pm\pi$ relative to the beam direction. The outer solenoid pair between the bends are operated with equal and opposing fields so that they have no net effect on the spin precession; they are adjusted to match the transverse optics of the system for the chosen value of precession. Following the second electrostatic bend there is a second "rotator" that operates in a manner similar to the one between the bends. This rotator takes the beam with a defined polar angle, θ, and rotates it to the desired azimuthal angle, ϕ. The operation of the manipulator has already been demonstrated at Illinois. Figure 36 displays the asymmetry measured for the beam using the Mott polarimeter as a function of both the polar and the azimuthal rotation angles.

Source enhancements for the G_E^0 experiment

A number of enhancements and additions are planned for the Illinois/CEBAF source, including:

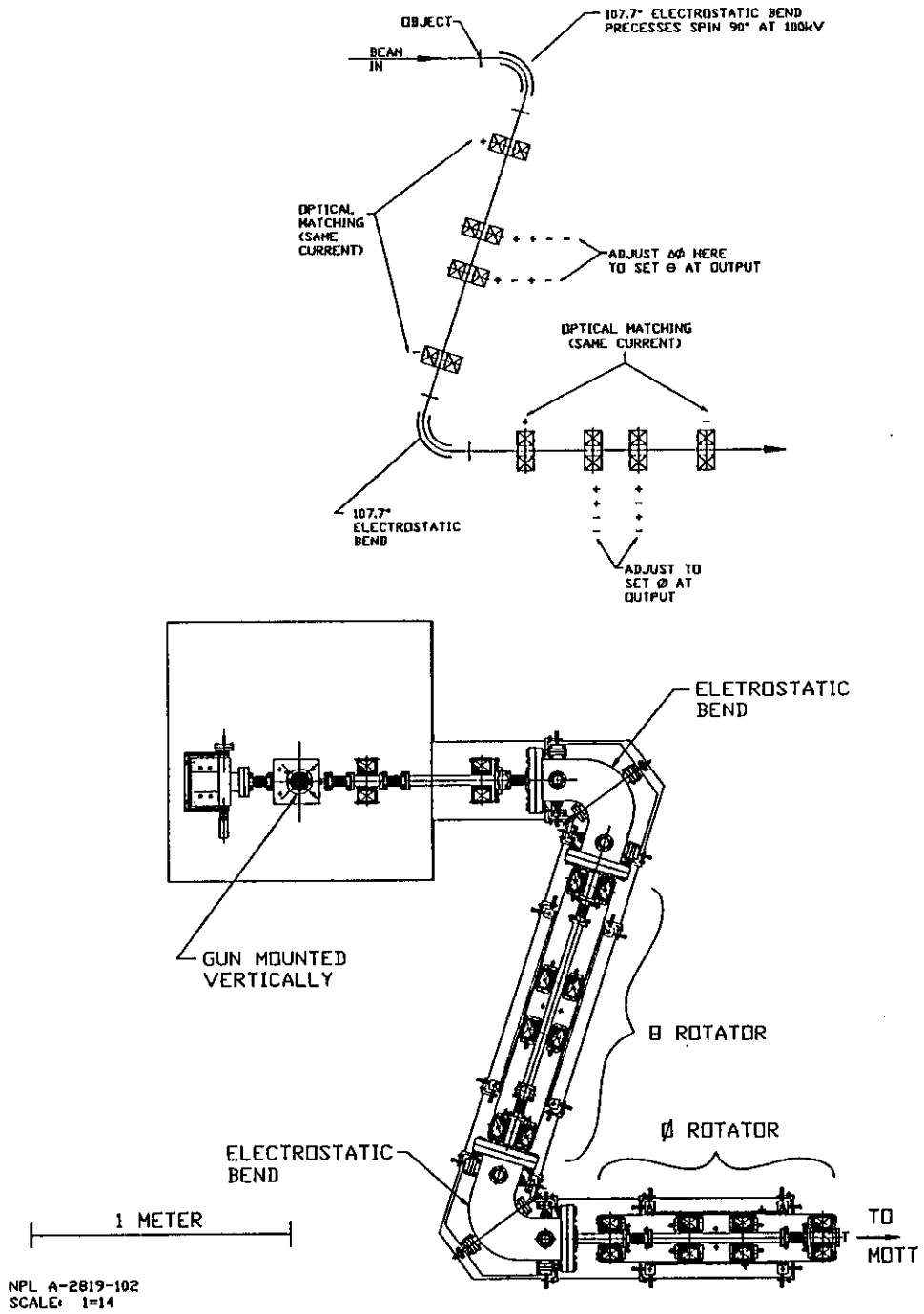

Figure 35: A schematic representation of the operation of the Illinois/CEBAF spin manipulator (top); and the mechanical realization of the spin manipulator showing the major components (bottom).

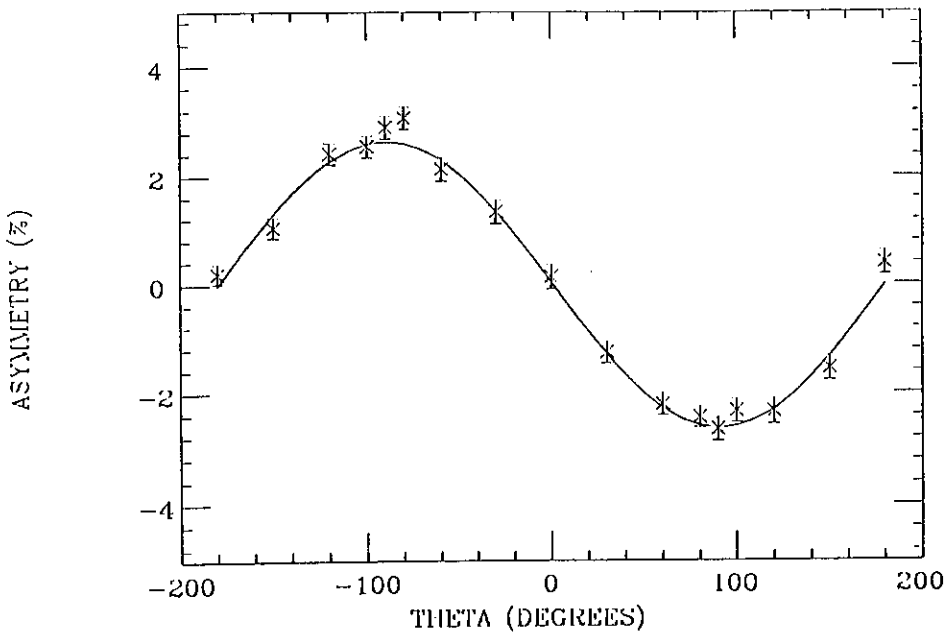

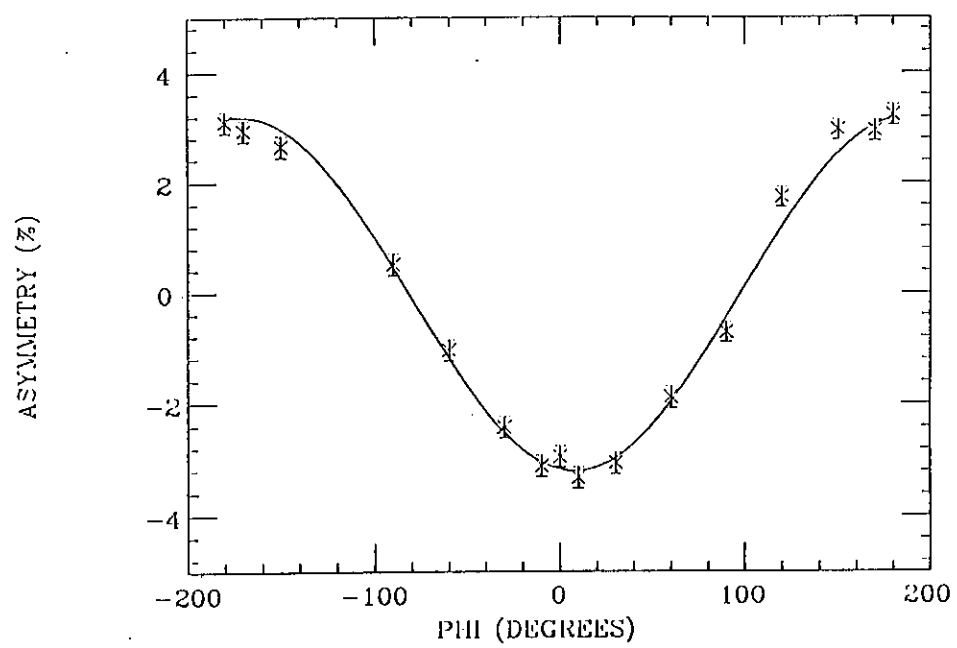

Figure 36: Operation of the Illinois/CEBAF spin manipulator. The upper curve shows rotation of the polar angle, θ for a fixed azimuthal angle $\phi = 90°$; the lower curve shows rotation of the azimuthal angle ϕ for a fixed polar angle $\theta = 90°$. In both cases, the asymmetry measured using the Mott polarimeter (which is proportional to the projection of the polarization in the vertical direction) is plotted as a function of the calculated rotation angle.

i. the development of the ancillary equipment needed for both rapid and slow flipping of the spin under computer control;

ii. a "flexible pulse structure" laser drive permitting the operation of the source at lower duty factor but with higher peak current (maintaining a constant average current);

iii. (possibly) rf chopping in the laser drive; and

iv. the construction of a second (duplicate) polarized electron gun for high reliability.

Rapid, computer-controlled flipping of the polarization vector is essential for experiments such as the G_E^0 measurement where the experimental asymmetries are extremely small and a variety of techniques must be employed to eliminate systematic error. The technology for implementing spin flipping will follow the ideas first developed at SLAC; it is straightforward and well–understood. Spin-flipping is most easily accomplished in the laser "drive" for the photocathode, as the beam helicity flips when the laser beam's helicity is switched. The helicity reversal for the Illinois/CEBAF source will include both an electrically- reversible "$\pm$ quarter-wave plate" based on a Pockels cell, and a mechanically-insertable half-wave plate (providing "slow" helicity reversal by changing the electrical sense of the operation of the Pockels cell). A third, independent method for reversing the spin vector is available via the spin manipulator discussed above, which will operate on the electron beam rather than on the laser drive.

In order to provide the 32 ns time structure needed for the G_E^0 measurement, we are planning the development of a "flexible pulse structure" drive system for the polarized source. This system will permit a trade–off between peak current and duty factor over a range of as much as two orders of magnitude. It will be possible, for example, to provide a cw beam of 40 μA average current with a 100% duty factor and a peak current (before bunching) of 0.24 mA; alternately, the same average beam current could be provided with a 1% duty factor and a peak current of 24 mA. The beam we want for the G_E^0 measurement is effectively a 6.25% duty factor (one pulse in 16) corresponding to a peak current of 3.84 mA (before bunching). The flexible pulse drive system that will be constructed for the G_E^0 experiment will also be useful for a variety of other experiments, such as those involving neutron energy measurement or particle identification by time of flight, where a controlled time structure in the beam is crucial. Studies of the gun itself indicate that a full two orders of magnitude variation in the duty factor will be feasible. It is clear that the factor of sixteen required for the G_E^0 experiment will be possible, but detailed calculations of the beam transport through the injector will be required before the minimum duty factor can be established. A duty factor of order 1% is a lower bound, as heating of the higher-order mode loads in the CEBAF linacs begins to be a problem at this level of charge per bunch.

The addition of chopping in the laser drive is of potential interest in that it will reduce the total charge drawn from the gun per unit time by a factor of six. The expected benefits include: a significantly improved lifetime for the source; the elimination of the emittance growth that can occur in conventional rf–cavity chopping systems; and a reduction of the

photocathode quantum efficiency required for full beam current.

A likely approach to the drive system would incorporate a mode-locked laser operating at a sub-harmonic of the CEBAF rf frequency and multiplied to the frequency of interest. We will probably incorporate chopping of the beam in the laser drive followed by bunching using conventional, single accelerating cavity techniques. It is not clear at this time whether the polarized source will require its own bunching cavity or merge with the CEBAF thermionic injector line upstream of the buncher on that line. A detailed design of the integration of the polarized source into the injection line will take place next year in collaboration with CEBAF staff. Among the issues to be addressed are the need to improve the shielding in the injector area so that it will be possible to work on the polarized source while the accelerator is running.

Finally, in order to obtain the highest possible reliability and availability for the polarized source we have begun constructing a second (duplicate) polarized electron gun. This source will initially be used for lifetime studies and the development of operations procedures at CEBAF. Eventually it will be installed (at CEBAF) in tandem with the source that is already working at Illinois. With two sources it is straightforward to switch between them when it is necessary to refurbish the cathode (which takes about 24 hours) or to make other repairs on the source. So long as the lifetime of the cathode is greater than the refurbishing time, the source (pair) can be operational essentially 100% of the time.

The work described above is already in progress at Illinois with funding from both NSF and CEBAF. Therefore we do not include the associated costs in the budget presented for the G_E^0 experiment proposed here.

The outlook for polarizations larger than 50%

Typical operating GaAs-type polarized electron sources have achieved polarizations between 25 and 43%. This relatively low polarization has been an important limitation in their use. As a consequence, a great deal of research has been carried out over the last decade aimed both toward understanding why working GaAs sources have a polarization less than the theoretical maximum of 50%, and toward "breaking" the 50% barrier.

Recent experiments [Al81,Ma89] indicate that the loss of polarization in GaAs is due to spin dilution as the electrons diffuse to the semiconductor surface; the absorption depth for 1.4 eV photons in GaAs is about 1 μm. The experiments of Maruyama *et al.* [Ma89] used custom-grown crystals; a thin layer of GaAs was grown by MBE on a 0.9 μm thick layer of $GaAl_{0.3}As_{0.7}$ which had been grown on a GaAs substrate. The $GaAl_{0.3}As_{0.7}$ layer isolates the thin GaAs sample from the substrate by providing a potential barrier (due to the higher bandgap in this material) that keeps electrons from deep within the crystal from reaching the surface. A thin Sb "cap" was added to protect the sample during handling. In the experiments of Maruyama *et al.*, a sample thickness of 0.2 μm gave a polarization

of 49%, close to the theoretical maximum, while the polarization obtainable from a 0.9 μm thick sample was indistinguishable from that obtainable from bulk GaAs. The quantum efficiency of the 0.2 μm sample was 1.8%, more than adequate for full beam intensity at CEBAF. This approach to "thin" cathode fabrication provides a practical solution to the problem of the installation of thin cathodes in a working accelerator source. Cathodes of this type have been obtained from two independent sources; they yielded essentially identical results.

Of course even the thinnest conceivable sample of GaAs would not have a polarization greater than 50%, so further increases in polarization require a different approach that somehow removes the degeneracy in GaAs. Among the possibilities that have been discussed [Si76,Si89,Re90] are: the application of uniaxial stress to the crystal; the construction of artificial structures with the bandgap energy varying in the direction perpendicular to the emitting surface; and the use of direct bandgap materials other than GaAs in which the degeneracy is absent due to the lack of symmetry in the crystal structure. In the past year we have seen major breakthroughs in each of these areas.

Strained photocathodes The application of uniaxial strain to a crystal of GaAs removes the band degeneracy by breaking the symmetry of the crystalline structure. Calculations [Zo82,Na90] of this effect indicate that high polarizations can be achieved, but the strain required is of order 6×10^9 dynes/cm^2. The generation of strain of this magnitude in the laboratory by conventional mechanical means is far from trivial, and the crystal is more likely to break than serve as a useful photocathode. Instead, experimenters have generated the necessary strain by growing the photocathode material on a substrate having a different lattice constant. Maruyama *et al.* [Ma91] were the first to demonstrate a photocathode that provides polarization in excess of 50%. They used a 0.1 μm crystal of $In_xGa_{1-x}As$ (with $x \simeq 0.13$) grown on a substrate of GaAs; in this case the lattice constants differ by 0.9%. This cathode provided a polarization of 70% at λ=940 nm with a quantum efficiency of $\sim 7 \times 10^{-5}$.

More recently, 86% polarization with a quantum efficiency of $\sim 2 \times 10^{-4}$ at a wavelength of 860 nm was achieved by Nakanishi *et al.* [Na91a] using a 0.08 μm thick GaAs layer grown on GaP_xAs_{1-x} (with x=0.17) (see Figure 37). The shorter wavelength is a better match for existing high-power lasers. For their crystal the lattice mismatch was estimated to be $\sim$ 0.6%. A second attempt by Nakanishi *et al.* [Napc] resulted in an 83% polarization with a 0.1% quantum efficiency. This cathode has the highest figure of merit available for the G_E^0 experiment, and we will attempt to reproduce the Nagoya results in the near future.

Terechov [Tepc] has suggested an alternate approach to straining GaAs: diffusion welding a thin crystal at an elevated temperature to a glass substrate with a different thermal expansion coefficient. The potential advantage of this approach lies in the fact that the crystal can be grown in its relaxed state, so its structure and surface should be closer to the ideal. Efforts to fabricate cathodes of this type are underway at Novosibirsk,

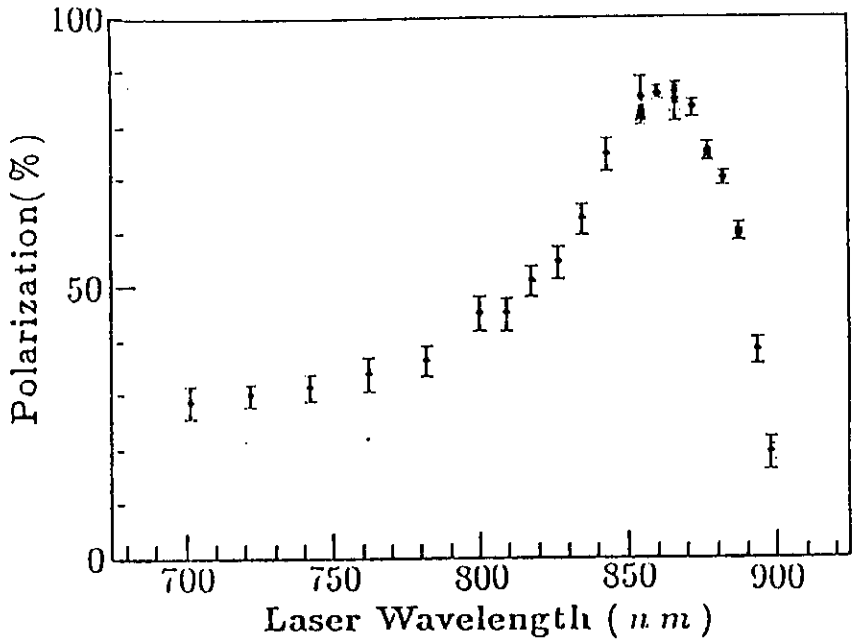

Figure 37: Polarization vs photon energy for electrons from a strained GaAs photocathode grown on GaP_xAs_{1-x} [Na91a].

and their polarization will be investigated at Illinois.

Multi-layer heterostructure cathodes Multi-layer heterostructures, such as alternating GaAs and $GaAl_xAs_{1-x}$, provide a second avenue to high polarization. The KEK/-Nagoya/NEC group has demonstrated [Om90] a polarization of 71.2% at $\lambda = 802$ nm from a 0.1 μm thick superlattice consisting of alternating layers of GaAs (19.8 Å thick) and $GaAl_xAs_{1-x}$ (31.1 Å thick) grown on a GaAs substrate. The layer dimensions were chosen by balancing the conflicting requirements of wanting the energy splitting to be as large as possible (implying deep, well-spaced, potential wells) and wanting good transmission of electrons between the wells (implying shallow wells) so that the polarized electrons can be extracted.

Alternate photocathode materials Both strained crystals and superlattices are capable of providing highly polarized beam at the modest beam currents needed for polarized target applications, but improved quantum efficiency will be necessary before these cathodes can realize their full potential. In both cases improved quantum efficiency will require a delicate balance of conflicting requirements. For example, when the thickness of the strained $In_xGa_{1-x}As$ crystal was increased [Ma91] to 1.14 μm the quantum efficiency rose to over 1×10^{-4}, but the maximum polarization was reduced to about 50% because the crystal "relaxed" over that thickness. Similarly, for the superlattices there is a delicate balance between polarization and quantum efficiency; an earlier crystal with the same well dimensions but a 0.4 μm thickness gave only 52.5% polarization. [Ku90a] In this case it is depolarization effects at the well boundaries that are thought to be most important. [Na90] Experiments to investigate these tradeoffs in both strained and superlattice samples are

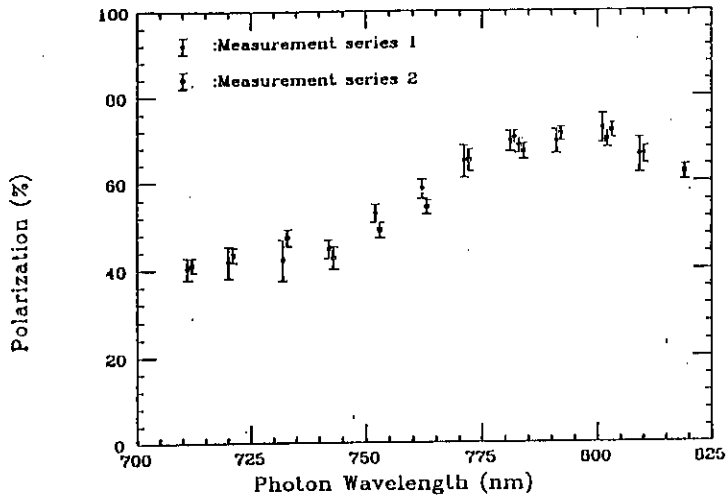

Figure 38: Polarization vs wavelength for electrons from a GaAs-GaAlAs superlattice photocathode [Om90].

underway, but it is not likely that quantum efficiencies much higher than a few times 10^{-3} will be simple to obtain.

A third approach to higher polarization in photocathode sources is the use of other direct-bandgap materials that naturally lack the valence band degeneracy of GaAs, such as the II–IV–V_2 chalcopyrites. In these ternary analogues of the III–V compounds (such as GaAs) the valence band degeneracy has been removed by the fact that there are two cations instead of one and, in most cases, significant tetragonal distortion. These materials have the promise of providing both high polarization and high quantum efficiency with more straightforward tradeoffs than is the case for strained or superlattice crystals.

Efforts [Si89,Re90] to make cathodes using chalcopyrite materials have been hampered by the poor quality of the crystals available, and by the low band gaps of some of the materials used. The RTI group [So89] has grown excellent quality epitaxial samples of $ZnGeAs_2$ using the MOCVD technique. They have also succeeded in growing alloys of $ZnGeAs_2$ with phosphorous [$ZnGe(As_{0.9}P_{0.1})_2$] and with silicon [$Zn(Ge_{0.7}Si_{0.3})As_2$]. These materials have significantly higher bandgaps than the 1.15 eV of $ZnGeAs_2$, and the Illinois/CEBAF group has successfully fabricated NEA photocathodes on $Zn(Ge_{0.7}Si_{0.3})As_2$. The emitted electron polarization from a similar chalcopyrite, $CdSiAs_2$, was measured by the ETH Zürich group. [Me90] The polarization underwent the expected transitions as a function of wavelength, but the magnitude of the polarization was only about 15%. This measurement probably suffered from poor crystal quality and from the crude surface treatment employed, and we can look forward to advances in this approach as well.

Operational implications of photocathode polarization results to date The figures of merit, P^2I, obtainable from the photocathode sources discussed above under the beam conditions appropriate to the G_E^0 experiment (40μA average beam current) are listed in Table 8. The current, I, available from a photocathode source is given by:

Table 8: Figures of merit for different polarized electron source photocathodes

Source/Cathode	Ref.	P(%)	QE	$\langle I(\mu A)\rangle^a_{max}$	$P^2I(\mu A)$ Laser Chopping[b]	$P^2I(\mu A)$ DC Operation[b,c]
Bulk GaAs (typical)	[Si89,Re90]	40	5×10^{-2}	4,938	6.4	6.4
"Thin" GaAs	[Ma89]	49	1.8×10^{-2}	1,778	9.6	9.6
GaAs on GaP_xAs_{1-x}	[Na91a]	86	2×10^{-4}	22	16.1	2.7
GaAs on GaP_xAs_{1-x}	[Napc]	83	1×10^{-3}	109	27.6	12.5
Superlattice	[Om90]	71	2×10^{-4}	20	9.9	1.7
$In_xGa_{1-x}As$ on GaAs	[Ma91]	71	7×10^{-5}	8	4.2	0.7

[a] Limited by maximum average laser power consistent with no "burning" (see text).
[b] Average current limited to 40μA (or less if limited by QE).
[c] $\langle I\rangle_{max}$ reduced by a factor of 6 to account for chopping losses.

$$I(\mu A) = \frac{QE(\%)\cdot P(mW)\cdot \lambda(nm)}{124}$$

where P = the laser power,
λ = the laser wavelength, and
QE = the quantum efficiency of the photocathode.

This formula yields the well-known result of 6.5 mA of beam current for a 1% quantum efficiency cathode and 1 Watt of laser power at a wavelength of 805 nm. For low duty factor accelerators, the available laser power (coupled with the few percent quantum efficiencies that are routinely achievable) typically defines the operational limit. The situation at CEBAF is different. To provide a 40μA (average) beam current with the 32 ns period proposed for the G^0_E experiment, the peak beam current required from the cathode is only 3 mA; for a 1% quantum efficiency cathode this can be achieved with 500 mW of (peak) laser power, and only about 6 mW of average laser power. The limitation instead is due to the phenomenon of "burning," in which local average power densities above a critical limit damage the crystal surface, destroying its quantum efficiency. Our understanding of this phenomenon is sketchy at best [Si89], and experiments place the average power density limit between 5 and 20 Watts/cm^2. Since the laser spot size is limited to ~1 mm diameter at CEBAF (to obtain optimum beam emittance), a 20 Watt/cm^2 power limit implies that the average laser power available is only 157 mW.

Applying this power limit to the different photocathodes available (and operating each at the wavelength appropriate for maximum polarization) yields the maximum currents in the 5th column of Table 8. Considering a (target-limited) maximum beam current of 40μA yields the results in the last two columns of the table; for the column labeled "dc operation" we have reduced the maximum currents available by a factor of six to account for chopping and bunching losses (assuming these operations are done external to the source using the

same techniques now used on CEBAF's thermionic gun. For the column labeled "laser chopping" we assume that this factor of six loss can be avoided by doing the chopping in the laser drive. As can be seen from the table, the strained GaAs on GaP_xAs_{1-x} cathodes developed at Nagoya have the promise of improving the figure of merit by as much as a factor of three over "thin" GaAs. However, we have chosen to use the more conservative figure of merit associated with the "thin" GaAs cathodes until it is clear that the strained samples are easily reproducible and operationally reliable. In the event that this turns out to be the case, the beam time required to carry out G_E^0 the experiment will be reduced significantly. The "production" beam time scales inversely with the figure of merit. The gain will not be as large for the test measurements required, but can nonetheless be expected to be significant.

4.4.2 Beam and spin transport, and beam polarization measurement

Beam transport through CEBAF

In order to use the correlation between momentum and flight time for data acquisition, we are planning to employ a beam microstructure with 32 ns between bunches as opposed to the normal 2 ns (per experimental hall). In order to keep the average beam current constant, the number of electrons per bunch must therefore be increased by a factor of 16 over "normal" operation. J. Bisognano *et al.* have studied [Bi91] the implications of this kind of beam time structure in conjunction with plans for an FEL at CEBAF. The FEL under consideration [Ne91] requires bunches of 120 pC at repetition rates of 2.5 and 7.5 MHz (the "normal," full-intensity, 200μA CEBAF beam has ~0.13 pC bunches at a repetition rate of 1500 MHz). They found that operating beams for the FEL simultaneously with the "normal" beams for nuclear physics operation influenced the nuclear physics beams at a level that was below all relevant design parameters. The 32 ns period, 40μA average current beam we propose implies operation with ~1.28 pC bunches at a frequency of 31.25 MHz. Since the FEL beam represents a much greater perturbation on the CEBAF linac, it is safe to presume that the beam planned for the G_E^0 experiment can operate interlaced with "normal" nuclear physics beams to the other end stations with no ill effects on any of the beams.

We plan to group the 32 ns micropulses into 30 Hz macropulses for purposes of noise reduction. Since the electronics is designed to be fully- buffered, so that data from one helicity state can be read out during the $1/30^{th}$ of a second associated with the next measurement interval, it will not be necessary to impose "dead periods" on the beam structure ("dead periods" on this time scale might perturb the energies of the other beams in the linac). **Therefore, it would appear that this experiment can be run concurrently with other nuclear physics experiments in other halls.**

Since this experiment requires a relatively high current on a cryogenic target, it will be necessary to "raster" the beam across the surface to avoid excessive heating. Experi-

ence with the SLAC hydrogen targets suggests that the beam be spread over an area of ≈ 0.2 cm^2. Devices to effect the necessary motion are under design at CEBAF for use in a variety of target applications, and we anticipate using them in this experiment. For the G_E^0 experiment it will be necessary to synchronize the rastering frequency with the helicity reversal rate to prevent unintended false asymmetries. Since the rastering will be done at audio frequencies, this synchronization will be straightforward.

Spin transport through CEBAF

We have chosen a beam energy of 2.5 GeV by considering the sensitivity of the experiment to both G_E^0 and background processes. At this beam energy, the longitudinal component of the electron spin will precess through 4.3 revolutions for five-pass acceleration, not including the effect of the beam switchyard magnets. Consequently, the spin must be oriented at the source so that it is pointed in the correct direction to obtain longitudinal polarization at the target. The necessary spin orientation apparatus has been constructed at the University of Illinois, and is described in Section 4.4.1 above.

In principle, focussing elements such as quadrupoles or solenoids will cause the spin of the individual electrons in the beam to precess by different amounts depending on their initial coordinates within the electron beam's phase volume. This effect could depolarize the beam completely as it completes its trip through the accelerator. However, rough calculations indicate that the very small beam emittance at CEBAF will keep the depolarization negligibly small. In the injection region, where the electron energy differences are largest, the focussing solenoids will all be installed so that the net field integral is zero. Another important feature of CEBAF is that there is no acceleration of the beam in regions having magnetic fields. These rough calculations will be checked by detailed calculations in the near future. J. Kewisch of CEBAF has agreed to supervise Mr. C. McDowell, a student at Caltech, who will carry out the calculations.

Beam polarization measurement in Hall C

The electron beam polarization, P_B, enters proportionally into the experimental asymmetry. The goal for the beam polarization measurement (at 2.5 GeV) is 2% for this experiment. We choose to do this with Møller scattering from a polarized ferromagnetic foil. The technique is relatively inexpensive and technically uncomplicated, and should be able to deliver the necessary precision. Møller scattering has been used to measure beam polarization by many groups over a wide range of incident energies [Ar91,Wa90,Co75]. Since the Møller scattering rate is quite large, the precision of the technique is limited mainly by systematic error.

The technique is described in detail in [Ar91,Wa90]. Briefly, one determines the (longitudinal) beam polarization by detecting Møller scattering with some sort of spectrometer

arrangement, and measuring an asymmetry A_{MEAS} as the beam helicity is flipped. We then have

$$P_B = \frac{A_{MEAS}}{P_T\ a_{zz}}\left(1 + \frac{B}{S}\right)$$

where P_T is the polarization of the target electrons, a_{zz} is the calculated analyzing power, and B/S is the ratio of background to signal. (An analogous relation allows one to measure transverse polarization components as well [Wa90].) Longitudinal and transverse analyzing powers are maximized for scattering at $\theta_{CM} = 90°$, so Møller spectrometers are designed to work at those kinematics. The scattered electrons each have half the beam energy E_0, and the laboratory scattering angle is $\theta_{LAB} = \tan^{-1}([2m/(E_0 + m)]^{1/2})$, where m is the electron mass. At $E_0 = 2.5\ GeV$, $\theta_{LAB} = 1.16°$. One finds $A_{MEAS} \approx 0.5\%$ so we aim to measure the asymmetry with a precision on the order of 10^{-4}.

The target foil is made from some high permeability material, typically Supermendur, an alloy of Fe(49%), Co(49%), and V(2%). It is completely saturated with an applied field between 50 and 100 Gauss. The field is generated by a pair of current-carrying coils surrounding the target. As the electrons in the foil are polarized only in the direction of the plane of the foil, it is necessary to tilt the target at some angle to the normal to the beam so that an appreciable fraction of the foil polarization is longitudinal. That is, $P_T = P_{FOIL} \times \sin(\theta_{TILT})$. The foil polarization is measured by determining its magnetization using induction techniques, and multiplying by the thickness of the foil. A $7 \pm 1\%$ correction must be made to account for the orbital contribution to the magnetization.

The limiting systematic errors arise from a number of sources [Ar91]. The cumulative uncertainty from the target thickness, foil polarization, tilt angle, and helicity-correlated beam motion is $2 - 3\%$. The dominant source of systematic error, however, is due to the uncertainty in B/S and how sensitive it is to the other systematic errors. Typical values of $B/S \approx 1$ have limited the precision in P_B to $\approx 5\%$. Background arises from the need to detect electrons with half the beam energy at very small angles where shielding is difficult, as well as some contribution from the Mott scattering radiative tail.

For beam energies between around 200 and 800 MeV, a simple quadrupole spectrometer has been used to detect Møller scattering [Ar91,Wa90]. That is, the target is located some distance upstream of the quadrupole magnet, and Møller scattered electrons are detected downstream in the defocussing plane. Incident trajectories are defined with a collimator system that allows both the incident beam and electrons scattered at $\theta_{CM} = 90°$ to pass into the magnet. With sufficient shielding, this technique can detect Møller scattering in singles with $B/S \approx 1$. However, the Mainz group [Wa90] has demonstrated that if both electrons are detected in coincidence, the background is eliminated. This is particularly elegant kinematics, at $\theta_{CM} = 90°$, since the detection scheme is symmetric for both electrons. Coincidence detection is only possible, however, for CW operation (or extremely low beam currents) since the Møller and background rates are quite high. We expect to use this technique for our measurement, since it is well suited to the CEBAF beam. Therefore, we will ultimately measure P_B to $\pm 2\%$ or so, limited by the systematics in foil polarization and tilt angle. Measurements of the transverse beam polarization will

also be possible [Wa90].

Figure 39 shows the beam line and tunnel leading to Hall C from the beam switchyard. A length of ≈15 m has been reserved for a beam polarimeter, downstream of the bending magnets which will precess the spin as it leaves the switchyard. CEBAF has available several surplus 10Q36 quadrupole magnets, any one of which is quite suitable for this task. An elevation view of the tunnel cross section, including the position of the beam line and the magnet, is also shown in Figure 39.

The length of the Møller spectrometer is determined by the choice of optics. There are essentially two options for Møller optics using the available quadrupole magnet. One is to optimize the design for our experiment beam energy, namely 2.5 GeV. This is done by setting the magnet to its maximum gradient (9.8 tesla/m) and adjusting the target position so that the Møller scattered electrons emerge from the magnet just inside the bore radius (12.5 cm). This gives the maximum deflection angle possible, which is best for shielding considerations. A drift space is added which would put the detectors at around 80 cm transverse to the beam axis, allowing sufficient space within the tunnel wall. (See Figure 39.) The optics are shown in the top of Figure 40.

It would of course be desirable to build a system that works over the possible range of incident energies, assuming other experiments are approved that will use polarized beam in Hall C. An alternative design has been worked out [Ch91] which allows one to detect Møller scattering for incident energies between 1 and 4 GeV. There are two potential drawbacks. One is that the target position must be located at one of three different locations, depending on the incident energy, leading to increased complexity and cost. The second, and potentially more serious, disadvantage is that the bend angle and transverse distance from the beam are somewhat smaller than in the system dedicated to 2.5 GeV. The optics are shown in the bottom of Figure 40. Backgrounds must be evaluated before a decision is made, again assuming there are other relevant experiments. In any case, no matter what choice of optics is made, the total length of the system is under 8 m and will easily fit in the allotted space.

Our experiment will run with 40μA average current, pulsed at 31.25 MHz. Using the Møller scattering cross section of 0.18 b/sr [Ar91], and assuming a $\frac{1}{2}$ mil Fe foil tilted at 60° and a 6 mm diameter collimator 2 m downstream of the target, we find a Møller scattering rate of 0.03/pulse or 1 MHz average. However, target heating effects may require that we use smaller average current, which we can easily achieve by decrease the beam pulse rate. In addition, the accidental pile-up rate may be too large, depending on backgrounds, so the instantaneous current may also need to be reduced to get systematic errors from dead time reduced below 1%. This is also easy to achieve simply by reducing the laser power at the polarized electron source.

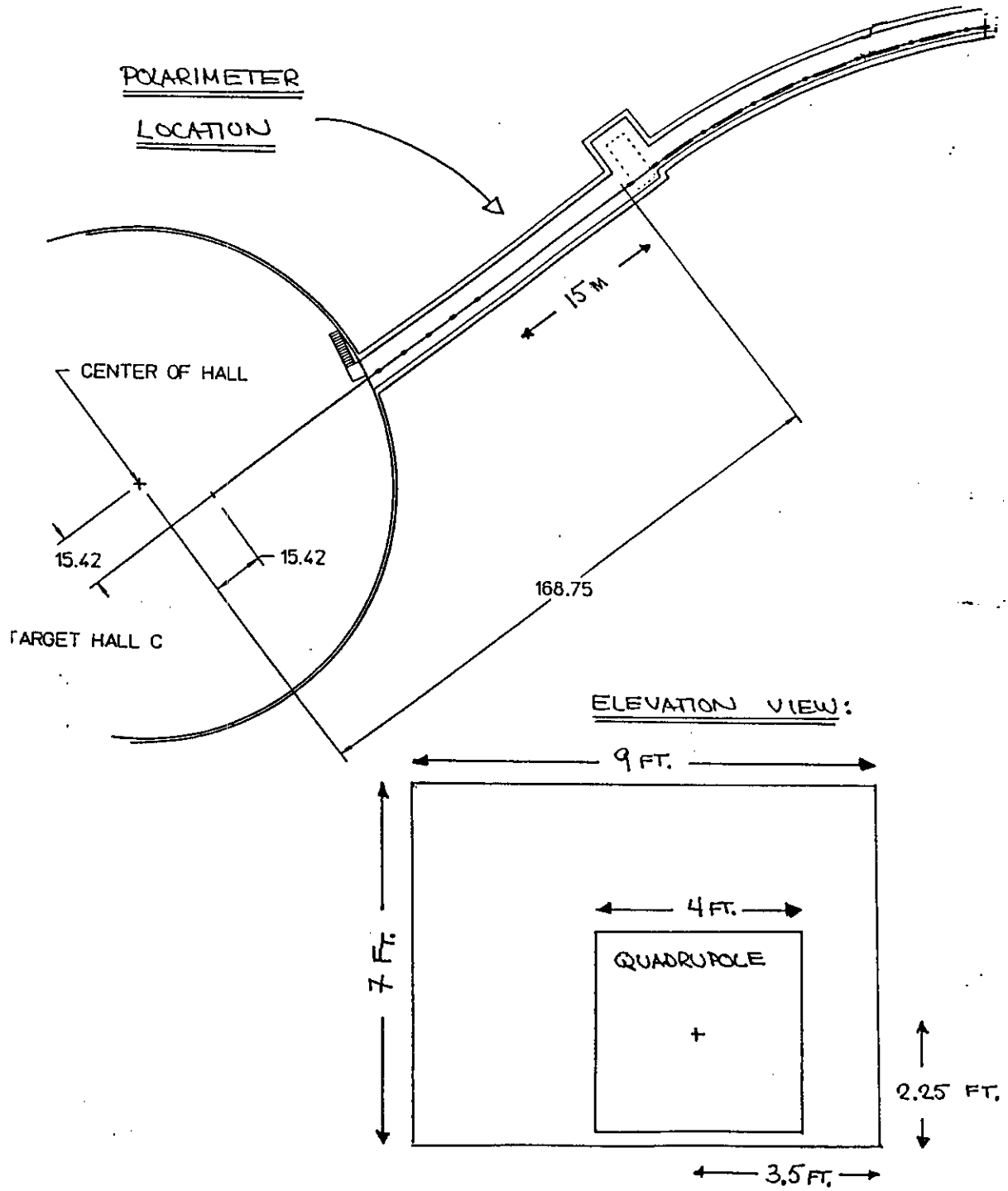

Figure 39: Location of the Møller polarimeter in the beam tunnel leading to Hall C. There is a clear area, reserved for this purpose, downstream of the bending magnets. The inset shows how the available 10Q36 quadrupole fits around the beamline inside the tunnel.

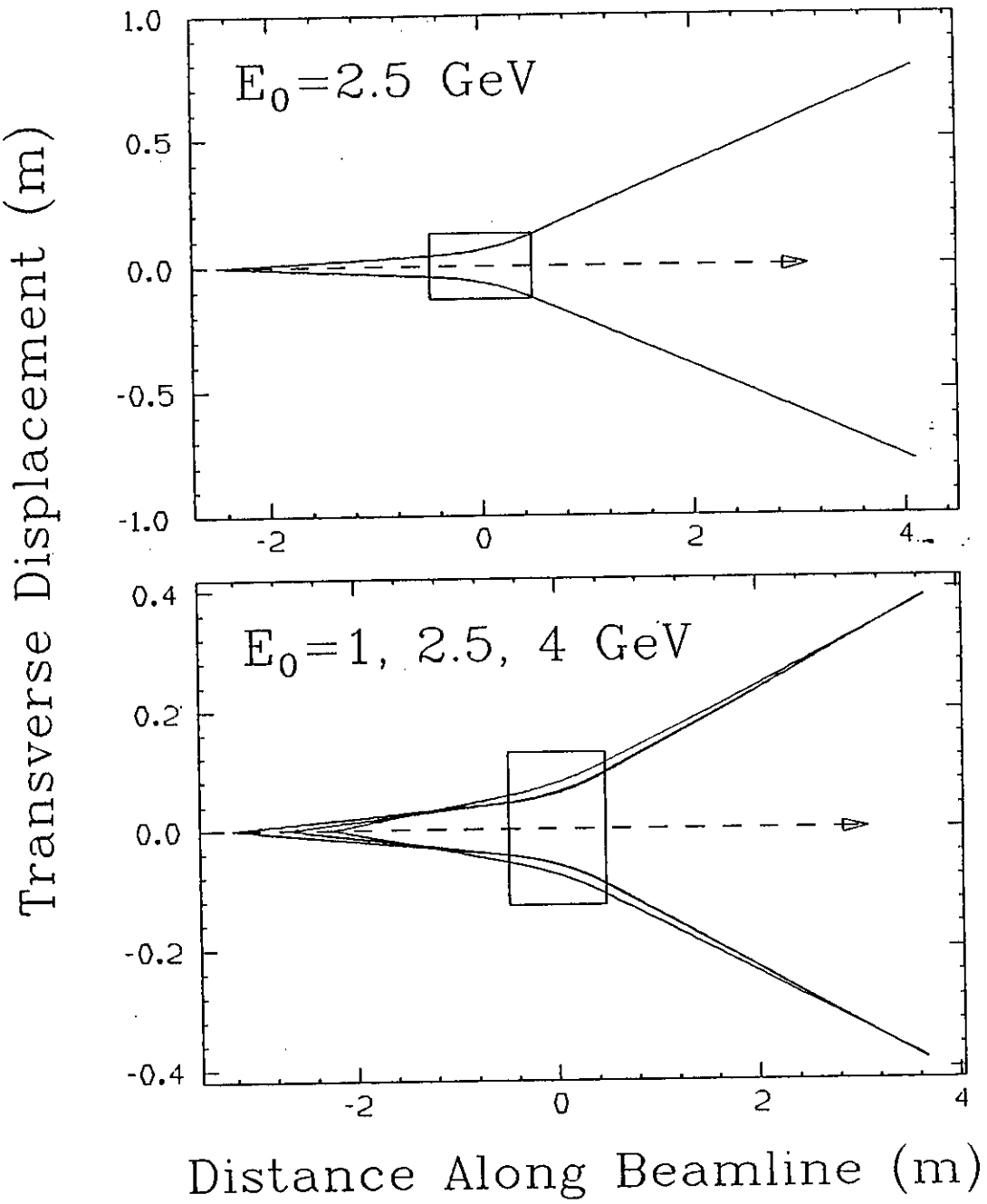

Figure 40: Two options for optics for the Møller spectrometer. The top option shows a design optimized for the nominal beam energy for our experiment, namely 2.5 GeV. The bottom option shows a design [Ch91] that allows all beam energies between 1 and 4 GeV, at the expense of a smaller deflection angle and some mechanical complexity. Note that the vertical and horizontal scales are not the same in either figure; the box represents the same 10" bore, 36" long magnet.

4.4.3 Beam current and position monitoring

After each 30 Hz macropulse, we want to read out information that characterizes the beam conditions during that pulse. These include, for example, the total charge Q in the pulse, and x and y positions at various points along the beamline so that we can infer the beam position and angle at the target, and the excursion, δ, of the average energy during the macropulse from the nominal central energy of the beam. In addition we may also want to read a beam profile monitor that gives information on the beam shape.

As discussed in Section 3.4.6 (see Table 4), we need to know the beam energy with a relative precision of $\approx 1 \times 10^{-5}$, the beam position to ≈ 25 μm, and the beam angle to $\approx$0.01 mr per macropulse. A location in the middle of the Hall C transport line has been identified as an appropriate location for beam energy measurement; the beam has a dispersion of 2.1 cm/%, so that a $\approx 1 \times 10^{-5}$ measurement of the energy corresponds to a position measurement of 21 μm, providing a good match between the precision required for the position and energy measurements. Provision must also be made in the beam transport and control systems for changing these quantities throughout the experiment, implying that experimental control of all beam switchyard steering must also be implemented.

Work is just beginning to design the necessary beam monitoring devices. The problem is a challenging one. W. Barry, who was involved in the development of much of the beam monitoring equipment on the accelerator at CEBAF, has agreed to undertake this task.

5 Budget

The proposed budget for the G_E^0 spectrometer and its associated equipment is presented in Table 9. EDIA costs equal to 25% of the basic estimated equipment costs are included for all equipment items, and an additional 25% is added in to account for contingencies. The total cost is estimated to be \$5,639 K. (We anticipate that the cousts might be shared by NSF and DOE on roughly a 2:1 basis).

There are several important qualifying remarks to be made. First, we have made use existing equipment where possible. The costs for the target and polarimeter included in the budget assume the existing equipment will be used. We are also looking into the possibility of providing the magnet power supply, water cooling tower and room shielding at reduced cost; however, at this point the costs in the budget are the full (new) costs. Second, we have not tried to estimate the costs associated with beam control and diagnostic apparatus other than the polarimeter. Last, we note that although the G_E^0 spectrometer must be designed and constructed with care, it is the online measurements that will provide the precision required for the experiment (for example, the measurement of relative sector efficiencies). The instrument is not technologically complex; we fully expect that with reasonable attention it will be constructed within the cost envelope given in Table 9.

Table 9: G_E^0 experiment equipment budget

Item	Cost(in 1991$k)	
Spectrometer:		
Coils	1100	
Power Supply	400	
Cooling Tower	250	
Support	620	
Slotted Beam Pipe	30	
Installation & Support Systems	400	
Subtotal		2,800
Alignment: Fixtures & Control		50
Detector Components and Electronics:		
Scintillator	14	
Phototubes	26	
Bases, shields	34	
Power supply	31	
Mean-timers	21	
CFD's	41	
Scalers	67	
Electronics Bins	20	
Cables, Racks	10	
Subtotal		224
Detector Support and Shielding:		
Support	75	
Scintillator Shielding	30	
Room Shielding	200	
Subtotal		305
Detector Monitoring: Laser Calibration		30
Target: SAMPLE Target Modifications		150
Data Acquisition:		
DECStation 3100/76	10	
Exabyte Tape Drive	5	
DAQ Modules	35	
Subtotal		50
Beam Monitoring: Polarimeter		30
EQUIPMENT COST		3,639
EDIA (25%)		910
SUBTOTAL		4,549
CONTINGENCY (25%)		1,137
TOTAL		5,686

Notes: Substantial costs are saved by using existing equipment.
Costs of beam monitoring and control equipment are not included.

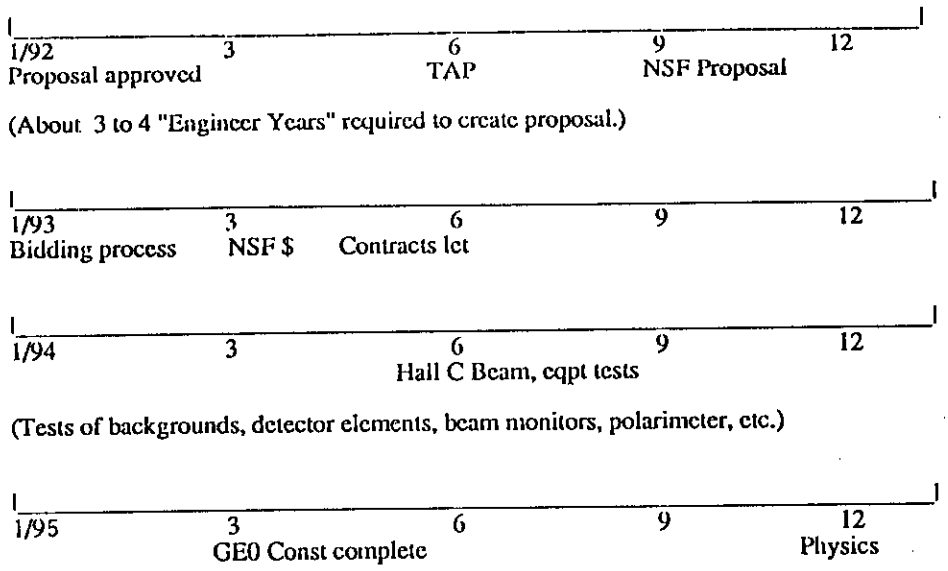

Figure 41: The schedule for the G_E^0 experiment.

6 Construction schedule

A possible schedule for design completion, proposal submission, bidding, construction, and installation is shown in Figure 41. It assumes that the physics proposal has been approved by January 1, 1992, and that the design is far enough along for a Fall submission of a proposal to NSF for a special equipment grant to cover the cost of the spectrometer. This implies that a TAP meeting should be scheduled for around June 1, 1992 to gain final approval of the instrument's design.

This suggests that the optimal time to go out for bids on the spectrometer coils and support is in the early part of 1993. Bringing the design to the point where bidding can be done then will require a large input of engineering resources (roughly 3 person-years) during CY92. A significant fraction of the funds to support this ($130 K) will come from the existing Illinois grant, but additional funds will be needed. We are in the midst of discussions with the NSF to see if it is possible to obtain these funds.

From the point of view of construction, funding for the device would spread nicely over the two-year period from March 1, 1993 to March 1, 1995, at which point the construction would be finished and the device ready for installation in Hall C. We note that all pieces of the spectrometer and supports will be small enough to be installed with the Hall C crane. With beam expected in Hall C in the Summer of 1994, we would use the time between turn-on and installation of the spectrometer to develop and test the necessary beam monitors and dump, the background rates and shielding, the polarimetry, and other things.

7 Institutional responsibilities

The collaboration brings much experience in both electron scattering and parity-violation experiments, in the instrumentation necessary for the experiment, and in knowledge of the CEBAF accelerator properties. Arizona State is undertaking the GEANT and TOSCA simulations. The Caltech group will be responsible for the target. The Carnegie Mellon collaborators will provide the data acquisition electronics and computers. CEBAF takes responsibility for accelerator and beamline instrumentation. The spectrometer will be designed and constructed by the University of Illinois group. Illinois will also provide the polarized electron source for the accelerator. We are discussing the construction of the detectors and polarimeter with another potential collaborator at this time; if they are unable to join our effort, Illinois will construct the detectors and CEBAF will construct the beam polarimeter. MIT and UMass have agreed to provide theoretical support for the experiment, particularly with the thorny issues associated with the radiative corrections.

8 Beam time request

We request a total of 1500 h to measure the flavor singlet charge form factor of the proton. The counting time required to achieve a statistical precision of 5% of the nominal asymmetry, $A^{nom} = -5 \times 10^{-6}$, is 400 h assuming a beam polarization of 49%. The remaining beam time is required for a series of tests to ensure that the experimental result is correct. We propose to first study the properties of the beam and monitors, then to test the detector using a solid target (likely carbon) and finally to install and test the system using the liquid target. The estimates for the breakdown of the beam time request are given in Table 10.

Table 10: Beam time request. The approximate breakdown of individual runs as well as the total number of hours is shown for each category.

Experiment Phase	Beam Time (hours)	
Beam polarization/Møller polarimeter	2@50	100
Beam position, energy, etc.	3@50	150
Spectrometer debugging	4@50	200
Backgrounds	3@50	150
Preliminary asymmetry tests	5@50	250
Liquid target tests	5@50	250
Production data	2@200	400
Total		**1500**

References

[Ab82] H. Abramowicz *et al.* (CDHS) Z. Phys. **C15** (1982) 19.

[Al81] S. F. Alvarado *et al.*, Z. Phys. **B44**, 259 (1981).

[Ar91] J.Arrington *et al.*, CalTech Preprint OAP-711 (1991), Submitted to Nuclear Instruments and Methods

[As89] J. Ashman *et al.*, Nucl. Phys. **B328** (1989) 1.

[Be89] D. Beck, Phys.Rev. D **39** (1989) 3248.

[Be91] D. Beck, to be published.

[Bi91] J. Bisognano *et al.*, "Design Considerations for Simultaneous FEL and Nuclear Physics Operation at CEBAF," presented at the 13th International Free-Electron Laser Conference (1991) (to be published).

[Ca78] R. N. Cahn and F. J. Gilman, Phys.Rev. D **17** (1978) 1313.

[Ca89] L. S. Cardman *et al.*, "The Illinois/CEBAF Polarized Electron Source R&D Project: Overview and Status Report," NPL Polarized Source Group Technical Note #89-4 (unpublished).

[Ca90] R.D.Carlini *et al.*, CEBAF proposal PR-89-023.

[Ch91] R.Chasteler, Private Communication (1991)

[Co75] P.Cooper *et al.*, Phys.Rev.Lett. **34** (1975) 1589

[Do89] J. Donoghue, Ann.Rev.Nucl.Part.Sci. **39** (1989) 1.

[Ho76] G. Höhler, Nucl.Phys. **B114** (1976) 505.

[Ja89] R. L. Jaffe, Phys.Lett. **229B** (1989) 275.

[Ka88] D. Kaplan and A. Manohar, Nucl. Phys. **B310** (1988) 527.

[Ku90] K. Kumar, Syracuse University Ph.D. thesis (1990), unpublished.

[Ku90a] Y. Kurihara *et al.*, KEK Preprint 90-92 (1990); summarized in ref. [Re90].

[La91] R. M. Laszewski, "Status of Parity Detector Design Studies." UIUC/NPL Technical Report 91-01 (1991).

[Li88] J. Lightbody and J. O'Connell, Computers in Physics **2** (1988) 57.

[Ma84a] A. Manohar and H. Georgi, Nucl. Phys. **B234** (1984) 189.

[Ma84b] W. J. Marciano and A. Sirlin, Phys. Rev. D **29** (1984) 75.

[Ma89] T. Maruyama *et al.*, Appl. Phys. Lett. **55**, 1686 (1989).

[Ma91] T. Maruyama *et al.*, Phys. Rev. Lett. **66**, 2351 (1991).

[Mc89] R. D. McKeown, Phys. Lett. **219B** (1989) 140.

[Me90] F. Meier *et al.*, cont. to the Bonn Workshop as quoted in ref. [Re90].

[Mu90] M. J. Musolf and B. R. Holstein, Phys. Lett. **242B** (1990) 461.

[Na90] T. Nakanishi and S. Nakamura, Nagoya Univ. Preprint DPNU-91-04, 1990; (unpublished) (see also ref. [Re90]).

[Na91] J. Napolitano, Phys.Rev. C **43** (1991) 1473.

[Na91a] T. Nakanishi *et al.*, Nagoya Univ. Preprint DPNU-91-23, 1991; and (to be published)

[Napc] T. Nakanishi, private communication.

[Ne91] G. Neil *et al.*, "FEL Design Using the CEBAF Linac," presented at the 13th International Free-Electron Laser Conference (1991) (to be published).

[Om90] T. Omori *et al.*, Nagoya Preprint DPNU-91-12 and KEK Preprint 90-190, 1990; submitted for publication to Phys. Rev. Lett.

[Po89] S. J. Pollock, Phys.Rev. D **39** (1989) 163.

[Re90] E. Reichert, in *Proc. of the 9th Int. Symp. on High Energy Spin Physics*, Bonn, 1990 (to be published).

[Repc] E. Reichert, private communication.

[Si76] C. K. Sinclair, AIP Conf. Proc. **35**, 426 (1976).

[Si81] C. K. Sinclair, in *High Energy Physics with Polarized Beams and Targets,* ed. C. Joseph and J. Soffer, (Birkhauser Verlag, Basel, 1981), p. 27.

[Si89] C. K. Sinclair, in *High Energy Spin Physics*, p. 1412, ed. K. J. Heller (AIP, New York, 1989), and references therein.

[So89] G. S. Solomon *et al.*, J. Appl. Phys. **65**, 1952 (1989).

[So90] P. A .Souder *et al.*, Phys.Rev.Lett. **65** (1990) 694.

[Tepc] V. I. Terechov, private communication.

[Wa90] B. Wagner *et al.*, Nucl. Inst. Meth. **A294** (1990) 541.

[We90] S. Weinberg, Phys. Rev. Lett. **65** (1990) 1181.

[Ze89] V. Zeps, Ph.D. thesis, University of Washington, 1990 (unpublished).

[Zo82] P. Zorabedian, Ph.D. thesis, Stanford University; and SLAC-248. (1982).